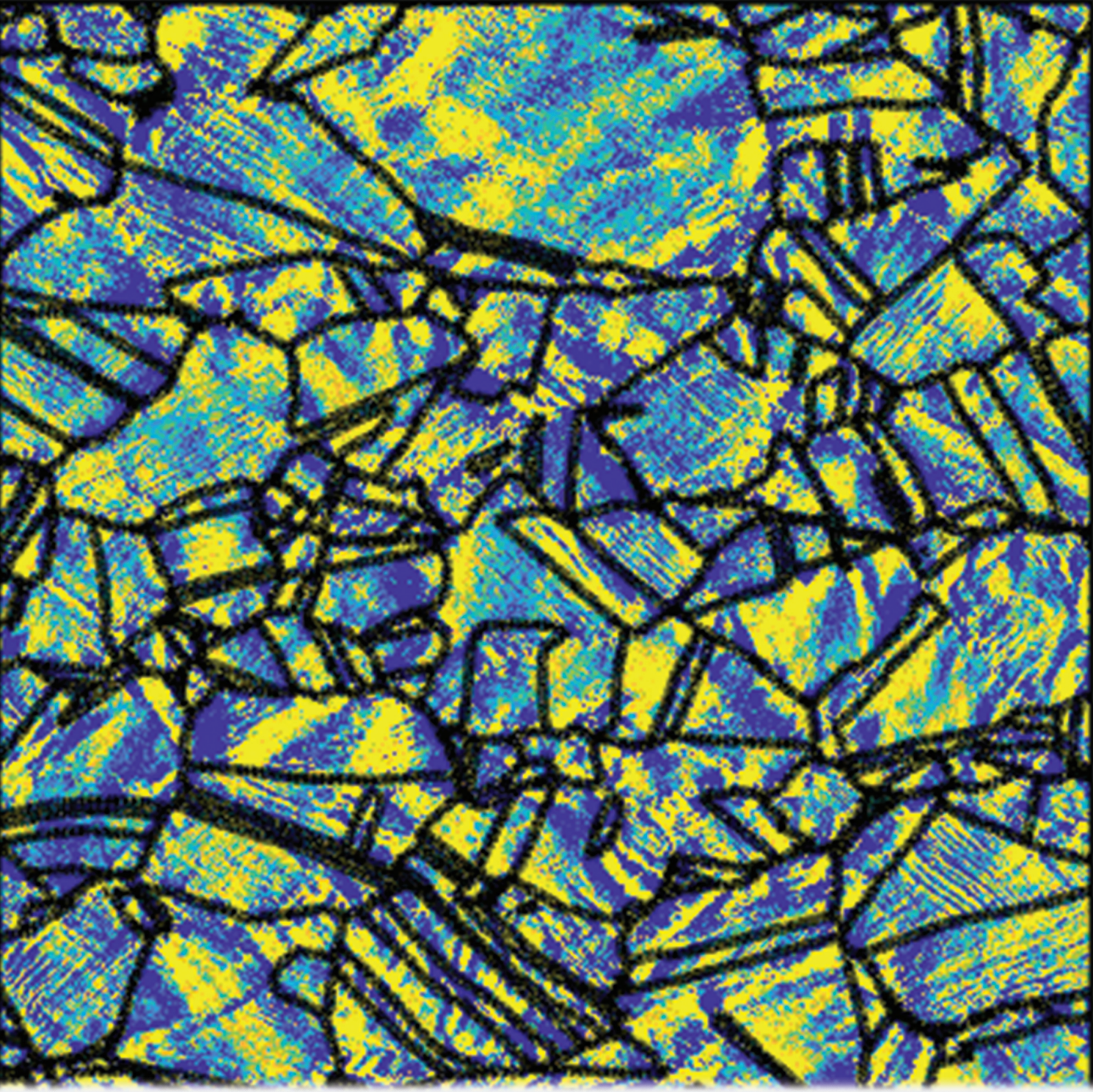

Master Thesis

MSc Materials Science and Engineering

STATIC RECRYSTALLIZATION OF AUSTENITE AFTER INITIAL DEFORMATION OF A Ni-30Fe ALLOY

Jonathan Joe Eipe

5003261

TU Delft

DELFT UNIVERSITY OF TECHNOLOGY

MS53035 - MSC THESIS

Static Recrystallization of austenite after initial deformation of a Ni-30Fe alloy

by

JONATHAN JOE EIPE (5003261)

Supervisors:
Dr.ir. SE Offerman
Pablo Garcia Chao

Committee Members:
Dr.ir. SE Offerman
Prof.dr.ir. Jilt Sietsma
Pablo Garcia Chao
Dr.ir. Kees Bos
Dr.ir. Winfried Kranendonk

A thesis submitted in fulfillment of the requirements for the degree of Master Of Science

in the

Faculty of 3mE

Materials Science and Engineering (MSE) Department

Acknowledgements

Firstly, I would personally like to show absolute gratitude to my supervisors at TU Delft, Dr.ir. SE Offerman and Pablo Garcia Chao, for granting me the opportunity to work along with them, in this prospering metallurgical field, affiliated with the Digitally Enhanced New Steel Product Development (DENS) programme. Despite the hardships of the COVID-19 pandemic and mutilple lockdowns that we had to endure, I will always appreciate the constant guidance from my supervisors, for keeping extra time during the weekly meetings to make sure all tasks and aspects of my thesis were covered. Particular mention to Pablo for the daily prompt responses to my never-ending list of questions, and providing the deformation-dilatometry measurements necessary for the thesis report.

I would also like to acknowledge Tata Steel(Netherlands) for conducting and providing me access to the experimental EBSD measurements, which played a key role in achieving accurate-driven results for the thesis project. Special thanks also to Winfried Kranendonk at Tata Steel, for giving me useful feedback and ideas at every stage of the thesis.

I would like to acknowledge the efforts of Avanika P. Yammiyavar for designing the cover page for the thesis report. Finally and most importantly, I would like to show my deepest gratitude to my parents (Joe Eipe and Susan Joe Eipe) for their continuous support, prayer and love, which is the sole reason for my achievements to date. Without them, this degree would add no value, and so I am ultimately thankful to God for all these blessings. Special thanks to my sister (Joanna Joe Eipe) to whom I would like to dedicate this thesis, wishing success in all her future endeavours.

Adapting to the Dutch lifestyle and curriculum of TU Delft for the past 2 years has been an ever-thrilling roller-coaster. Despite all the highs and lows, having constant friends at every moment has made the masters journey quite eventful and memorable. I would like to appreciate every friend that stood by me through the toughest moments in these 2 years. I am looking forward to the next phase of life, even-though my masters education concludes here. I believe that the enlightenment and theoretical knowledge gained from TU Delft would help in equipping myself, to take on challenges in the professional world of scientific research.

Abstract

The Static Recrystallization(SRX) phenomenon of austenite in C-Mn steels have a large impact on the final mechanical properties of the steel. However, the austenite recrystallization kinetics are difficult to investigate experimentally, due to solid-state phase transformations during cooling to room temperature. The best model alloys to examine SRX are those austenitic alloys such as, Ni-30Fe alloy, that do not experience undesirable phase transformation and that have similar stacking fault energy(SFE) as austenite in C-Mn steels. The hot-working of the Ni-30Fe alloy has been conducted at high deformation temperatures, followed by an uniaxial compression test at a low strain condition (ϵ = 0.2) with a strain rate of $1s^{-1}$, and an annealing temperature of 900°C (above recrystallization start temperature). Thereafter, the alloy is experimentally investigated by Electron Backscatter Diffraction(EBSD), to characterize the austenite microstructure and to measure the crystallographic orientations. The experimental measurements from the EBSD technique are subsequently analyzed using MTEX software to study the SRX phenomenon that occurs during hot rolling of steels.

The technique to separate recrystallized and deformed grains in this research has adopted the Kernal Average Misorientation(KAM) and Grain Average Misorientation(GAM) technique, rather than the previously utilized Grain Oriented Spread (GOS) technique which incidentally produced slower and inaccurate recrystallization kinetics. The initial and final grain size calculations have been conducted by consideration of the annealing twins, and the reported results are in close agreement with earlier conducted work of Sellars model. The EBSD scan which captures the Geometrically Necessary Dislocations(GND) have been experimentally measured after deformation to be approximately $4.5x10^{14}m^{-2}$, by utilizing the approach of KAM, curvature tensor and the Burgers vector with an estimated 13% error. Additionally, the effect of recovery has been captured with the continuous decrease in stored energy as a function of time, where the GND density is estimated to be $7.3x10^{12}m^{-2}$ after the annealing treatment.

The GND density present in the deformed microstructure is significant to provide the net driving force necessary for nucleation, based on the validated strain-induced-boundary-migration(SIBM) mechanism. The initial nucleation site is observed at triple junctions, and the selected nucleation criterion factor for the captured GND densities, estimates the driving force for nucleation to favour single sub-grain SIBM. The minimum critical sub-grain size required for bulging is calculated to be 3.40 ± 0.44 μm after deformation, which is an increasing parameter with time, as a result of the recovery process. The number of recrystallized grains captured at different time intervals using the validated GAM technique assists in experimental nucleation rate calculations, that have been subsequently converted for a 3D microstructure, in order to compare with the nucleation framework of Rehman's model. The recrystallization nucleation process is experimentally observed to obtain peak values at 2s and continues until all the GNDs are annealed out of the specimen. There is a large discrepancy in the nucleation rate predicted by the model, which is much higher with respect to the experimental observations reported. Finally, the experimental recrystallization kinetics is observed to be in close agreement with the JMAK model during the initial phase of the annealing treatment, but deviates in the later phase of the recrystallization process.

Contents

List of Figures

List of Tables

List of Abbreviations

HAGB	**H**igh **A**ngle **G**rain **B**oundary
SRX	**S**tatic **R**ecrystallization
$\mathbf{T_m}$	**T**emperature of melting
ϵ	Deformation strain for static recrystallization
ϵ_c	Critical deformation strain for dynamic recrystallization
SFE	**S**tacking **F**ault **E**nergy
KAM	**K**ernel **A**verage **M**isorientation
GND	**G**eometrically **N**ecessary **D**islocation
SSD	**S**tatistically **S**tored **D**islocation
EBSD	**E**lectron **B**ack**s**catter **D**iffraction
GOS	**G**rain **O**riented **S**pread
GAM	**G**rain **A**verage **M**isorientation
LAGB	**L**ow **A**ngle **G**rain **B**oundary
CSL	**C**oincidence **S**ite **L**attice
JMAK	**J**honson **M**ehl **A**vrami **K**olmogorov
SF	**S**peich **F**isher
FEG-SEM	**F**ield **E**mission **G**un - **S**canning **E**lectron **M**icroscopy

Chapter 1

Introduction

1.1 Overview

The current chapter consists of discrete sources highlighting essential information regarding the hot rolling of steels in section 1.2, which have an industrial importance for different applications. Thereafter, the chapter goes on to describe the microstructural changes that occur during the annealing phenomenon in section 1.3, followed by a short introduction to the static recrystallization process in subsection 1.3.1. Finally, a structure is provided in section 1.4 regarding the format of this thesis report.

Keywords: SRX, Recovery, Grain growth, GOS, Ni-30Fe alloy, GND density, Stored energy, KAM, Critical size for bulging, JMAK model, SF equation, Recrystallization kinetics, GAM, Nucleation, Merging function, Annealing, Twins

1.2 Hot-Rolling of Steels

The industrial revolution since the late 1700's led to the birth of rolling mills, where steel became a crucial material rolled for different purposes in heavy machinery, railroads and cargo ships. Generally, a rectangular sheet of semi-finished cast steel, referred to as billet or slab, is heated above the recrystallization temperature (which is usually between $1/3$ and $1/2$ T_m of the material) using a reheating furnace, as seen in Fig.1.1. As the initial material is hot-rolled, it is essential to continuously control the temperature to be above the recrystallization temperature, and hence a safety factor of around 50-100°C above the recrystallization temperature is added. This heated slab is usually passed through a roughing mill with a pair of edge rollers, and then a finishing mill, so that the desired thickness and improved mechanical properties are achieved (as seen in Fig.1.1). Micro-structurally, during this hot metalworking process, we observe that the grains initially undergo a deformation, which allows recrystallization and a microstructure that is equiaxed, preventing the steel from work-hardening. Finally, the finished metal sheet products, can either be as rolled steel which are coiled as seen in Fig.1.1, or steel bars that are sectioned and then packaged.

The ductility and formability properties acquired from hot metalworking processes is used for different industrial applications such as: railroads, truck frames, metal buildings, guard rails, automotive clutch plates and wheel rims, etc. From these applications, we can conclude that hot rolled steel sheets are being used for applications that do not require high precision, since the cooling procedure which occurs after the processing, provides less command over its final shape. However, since cooling occurs gradually at room temperature, it allows the rolled steel sheet to be

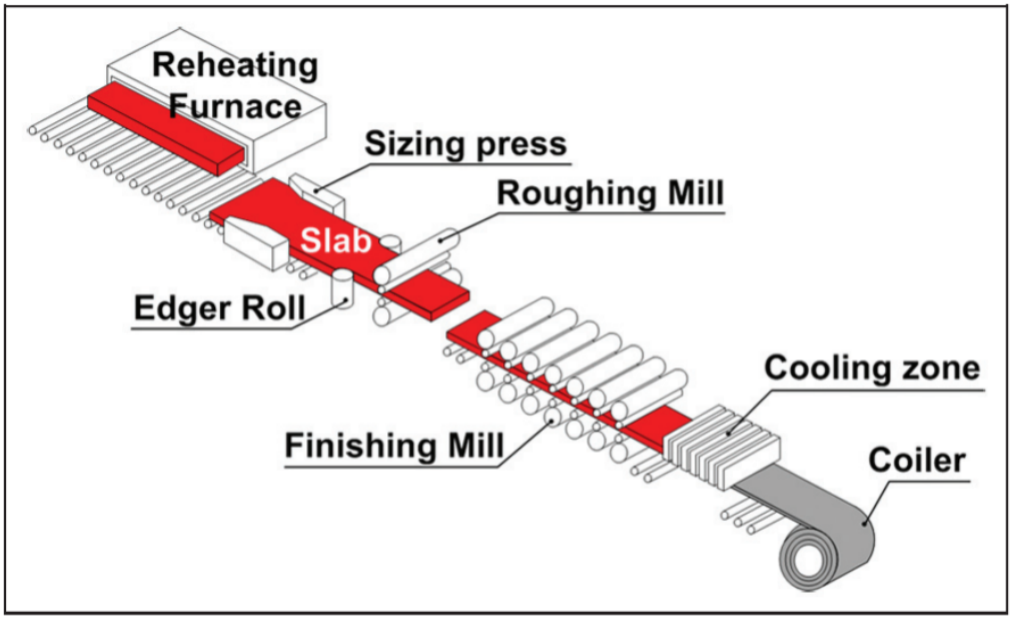

FIGURE 1.1: **Schematic representation of a hot rolling mill [1]**

liberated from internal stresses that emerge from either work-hardening or quenching processes [15].

In terms of expense, hot rolling of steel is more profitable than cold rolled steel, since it requires low processing time, thereby reducing energy costs and consumption. Hot rolling typically utilizes larger ingots and larger reduction rolling mills than other metal working processes, enhancing greater manufacturing efficiency and producing an environment for improving rolling speed. Therefore, this would assist in accomplishing an automated and uninterrupted rolling process. Moreover, based on the industrial applications, hot rolled steel is optimal for situations where total material strength is more important than dimensional tolerances and surface finish. Despite surface finish not being ideal for hot rolled steels, scaling of the sheet surface can be eliminated by sand blasting, grinding, or metal pickling baths. Thereafter, the descaled steel could be coated to provide the necessary surface finish to be sold in the market.

1.3 Annealing Phenomenon

Annealing of the metal sheet allows microstructural changes such as: recovery, recrystallization and grain growth of the microstructure, in order to annihilate or arrange the defects in a lower energy configuration. Based on the annealing phenomenon from Fig.1.2, the recrystallization process, is generally associated with the reduction in the hardness and strength of a material, so as to improve its ductility and formability. The recrystallization process can be a complex procedure to be defined since it is accompanied by the recovery and grain growth in the microstructure. According to Doherty et al.[16], the recrystallization can be defined by: *"The formation of a new defect-free grain structure in a deformed material through the development and migration of HAGBs with a misorientation >15°, constrained by the stored energy obtained during deformation."* Therefore, this definition permits us to separate recrystallization

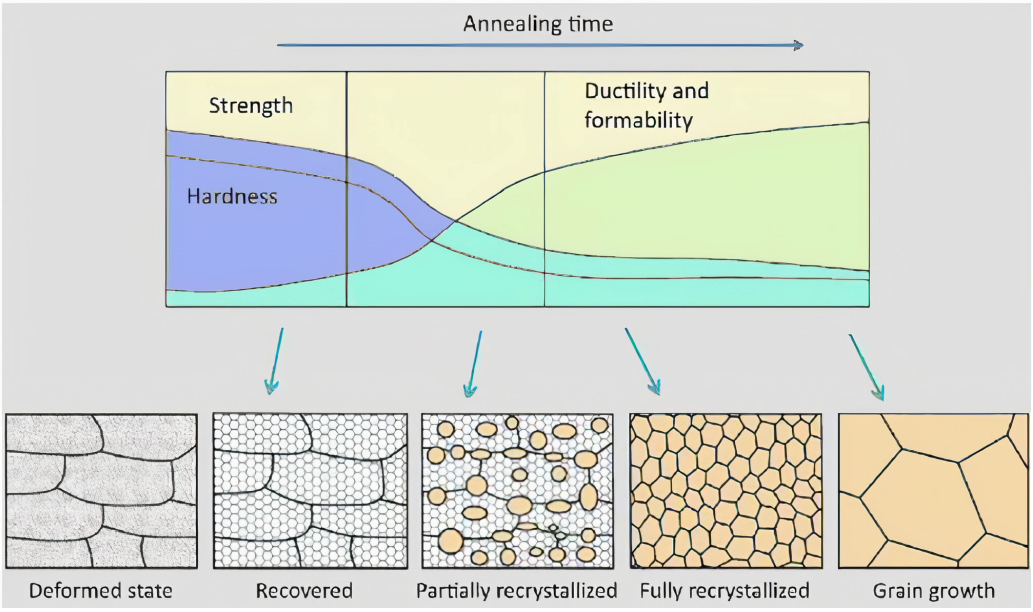

FIGURE 1.2: **Schematic representation of the Annealing phenomenon [2]**

from the other associated processes such as: recovery and grain growth.

Initially, when the material undergoes deformation, the microstructure consists of high defect dislocation density and large internal stresses, causing an environment which requires the arrangement of defects having a lower energy configuration. Thereafter, during recovery, the rearrangement and annihilation of dislocations occurs, but the HAGB does not undergo migration, achieving a metastable state. So, for recovery, softening of the material begins, where only a partial restoration of properties and a homogeneously formed microstructure is developed, as shown schematically in Fig.1.2. From these terminologies associated with the annealing treatment, it can be understood that recrystallization is a continuation of the restoration process in which the newly formed grains have fewer dislocations(compared to the deformed state) within the recovered microstructure, as shown in Fig.1.2. The earlier defined recrystallization process, is more commonly referred to as *primary recrystallization*, which is the basis for the thesis project. Then, during grain growth process, the curvature and energy of the grain boundary determines the driving force [17]. Thereby, grain growth causes the annihilation of the smaller grains and growth of only the larger grains, such that the grain boundaries attains a lower energy configuration and a reduction of the total area of the grain boundary, as shown schematically in Fig.1.2.

Research with respect to annealing have identified two phenomenological categories [18]: continuous and discontinuous annealing phenomena. In continuous annealing phenomenon, there are no identifiable nucleation and growth stages. Continuous annealing allows us to categorize the microstructural changes as: recovery by subgrain growth, continuous recrystallization and normal grain growth. However, with the discontinuous annealing phenomenon, the deformation in the microstructure evolves heterogeneously by differentiated nucleation and growth stages. Initially, nucleation of strain-free recrystallized volume is developed, followed by the growth

of the recrystallized grains, where migration of HAGB occcurs, so as to replace the deformed microstructure. Discontinuous annealing allows us to categorize the microstructural changes as: discontinuous subgrain growth, primary recrystallization and abnormal grain growth. Based on this description, the discontinuous annealing phenomenon has relevant importance for the thesis project.

1.3.1 Static Recrystallization Process

The semi-finished cast steel in the form of a billet consists primarily of coarse austenite grains in the microstructure, with brittle characteristics that prevent the dislocation motion across grain boundaries. As the billet is passed through the rollers, the initial grain structure undergoes changes in dimension due to deformation, forming an elongated pancaked structure. Moreover, the deformation induced from hot rolling, generates deformation bands within the grains, leading to deviation in the local orientations. Therefore, the primary recrystallization phenomenon explains the microstructural and crystallographic orientation changes of the as-deformed microstructure, when it is annealed above the recrystallization critical temperature, at a critical strain and a minimum held time(annealing time interval).

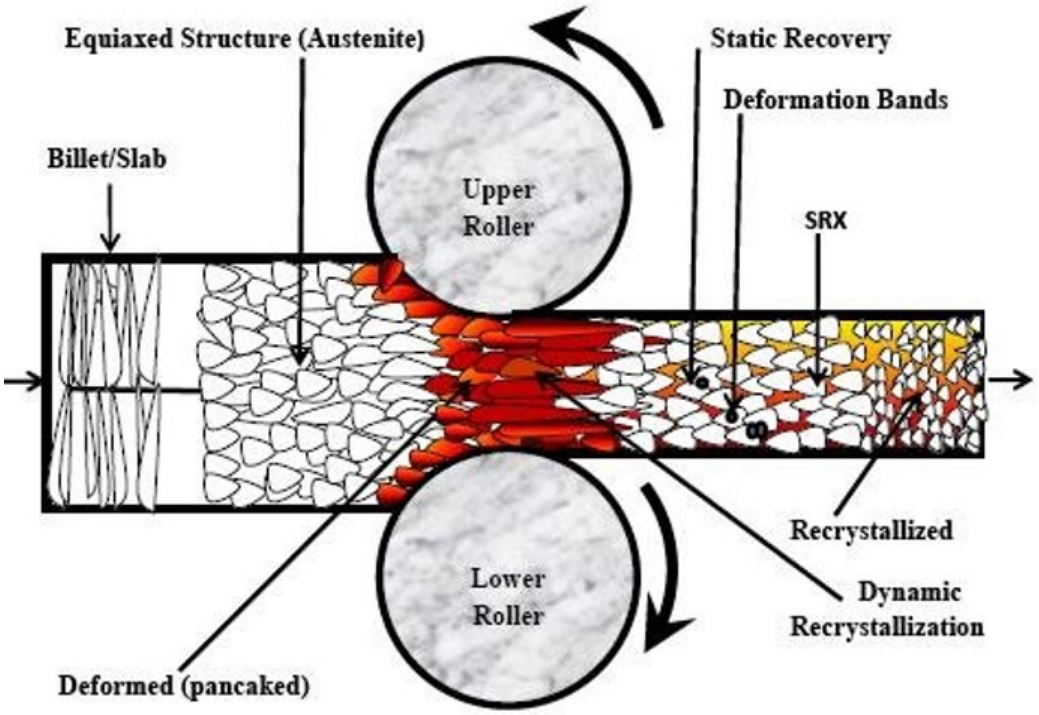

FIGURE 1.3: **Recrystallization Phenomenon during hot rolling [3]**

This phenomenon would be a crucial method for achieving the refinement of grain size and desired mechanical properties during hot working. The process of static recrystallization(SRX) will be the main area of interest in this project, where the recrystallization process begins and continues only after the material has been deformed. This processing technique encompasses the defect-free grains that undergo nucleation and growth processes in the deformation matrix, which have concurrently experienced dislocation annihilation(static recovery) during the annealing treatment. By contrast, the grains that are formed during the deformation condition is referred

to as dynamically recrystallized grains(as seen in Fig.1.3), which is beyond the scope of interest for this project. The SRX phenomenon at a certain annealing temperature is highly dependent on a deformation strain(ϵ), below the critical strain(ϵ_c) condition for dynamic recrystallization and the recrystallized grain size, which is further examined after the austenitic alloy is modelled in chapter 2.2.

1.4 Thesis Structure

The thesis report comprises of different chapters, namely:

- **Introduction**: The basic knowledge required to understand the essential metallurgical phenomenon in the current field of research.
- **Literature Research**: State-of-the-art literature review highlighting background problems, physical significance, research objectives and methodology for the thesis project.
- **Experimental Methods**: Explanation of the experimental procedures conducted to obtain the results for the thesis project.
- **Results and Discussions**: Obtaining quantitative and qualitative results based on the experimentation and correlation of results with the state-of-the-art literature research.
- **Conclusions and Recommendations**: Establishing firm conclusions based on the comparison of different results and formulating recommendations for future research in the similar metallurgical field.

Chapter 2

Literature Research

2.1 Overview

SRX is a highly widespread and essential restoration process occurring during hot working of steels at lower strain deformation. The static recovery process after deformation has fascinated a substantial interest amongst various study groups because it increases formability and ductility properties. Such research groups have mainly concentrated on the mechanical response, grain size variations and kinetics of the SRX process, as a function of thermomechanical parameters such as temperature and strain. The current chapter mentions the relevance of the modelled alloy in section 2.2 with respect to low carbon steels such as C-Mn steels, which would directly benefit industrial rolling applications. Then, the methodology adopted to measure deformation for calculation of dislocation density is described in section 2.3. The net driving force is supplied by the deformation stored energy explained in subsection 2.3.1, mainly due to the extended array of elastic stresses linked with the dislocation and subgrain structure that is formed from deformation. Then section 2.4, describes how SRX phenomenon progresses by the development and movement of newly formed HAGB using a defined mechanism and model at certain nucleation sites. During recrystallization, there is no new deformation inflicted and the microstructure resulting from SRX normally comprises of equiaxed crystals with the presence of twin boundaries. So, section 2.5, explains the formation of annealing twins along with a statistical quantification approach, and differentiates it with respect to the former twins. Additionally, in section 2.6, the recrystallization behaviour is described, mainly following the framework of the JMAK sigmoidal kinetics, which ultimately causes the refinement of the grains in the microstructure. Finally, the chapter concludes in section 2.7 with the formulation of the research objectives for this thesis report, based on the state-of-the-art literature review.

2.2 Modelling Austenitic Alloy and Experimental Conditions

The SRX phenomenon of austenite in C-Mn steels have a relative importance with respect to the final mechanical properties. However, currently for austenite phase steels, there is limited information available for the SRX process with respect to the development of dislocation substructures (statically recovered) of the deformed matrix and its subsequent progressive development to form dislocation-free recrystallized grains (by recrystallization nucleation and growth processes). Additionally the solid-state phase transformation taking place in C-Mn steels during cooling restrains the precise examination of the austenite microstructure and the SRX kinetics. A solution to this problem is to study an alloy such as 304 stainless steel or Ni-30Fe alloy that retains its austenite structure upon cooling down to room temperature [4]. The

former alloy(304 SS) is known to have a lower SFE (stacking-fault energy) in comparison to C-Mn steels, which has a SFE value of approximately 0.75 J/m^2. Hence, 304 SS is not suitable for the SRX phenomenon study despite its relatable deformation characteristics, cheap modelling cost and availability [4].

By contrast, deformation behaviour studies[19],[20], of Ni-30Fe alloy have shown that SFE values are comparable to the C-Mn steels. The dissociation of Shockely partials would be the most precise method to calculate the SFE, but it is not always possible to get the dislocations to dissociate, which is seen in the case of Ni-30Fe model alloy [4]. Despite these complications, the results obtained by Charnock et al.[21] and confirmation by Taylor et al.[4], have shown that Ni-30Fe model alloy at room temperature has a SFE similar to that of C-Mn steel, and hence can be used to study the deformation of austenite [10]. Therefore, the alloy chosen for the purpose of studying the SRX phenomenon is the Ni-30 Fe alloy with an approximated SFE value of 0.712J/m^2, obtained from the literature [21]. For the purpose of this report, the SFE values below 0.40J/m^2 can be categorized as low SFE materials(e.g. 304 SS: 0.21J/m^2 [15]), whereas SFE values higher than 1.00J/m^2 can be determined as high SFE materials (e.g. Nickel: 1.28J/m^2 [15]). This categorization of materials based on their SFE values is derived from the SFE of pure materials reported by Humphrey et al.[15]. On the basis of this categorization, Ni-30Fe alloy can be labelled as an intermediate SFE material.

The hot working of the Ni-30Fe alloy passed through the rollers can be determined by the applied deformation strain, strain rate, annealing temperature, and annealing time. These parameters which control the processing of the alloy, along with the material parameters such as the initial grain size and chemical composition, determine the static recrystallization kinetics and its subsequent recrystallized grain size. The hot working of austenite could be initially conducted at a high deformation temperature, where the sample is held until the austenite phase is formed. Thereafter, the temperature can be lowered to an annealing temperature of 900°C, where the sample is held for a short period so that a homogenized temperature is achieved. Then, a strain is induced at a selected strain rate for the SRX phenomenon to proceed.

After the deformation strain is applied at 900°C, the deformed matrix can rearrange and annihilate the dislocations, followed by the initiation of the nucleation event. As described in subsection 1.3.1, the SRX phenomenon is directly linked with the critical strain(ϵ_c), so as to essentially avoid the onset of dynamic recrystallization. The correlation between ϵ_c and ϵ_p (peak strain) can be obtained by using an approximated factor $k = 0.87$, where $\epsilon_c = k\epsilon_p$ [3]. The peak strain and critical strain has been experimentally obtained and confirmed by Taylor et al. [4], using the flow-curve analysis for Ni-30Fe alloy, as shown in Fig.2.1(a). Correspondingly, the work-hardening rate θ, has been calculated as the incremental stress divided by the incremental strain in Fig.2.1(b). The transitional point where a change in the flow-curve slope occurs, represents the condition where the grains begin to dynamically recrystallize during deformation. The flow curves beyond the maximum peak strain observe continuous work-hardening rates, where the dominant restoration mechanism is dynamic recovery, which is not studied in this thesis. Nevertheless, the obtained peak strain from the Fig.2.1 for the Ni-30Fe alloy at 900°C is 0.37. Therefore, using the co-relation factor k, we obtain a minimum critical strain of 0.32 at 900°C for the onset of dynamic recrystallization in the Ni-30Fe alloy.

Therefore, on consideration of the above conditions for the Ni-30Fe alloy, a deformation strain, $\epsilon < \epsilon_c$ at an annealing temperature of 900°C, must be applied for SRX phenomenon to proceed. A deformation strain of ϵ=0.2, is chosen in this report to study the SRX phenomenon for different annealing times. It is important that the experimental conditions selected for the modelled Ni-30Fe alloy does not encounter dynamic recrystallization, as it would subsequently produce systematic errors during the nucleation process.

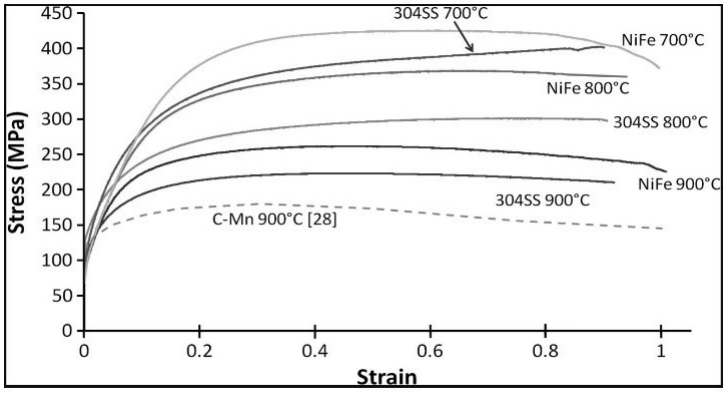

FIGURE 2.1: **Flow curves for C-Mn, 304 SS and Ni-30Fe alloy deformed at different annealing temperatures [4]**

2.3 Deformation measurements: KAM and GNDs

Once the material has been deformed, the spatial distribution of dislocations and its density before the recovery stage begins is essential for understanding the physical mechanisms involved with the microstructural changes. Hence, it is important to introduce a method of estimating the deformation induced based on the Kernel average misorientation(KAM). The KAM can be defined as the estimated local grain orientation that provides the first approximation regarding dislocation network configurations in the deformed microstructure, generally obtained from EBSD data. Translating this definition into a function, we need to introduce some orientation parameters, namely [6]:

- $o_{(i,j)}$: The orientations at a pixel(kernal) position (i,j)
- $N(i,j)$: The set of all neighbouring pixels that are taken into consideration.
- ω : The disorientation angle between a central orientation pixel point (i,j) and a neighbouring orientation pixel point (k,l)

Thereafter, the $KAM_{i,j}$ at a kernal position (i,j) can be formulated as shown in Eq.2.1 [5]:

$$KAM_{i,j} = \frac{1}{|N(i,j)|} \sum_{(k,l)\in N(i,j)} \omega(o_{(i,j)}, o_{(k,l)}) \tag{2.1}$$

Here, the selection of number of neighbouring pixels belonging to the N(i, j) set is essential for the KAM function computation. Additionally there are some other limitations that must be taken into consideration such as [5]:

- Number of nearest neighbours (n), which is taken as 2 for our case. The neighbours for the Ni-30Fe alloy fits a hexagonal grid, as shown in Fig.2.2 (a).
- Neighbouring pixels are considered only in the same grain.
- Neighbouring pixels only with a misorientation angle lower than a threshold angle, $\Delta\theta_{\text{threshold}} = 2.5^{\circ}$, are taken into account.

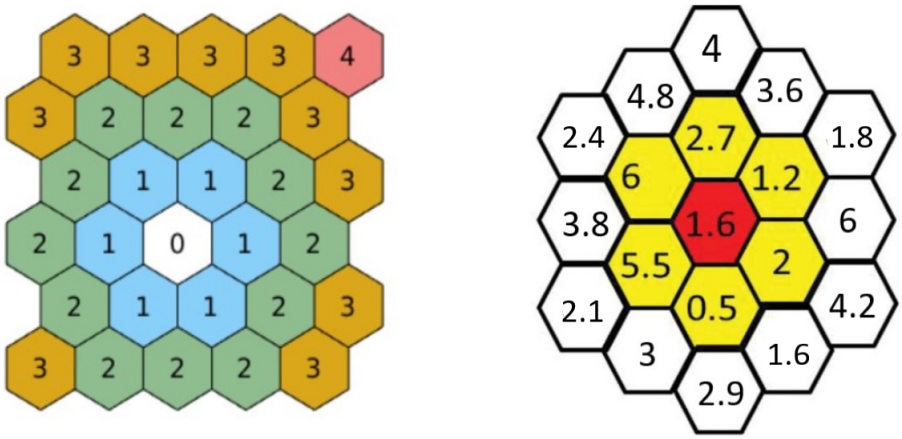

FIGURE 2.2: **(a) Number of nearest neighbours; (b) Calculation of KAM values using the defined KAM function for 2nd nearest neighbours [5][6]**

The obtained KAM values as shown in Fig.2.2(b) using the function in Eq.2.1, can be optimized using denoising techniques described in chapter.3.4.2, and thereafter scaled down to a regime between 0-2. It is important to note that this deformation measurement approach used for EBSD systems is dependent on the number of pixels within the kernel, the threshold angle ($\Delta\theta_{\text{threshold}}$), the scanned area of the sample and its corresponding step size.

Over the previous couple of decades, the EBSD technique has been computerized and effectively developed with respect to its precision and indexing speed [22]. Calculating and plotting dislocation densities and the correlated stored energy after deformation are significant for the quantitative explanation of SRX phenomenon. There are a number of mechanisms that are greatly reliant on the specifics of the dislocation density and stored energy distributions in the Ni-30Fe alloy. The impact of the elastic strain field and the curvature of the crystallographic structures is known to stimulate the local misorientations. It has been reported [23] that the impact of the elastic strain field is much less significant than the rotation of the lattice or the local misorientation. Hence, the elastic field can be assumed to be negligible and consequently the lattice curvature can be associated to the existence of dislocations. So, these dislocations are determined by the method which stimulate a quantifiable curvature in the crystallographic structure and are referred to as geometrically necessary dislocations(GNDs) or statistically stored dislocations(SSDs). The separation between GNDs and SSDs is highly dependent on the step size chosen for the EBSD scans. For the purpose of this thesis project, only the GNDs are considered and measured from the EBSD technique based on the intragranular misorientations because

only the GNDs are associated with the lattice curvature. A quantifiable assessment of GNDs from EBSD measurements can be obtained with two main methods.

The first method is established using the estimation of the dislocation density tensor reported by Nye et al.[24], also known as the Nye tensor. It is achievable to directly measure 3-components of the Nye's tensor and to approximate the other two components from the EBSD measurements of the 2D scanned region of the sample. However, there would be four residual components of the Nye tensor that cannot be accessed through experimentation and must be computed by decreasing the global dislocation density [23]. The major obstacle from this method is that numerous values can be obtained and the reduction of the global dislocation density to estimate all the 9 components of the Nye tensor could be cumbersome.

The second method which is easier and preferred can be conducted using the misorientation angle between pixels positioned at a certain distance Δx from each pixel. Utilizing the information based on the strain gradient model by Gao et al.[25], the GND density can be formulated as shown in Eq.2.2 [23], on the basis of a simple uniaxial compression test, and in association with the misorientation angle within the kernal.

$$\rho_{\mathrm{GND}} = \frac{k\Delta\theta}{b\Delta x} \tag{2.2}$$

where, b = 248pm, is the burgers vector norm for the edge and screw dislocations in Ni-30Fe alloy. Then, Δx is the unit length over which the misorientation is measured. The parameter k is a constant which is dependent on the type of sub-grain boundary, where k=1 if the predicted dislocation network consists of tilt sub-grain boundaries made of edge dislocations, and k=2 if the situation consists of twist sub-grain boundaries made of screw dislocation. For our case, k is taken as 1, since GNDs are mainly known to be part of of tilt boundaries in the crystallographic structure. The elastic curvature κ with a measure of m^{-1}, is the basis for the dislocation density quantification and is derived from Eq.2.2, where $\kappa = \Delta\theta/\Delta x$ [26].

From a realistic viewpoint, an EBSD map comprises of distinct orientation measurements at positions separated by Δx, and misorientation angle $\Delta\theta$. So, the elastic strain field data can be attained from the curvatures, $\kappa = \Delta\theta/\Delta x$. Thereafter, the KAM values obtained from the earlier derived function in Eq.2.1, can be integrated into the local GNDs calculation method (shown in Fig.2.3). This method is utilised for the thesis project, as observed in subsection 4.5.1, which is highly influenced by the generic curvature, κ. The curvatures have a percentage of error that is highly dependent on the step size(considered reference distance, known as Δx), and an error on the spatial position known as δx. Additionally, it is also important to note that the lowest misorientations, typically below 0.5°, must be neglected in the analysis as those misorientations might account for measurement noise. The estimation of levels of noise is complicated and hence a misorientation error, $\delta\theta$=0.5°, and certain denoising techniques must be executed. Therefore, the relative error for the curvature tensor can be calculated as shown in Eq.2.3 [23], and correspondingly the errors of the calculated GNDs can also be estimated.

$$\frac{\delta\kappa}{\kappa} = \frac{\delta\theta}{\Delta\theta} + \frac{\delta x}{\Delta x} \tag{2.3}$$

So, the percentage error must be accounted with this method, since the misorientation measured around a crystal defect is dependent on the step size, reducing the local dislocation density for an oversized step size [23].

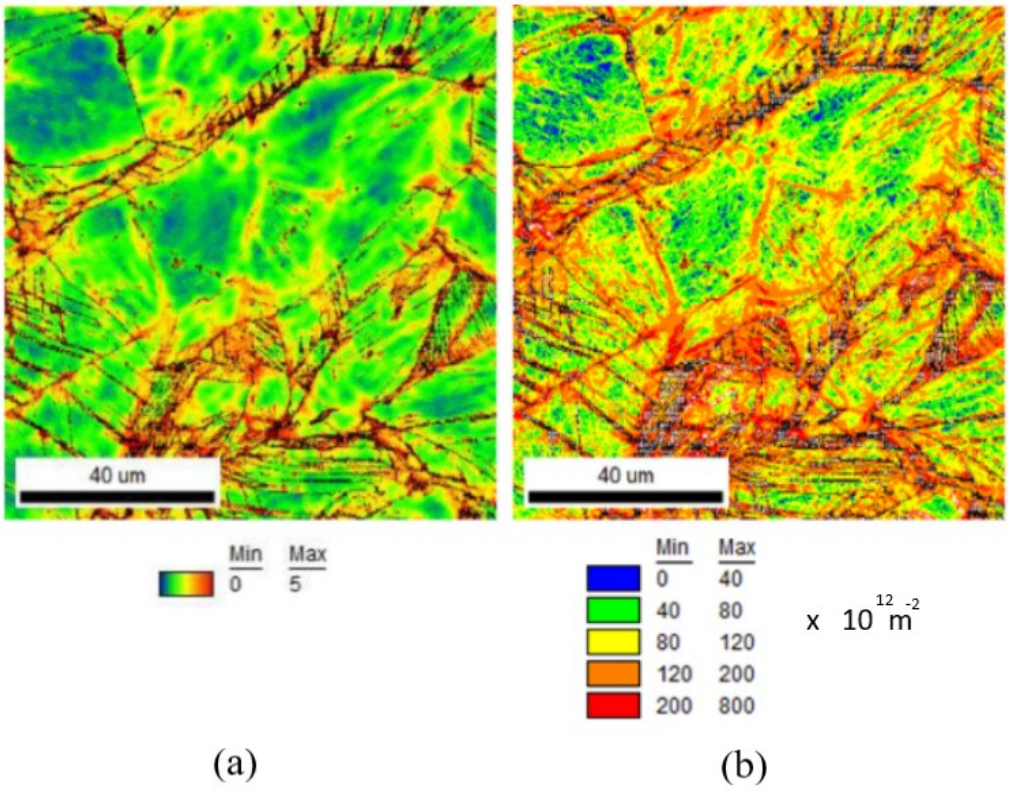

FIGURE 2.3: **(a) KAM map plotted for 304SS alloy after deformation; (b) Corressponding GND density calculated using the KAM values and curvature tensor [7]**

2.3.1 Stored Energy

Once a material is deformed, the following recovery and recrystallization nucleation behaviour is dependent on the stored energy and its spatial distribution in the sample. In terms of the microstructure, GNDs develop into forests after deformation. These GNDs forests can be found as kinks or jogs with intricate tangles and pile ups, which subsequently arrange themselves into lower energy configuration as a result of recovery [11]. Thereby, the static recovery allows the formation of cells or sub-grain boundaries, which can be observed as the smallest volume in an EBSD map with a step size in the order of 100nm. Thereafter, the migration of these sub-grain boundaries, due to accumulation of dislocations, is known to provide the driving force required for recrystallization nucleation. Additionally, the microstructure that contains a coarse-grained structure becomes partially divided upon deformation, developing varying orientations in a deformed grain. This phenomenon is known to cause the formation of deformation bands based on the inhomogeneous stresses transferred from the surrounding grains, and finally providing an energy advantage required for recrystallization nucleation to occur. So ultimately, the estimation of the stored energy is essential for the prediction of the different stages in recrystallization [27].

The dislocation line energy, E_{dis} per unit length, can be approximated as shown in Eq.2.4 [15], by neglecting the dislocation core energy and presuming isotropic elasticity.

$$E_{\text{dis}} = \frac{Gb^2 f(\nu)}{4\pi} ln(\frac{R}{R_0}) \tag{2.4}$$

where, R is defined as the higher radius limit for separating the dislocations, usually taken as $\rho^{-1/2}$. Then, R_0 is the lower radius limit, usually taken as $2.5b$. The shear modulus, given as G, is an elastic constant dependent on the temperature and hence has to be adjusted from 81GPa at room temperature [11]. The shear modulus for the Ni-30Fe alloy at 900°C has been obtained as 42GPa using the approximation G = 81*10^9[1-{T(K) - 300}/1810] [11]. Finally, the function of the Poisson's ratio, $f(\nu)$, can be calculated by proceeding with an average number of edge and screw dislocations, $\sim (1-\nu/2)/(1 - \nu)$, with a Poisson's ratio of 0.3 [15]. Thereafter the stored energy (S_E) can be approximated with the obtained GNDs as:

$$S_{\text{E}} = \rho_{\text{GND}} E_{\text{dis}} \tag{2.5}$$

However, it is important to note that the approximations from Eq.2.5, is only suitable if the dislocations are positioned in a manner where the stress fields of other dislocations are concealed. The theories related to dislocation [27] observe that the dislocation line energy depends on its position in the microstructure, where it has the highest energy in a pile-up and lowest when it forms as subgrain boundaries. Therefore, it essential to know how the dislocations are found in Ni-30Fe alloy for the deformed conditions, which is known to appear as the described GND forests with intricate tangles [27].

Another approximation for the stored energy, S_E, can be obtained as shown in Eq.2.6 [28]:

$$S_{\text{E}} = \frac{1}{2} \rho_{\text{GND}} G b^2 \tag{2.6}$$

Finally, a comparison between both the equations, Eq.2.5 and Eq.2.6 can be conducted to validate the relevance and accuracy of the calculated dislocation line energy per unit length from Eq.2.4. The effect of recovery can be captured by taking the stored energy (S_E) as a function of time (t), using Eq.2.6. The inference based on this equation is that, due to the effect of static recovery, the dislocation density is reduced with time and consequently the stored energy is reduced.

In conclusion to this section, EBSD data offers the calculation of the GND density from the KAM values and curvature tensor. Finally, the deformation stored energy and the effects of static recovery that are considered in this section permits the SRX phenomenon to be further modelled, using a nucleation framework, shown in the next section.

2.4 Recrystallization Nucleation

The SRX microstructural changes that occur after the material has been deformed are essentially thermally activated restoration and softening processes, categorized as: recovery, recrystallization and grain growth. Substructural recovery occurs prior to recrystallization, where the material decreases its stored energy. During this process, the dislocation density considerably reduces by dislocation annihilation and

the residual dislocations are arranged in configurations of low energy. This process allows formation of LAGB (low angle grain boundary with misorientations smaller than 15°) known as sub-grains [29]. Thereafter, the recrystallization process incorporates a nucleation stage of strain-free grain volumes [29], which subsequently consumes the deformed microstructure in its entirety, by HAGB migration. It is important to note that the recrystallization nucleation stage is, by itself a procedure of migration of the subgrains, and hence, the theory of classical nucleation pertaining to phase transformations is ineffective here.

The recrystallized nucleus can be understood as a microscopic crystal that has a low internal energy, which possesses the ability to grow in the recovered microstructure separated by a HAGB. It is highly unlikely for the number of nuclei per unit volume (N) to be a constant parameter and hence, the nucleation rate is a complicated parameter, due to the detection method used and time of observation. The nucleation rate can be defined as [15]:

$$\dot{N} = dN/dt \tag{2.7}$$

Recrystallization nucleation frequently begins in areas that include microstructural inhomogeneities. These inhomogeneities are for example: large boundary curvatures and strain gradients that are in severely distorted grain boundaries; triple junctions formed by neighbouring grains; the high dislocation densities present in deformation bands of coarse-grains.

Investigating and recognizing nucleation events that arise in these type of sites, develops the need to primarily identify the underlying deformation substructures and the particular characteristics that render these sites as suitable nucleation sites. This is an indication that recrystallization study is not a "1 - mechanism" pursuit, but instead typically involves a systemic methodology, where a range of potential processes and their interactions have to be brought into contemplation.

It should be noted that even with the available computation models (Monte Carlo Potts models, Continuum mechanical models, Cellular automata) [30] on recrystallization kinetics, it is complex to experimentally arrive at the nucleation rate due to the involvement of different nucleation mechanisms and sites. However, with synchrotron radiation (High energy X-rays) such as the 3DXRD microscopy technique, the nucleation rate can be determined [31]. With respect to this thesis project, the experimental nucleation rate is attempted to be compared to a physically based model by Rehman et al. [11].

Despite the mentioned improvements made to study nucleation in 3D, the preferred and best method to study the recrystallization nucleation is directly by acquiring measurements from 2D itself, followed by a conversion to 3D. For conversion of the experimentally calculated nucleation rate from 2D to 3D, the modified procedure of Johnson-Saltikov[32] conducted by Erica Anselmino[8] is adopted for our study.

The methdology for the conversion from 2D to 3D have made multiple assumptions such as the shape, spatial distribution and orientation of the grains. Using the similar criteria from the literature [8], it can be observed that the average grain diameter in 3D is larger by a common approximated factor. The nucleation rate calculated in 2D, converted to 3D, and its corresponding equivalent diameter is shown in Fig.2.4. The main parameters presented here are: N_A(i)% and N_v% which is defined as the

number of particles per unit area and per unit volume, respectively for a sample section, *i*. From Fig.2.4, we can infer that the nucleation rate would be inversely proportional to the diameter, since the nucleation rate ideally includes the number of recrystallized grains formed/mm^3s.

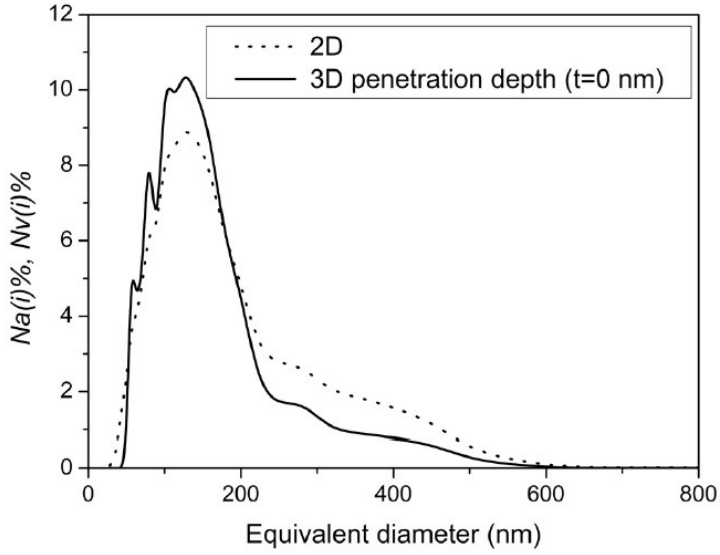

FIGURE 2.4: **Particle size distribution for an Al annealed sample[8]**

2.4.1 Nucleation Mechanisms and sites

The nuclei developed during SRX comprise of reduced dislocations densities as compared to the deformed grains. These newly developed crystal grains are partly bordered by mobile HAGBs. Hence, recrystallization nucleation, involves those mechanisms that allow the creation of new mobile HAGBs or the bulging of previously existing HAGB. Even though officially there two stages in recrystallization are known as the nucleation and the growth stages, yet both processes are typified by growth, meaning that it is related to the motion of interfaces. To be more detailed, the key distinction amongst both processes is that, only recrystallization nucleation must determine some characteristics that explain how, why, where and in which direction the transformation[33] begins.

Recrystallization nucleation has to be addressed in terms of three main instability criteria. The first criterion is stated as thermodynamic instability criterion due to the presence of a deformation stored energy. The second criterion is known as the kinetic instability which arises due to the formation of mobile HAGBs. The third criterion is referred to mechanical instability due to the driving force gradients observed across the HAGBs [33]. The recrystallization nucleation sites are those that contain microstructure inhomogeneity due to the induced deformation which is known to accumulate at grain boundaries and triple junctions [10].

From the literature study, we can observe that there are 2 main mechanisms involved for the SRX phenomenon, namely: nulceation by continuous sub-grain growth and strain-induced-boundary-migration(SIBM), shown schematically in Fig.2.5. Using

the detailed information available in the literature [15][33], the the following points for the SIBM and the sub-grain growth mechanism can be concluded:

- SIBM is known to occur for deformation strains upto 0.4, as confirmed by Hansen et al.[34], whereas sub-grain growth occurs at higher deformation strains since the accumulation of misorientations is a key requirement.
- SIBM occurs in low, intermediate and high SFE materials, whereas sub-grain growth is favoured in low SFE materials [35]. This differentiation could be crucial with respect to the nucleation mechanism possibilities for Ni-30Fe alloy.
- SIBM occurs during the hot working of the material and is dependent on the deformation strain, whereas sub-grain growth requires a profitable lattice curvature for mobility of the sub-grains [33].
- Finally, both these mechanisms require a heterogeneous sub-grain size distribution and a stored energy deformation gradient between two grains for bulging to occur.

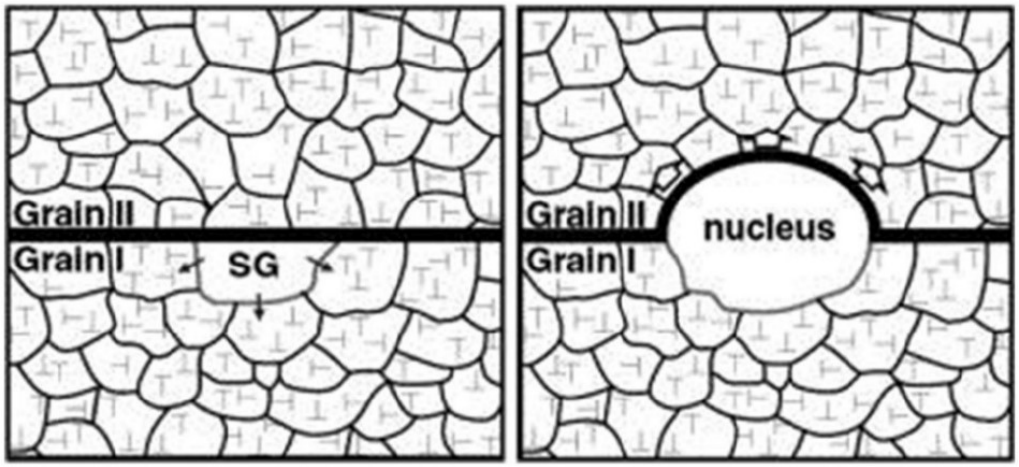

FIGURE 2.5: **Recrystallization Nucleation mechanisms for SRX by sub-grain growth (left) and SIBM(right)[9]**

Therefore, for the purpose of this project, the dominating nucleation mechanism is predicted to occur by SIBM, which can be experimentally validated in this research study.

With respect to nucleation sites for Ni-30Fe alloy, Beladi et al.[10] confirmed that the nucleation site was observed at triple junctions and grain boundaries (shown in Fig.2.6(a)). The triple junctions can consist of different types of boundaries, namely: Σ3, Σ9, coincidence site lattice(Σ) boundaries and random(R) boundaries. These different boundaries can form a combination of triple junctions such as: Σ3-Σ3-Σ9, R-R-R, Σ-R-R, Σ-Σ-R and Σ-Σ-Σ [10]. During SRX, it is observed that the triple junctions with a configuration of Σ-R-R are known to be predominantly present for the Ni-30Fe alloy, as shown in Fig.2.6(b) for two different temperature conditions. Therefore, the presence of majority of triple junctions containing one sigma boundary could be influential for the initiation of recrystillization nucleation.

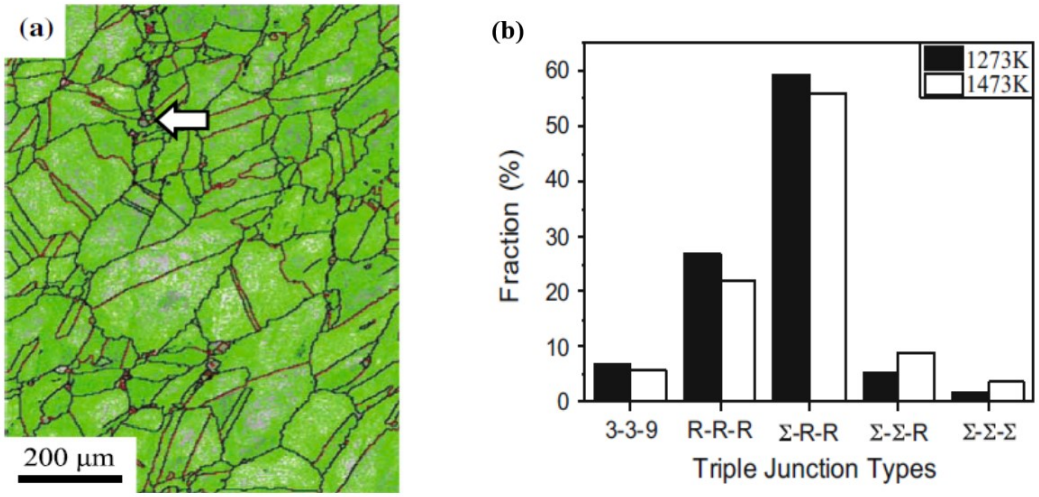

FIGURE 2.6: **(a)EBSD map of a Ni-30Fe alloy after deformation of 0.3 strain and 1000°C, to indicate the recrystallized nucleation site; (b)Triple junction categories during static recrystallization for 1273K and 1473K for the Ni-30 Fe alloy[10]**

2.4.2 Nucleation Rate: Framework modelling

The deformed austenite microstructure is presumed to comprise of a statistical distribution of sub-grains. The literature[11] states that the size distribution of the sub-grains stays identical during sub-grain growth. Then, the average sub-grain size grows at a velocity, V_{SG}, and a sub-grain mobility, M_{SG}, during the annealing time, allowing an expression, as shown in Eq.2.8 [11]. The mechanism related to this sub-grain growth which is explained above in subsection 2.4.1.

$$\langle r(t)\rangle = \langle r(0)\rangle + \int_0^t M_{SG} V_{SG}\, dt \tag{2.8}$$

where, $\langle r(0)\rangle$ is the initial average subgrain radius, and $\langle r(t)\rangle$ is the average sub-grain radius at time, t. Now, based on the Bailey-Hirsch nucleation criterion [11], the recrystallized nucleus is developed only when the driving force is able to overcome the boundary curvature forces[$2\gamma_{SE}$/ r(t)]. Originally, the stored energy from Eq.2.6 is not adequate to surpass the boundary curvature force (capillary forces), since the sub-grain size present in the deformed state are exceedingly small. Nevertheless, as the sub-grains grow during the annealing time, the boundary curvature force will decline, since it is inversely proportional to the sub-grain size. Consequently, once the sub-grain reaches the critical radius as shown in Eq.2.9 [11], it attains the required driving force for nucleation to occur by, bulging into the immediate grain in the vicinity. The mechanism related to this recrystallization nucleation process is described as SIBM (described in section 2.4.1).

$$r_c = \frac{2\gamma_{SE}}{\frac{1}{2}\Delta\rho_{GND} G b^2} \tag{2.9}$$

where [11], $\Delta\rho$ is the dislocation density difference between two grains. Since it is experimentally difficult to obtain the dislocation density between two sides of a grain boundary, here, $\Delta\rho_{GND} = 0.5\rho^*_{GND}$ (where, ρ^*_{GND} is the global GND density). The value of 0.5 is selected as an intermediate value for an extreme case where the

dislocation density is the same in both grains, and the other extreme case, where the grain boundary near one grain is without dislocations. The specific grain boundary energy,γ_{SE}, has been obtained using the Read-Shocley equation[36] as $0.712 J/m^2$, for the Ni-30Fe alloy. The other variables, G and b in Eq.2.9, have been defined previously in section 2.3.

There is a decrease of the stored energy observed as a consequence of static recovery (as seen from the subsection 2.3.1). So, since the global dislocation density is reduced and consequently its driving force, [11] this makes the critical radius for bulging at the grain boundary an increasing parameter with time. This leads to a competition between the critical sub-grain size necessary for bulging into the neighbouring grain (as seen in Eq.2.9), and the generalized sub-grain growth (as seen in Eq.2.8).

The minimum strain required for the recrystallization process to occur in Ni-30Fe alloy is above 0.03 [15]. When the applied deformation is lower than this, then it is not possible for any of the sub-grains within the microstructure to reach the critical size as required from Eq.2.9 [11]. So, here the nucleation process does not occur, even by the predicted nucleation mechanism, as shown in Fig.2.7(a). On the contrary, deformation strains at 900°C, such as, $\epsilon = 0.2$, allows the formation of sub-grains within the microstructure which would reach the necessary critical value, r_c. Finally, the larger sub-grains bulge into the grain in the vicinity, which as a result, indicates the nucleation of recrystallization, as graphically identified from Fig.2.7(b) [11]. This proves the involvement of the SIBM mechanism for the recrystallization nucleation process, schematically shown in Fig.2.5. The parameter, ϵ_c, indicated in Fig.2.7 is different from the earlier defined minimum critical strain for the onset of dynamic recrystallization.

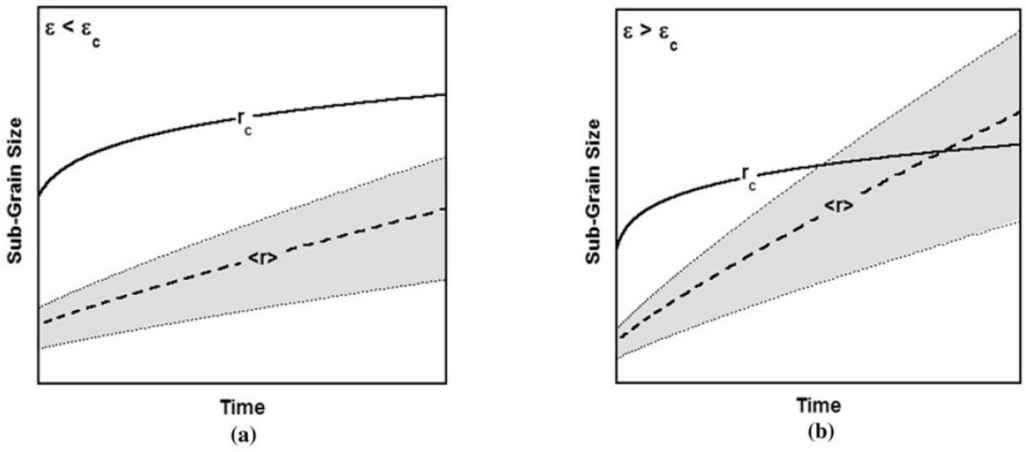

FIGURE 2.7: **Time advancement with respect to sub-grain size and critical radius of nucleation when the applied deformation strain is less(a) and more(b) than the minimum strain necessary for nucleation [11]**

The information of the size distribution of sub-grains permits the estimation of the sub-grains that have the capability to form nuclei. The Rayleigh distribution described by Hansen et al. [34], is known to provide an adequate characterization of the sub-grain size distribution as formulated in Eq.2.10.

$$p(\chi) = \frac{\pi}{2} exp(-\frac{\pi\chi^2}{4}) \tag{2.10}$$

where, χ is the normalized sub-grain size. Then, it is possible to calculate the sub-grain fraction that achieves the minimum critical size, f(t), as shown in Eq.2.11 [11].

$$f(t) = \int_{\chi c(t)}^{\infty} P(\chi)\, d\chi \tag{2.11}$$

This function can be written analytically in terms of Eq.2.12 [11].

$$f(t) = exp(-\frac{\pi}{4}\chi_c(t)^2) \tag{2.12}$$

It is important to note that only the sub-grains that are in the vicinity of the grain boundaries can form viable nuclei since the recrystallization process is presumed to take place by SIBM. The amount of prospective nuclei can hence be valued as the deformed grain boundary area per unit volume, S_v [11], which is then divided by the cross-sectional area of the critical sub-grain [11], A_{nucl} (described as the average area of a viable nucleus = πr_c^2). The combination of this theory in Eq.2.11, with a volume fraction of available sites that can undergo recrystallization at a given time, would provide the rate of nucleation, as seen in Eq.2.13 [11].

$$\frac{dN}{dt} = \frac{df}{dt}\frac{S_v}{A_{nucl}} F_n(t) \tag{2.13}$$

Yoshie et al.[14], arrived at an empirical equation for S_v (deformed grain boundary area per unit volume) as shown in Eq.2.14.

$$S_v = (\frac{24}{\pi D_i})(0.491e^{\epsilon} + 0.155e^{-\epsilon} + 0.143e^{-3\epsilon}) \tag{2.14}$$

where, D_i is the initial grain diameter before rolling and ϵ is the true strain applied. The function $F_n(t)$, in Eq.2.13, is presented so that the gradual consumption of nucleation sites can be considered. Basically, it signifies the fraction of the outer grain boundary shell that is still free for nucleation [11]. So, $F_n(t)$ can be defined as the non-recrystallized fraction of the boundary shell, as shown in Eq.2.15 [11].

$$F_n(t) = 1 - \frac{V_{rex}}{4\pi {R_i}^2 \delta} \tag{2.15}$$

Essentially, the unrecrystallized fraction is obtained by taking the inverse of the total recrystallized volume, V_{rex}. Then, δ is the grain boundary thickness, assumed as 1nm for the Ni-30 Fe alloy [37], and R_i is the initial radius of the deformed grain. When the non-recrystallized volume fraction, $F_n(t)$ is equivalent to zero, it is assumed that site saturation is attained. Consequently, the nucleation rate would also be zero (based on Eq.2.13) once site saturation is obtained, and the SRX phenomenon would thereafter transition solely into a grain growth process. Hence, this concept of site saturation can be used to describe the completion of the recrystallized nucleation process, as there is no more volume in the material available for a nucleus to develop. Finally, even though the grain growth process is beyond the scope of this report, it can be comprehended from the literature [11], as centered on the mobility of the HAGB which is dependent on the temperature and the remaining stored energy in the material.

2.5 Former Twin Boundaries and Annealing Twins

There are two types of twin boundaries known as the coherent twin(CT) boundary and incoherent twin(IT) boundary. CT boundary is formed by the two adjacent crystal lattices in the {111} plane with a mirror plane in between them, whereas the IT boundary is formed on any other plane. In austenitic steel, the twin boundary misorientation can be achieved by rotation of 60°around the <111> axis direction of the parent grain [13]. These twin associated crystal lattices have coincident atoms, forming a CSL. For instance, when 1 in 3 lattice points coincide with each other, it provides a twin relationship, also known as $\Sigma = 3$ Coincident Site Lattice (CSL).

Former twin boundaries are those twins present before deformation in the Ni-30Fe alloy, but then undergo changes in misorientations of the tilt and twist boundaries due to a deformation strain, and therefore suffers loss in their grain boundary character. However, annealing twins are formed during the recovery, recrystallization or grain growth of the FCC structured metals (such as austenite steels) comprising of low to intermediate SFE. The stacking sequence in FCC lattice is commonly known as ABC stacking sequence which comprise of {111} planes. These {111} planes of the ABC sequence occur as a nucleation process on top of one another. Now, when a different plane of atoms are stacked instead of the normal stacking sequence, it generates a stacking fault error. This has been illustrated in Fig.2.8 and is described based on the growth accident theory. From Fig.2.8, we can infer that the stacking fault is changed to B plane of atoms instead of A. This could eventually turn into a twin if an A plane of atoms is stacked above the B plane with a C plane(shown as red plane in Fig.2.8) behaving as a mirror for the twin. For the new A plane to be added, the migration of the grain boundary must occur in the opposite direction to the centre of curvature, as shown by the arrow in Fig.2.8. Hence, this twin formation could occur during the annealing treatment when boundary migration takes place.

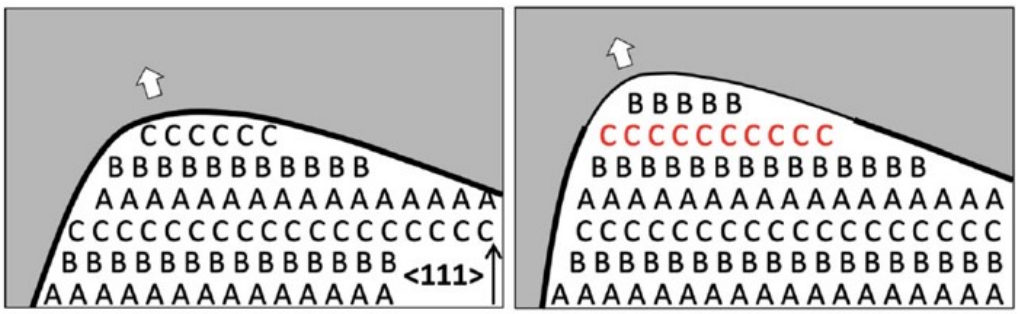

FIGURE 2.8: **The growth accident model by Gleiter [12]**

There has been importance in enhancing the properties of metallic alloys by regulating the grain boundary character and maximizing the quantity of low Σ boundaries (CSL boundaries such as first order $\Sigma 3$ twins and second order $\Sigma 9$ twin orientations) through thermomechanical processing [33]. When $\Sigma = 1$, it is a coincidence site lattice boundary that is referred to as a LAGB [13]. So, the growth accident theory indicates that due to a stacking error, a CT boundary develops at a migrating grain boundary, which is supported by many recent experimental studies [38] [39] [40].

These literature studies have shown that Σ3 boundaries that forms twin boundaries have the lowest grain boundary energy and hence are favourable in the Ni-30Fe alloy. Furthermore, the migrating distance and migrating velocity of the grain boundary are twofold crucial factors for annealing twin formation. The numerical models[13](Gleiter's model and Pande's model,[41] [42] respectively) for the growth accident theory, were only created to foresee the annealing twin density in the grain growth process and is not competent to calculate the density of the annealing twins in the recrystallized process.

2.5.1 Quantitative and Statistical Analysis of Annealing Twins

Annealing twins are known to be generated easily in C-Mn steels, since the stacking fault energy (approx. 0.75 J/m^2) of the material is intermediate. The quantification of the annealing twins is based on their density along the <111> axis by a misorientation of 60°and a tolerance of 8.66° based on Brandon criterion [43].

Using the study conducted by Jin et al.[13], to determine the annealing twin density (m^{-1}) in the recrystallized regions of the material. The EBSD maps are used for observing the recrystallized grains, as shown in section 4.3. Thereafter, the density of the annealing twins can be attained as shown in Eq.2.16 [13].

$$Twin\ Density = \frac{2L_{tb}}{\pi S_{re}} \tag{2.16}$$

where, L_{tb} is the length of the annealing twin boundary and S_{re} is the surface area of the recrystallized grains. The ratio between the variation in average grain size and the increment of time between two consecutive EBSD[13] mappings is essential in estimating the average velocity of migration.

The study by Jin et al.[13] is indicative that during the beginning of the recrystallization process, the twin density increases as the recrystallization fraction increases, and the highest value of annealing twin density relates to the highest value of grain boundary migration velocity. Secondly, during the[13] recrystallization process, both the average grain size and the stored energy positively impacts the grain boundary migration velocity, which is known to coincide with the Growth accident theory. Thirdly, the remainder of the stored energy level declines constantly during the recrystallization process as seen in the subsection 2.3.1. So, the initial positive impact of the stored energy[13] with respect to the annealing twin density diminishes with time.

The literature[13][40] suggests that there are lesser annealing twins generated by the end of the recrystallization process, which is understandable since the average grain boundary velocity is shown to be significantly smaller at the end rather than at the start of the recrystallization process [13]. So, this validates that the probability for the annealing twin development to be directly proportional to the migration velocity based on the growth accident theory[13]. Additionally, when considering the grain growth process which has a recrystallized fraction greater than 80%, the amount of generated annealing twins is approx. 10%. The progression of annealing twin density is predominantly analyzed by the creation, inter-linkage, or the loss of the existing twins [13].

In Fig.2.9(a) and (b), two different topological changes in the annealing twins can be observed by the black and blue circles. In the black circle, the topological change is observed by the the Σ9 boundary merging into the the Σ3 boundary, due to the capillary forces that causes the migration of the twin boundaries. The driving force for this annealing twin change is based on the ability to have a lower interfacial energy. This decline in the interfacial energy can be attributed to transformational changes such as: total boundary length decrease, Σ9 merging into Σ3 boundary transformation, and the consumption of two triple junctions. Then in the blue circle, the topological change is observed by the incoherent twin boundary that merges into a coherent twin boundary, and the Σ9 interface boundary which is between the coherent and incoherent portion fades away. This transformational change is energetically favourable since both the incoherent twin boundary and the Σ9 have larger interfacial energy than coherent twin boundary [44].

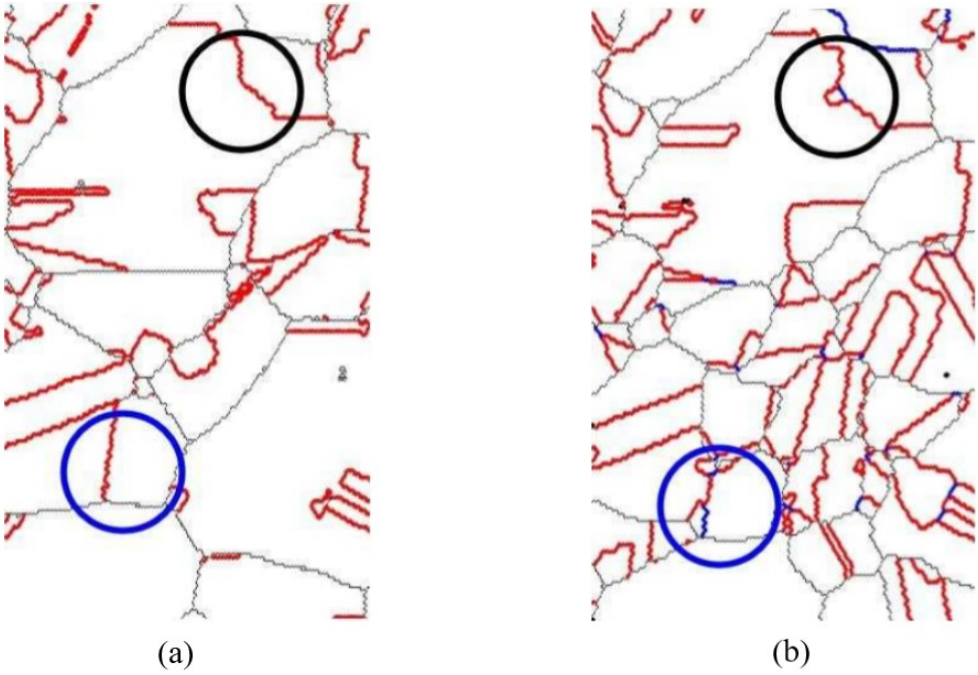

FIGURE 2.9: **(a) & (b): EBSD maps of two consecutive annealing times where, thick Red lines: Σ3 boundaries, Thick Blue lines: Σ9 boundaries, Thin Black lines: HAGB [13]**

So, the evolution of Σ3 and Σ9 boundaries is essential to reduce the total interfacial energy. Now, for nucleation to occur, the grain boundaries must begin bulging during or after annealing treatment, where each grain boundary type is known to have a bulging amplitude [10]. Since, there is a reduction in the interfacial energy of Σ3 and Σ9 boundaries, the bulging amplitude tends to be extremely small in comparison to the HAGB. However, within the grains, the presence of such Σ3 and Σ9 grain boundaries at the intersections of slip bands and former twin bundles could behave as a nucleation site. Generally, this nucleation site is expected to retain the orientation of the deformed matrix itself [45]. The study shown above for the development of annealing twins during recrystallization and grain growth is conducted with a 304L austenitic stainless steel. Therefore, similar investigation is required with the modelled Ni-30Fe alloy to predict the behaviour of annealing twins in C-Mn steels.

2.6 Recrystallization Behaviour

The recrystallized nucleation of grains do not occur in the conventional manner but instead grow from pre-existing sub-grains, disregarding the classical nucleation theory [46]. So, initially, there is an "incubation time" for the recovery process where the sub-grains with LAGB (low-angle grain boundaries [$< 1\ ^{\circ}$misorientation]) commence to dislocation accumulation and develop higher misorientation with regard to their neighbouring grains. This increase in misorientation enhances the boundary mobility and hence the growth rate of the sub-grain rises. If one subgrain in the microstructure turns out to have higher dislocation density, a larger subgrain size or positive orientation, then that subgrain will be able to grow more quickly. Finally, as the growth advances, its grain boundary develops higher misorientation about the surrounding grains until eventually, it is identified as a completely new strain-free grain.

The change of the microstructure in terms of recrystallization of an austenitic alloy, due to strain deformation and heat treatment can be understood using a Cellular Automata (CA) simulation model. This can be combined with the EBSD experimental technique, which would offer the usage of actual microstructural information that can assist in validation and accuracy of the predicted model. The recrystallization model and microstructure evolution can be best described using the main components such as: (i) The initial grain size distribution (to develop microstructure heterogeneity for recrystallization nucleation) and static annealing conditions to achieve the deformed state, ii) The orientation gradient for deformed grains, critical sub-grain size and stored energy for the nucleation criteria (nucleation rate, mechanism and site), iii) The spatial distribution of the recrystallization nucleation sites and the recrystallized volume fraction for the grain growth kinetics [45].

2.6.1 Recrystallization Kinetics

The kinetics of recrystallization can be observed as shown in Fig.2.10(a). Initially, the point where the nuclei develop is marked as time, τ, also referred to as the incubation time. The incubation time (nucleation initiation) is dependent on the recovery effects and the spatial distribution of grain boundaries and triple junctions in the material. Rehman et al. [11], showed that the initial nucleation incident transpires after 3 seconds(τ) of holding, and can be achieved by the largest subgrain in the deformed grain that reaches the critical radius(r_c) for bulging, as shown in Fig.2.10(b).

Following the nucleation initiation stage, there is a rapid increase in the recrystallized volume fraction [45]. The preliminary increase in the rate of nucleation implies the fact that a greater number of sub-grains are achieving the critical radius for bulging as a consequence of the SIBM mechanism[11], as observed in Fig.2.10(c).

Thereafter, the grain growth of the nuclei begins with a constant growth rate consuming the deformed matrix. The kinetics are noticed to decelerate substantially after nearly half the deformed grains are consumed and transformed. The stagnation or decline in the recrystallization rate that follows can be attributed to the consumption of free nucleation sites at the grain boundary and triple junctions. A mathematical approximation can be derived in order to calculate the recrystallized

volume fraction, X_{re}. This derivation is a simplified form for the recrystallized volume fraction using the JMAK model, which can be written in the form of Eq.2.17 [47].

$$X_{\text{re}} = 1 - exp(-Kt^n) \tag{2.17}$$

where, X_{re} is the recrystallized volume fraction at a time, t. The value of K is the thermally activated rate constant that represents the nucleation and growth rates, and n is the Avrami constant that indicates the transformation process. The parameters K and n [11] are presumed to be constant at a provided temperature.

Previous effort [48] [47] [49] related to this subject has steered the advancement of effective semi-empirical relationships [11] that explain the interactions between recovery and recrystallization with good precision, as modelled by Rehman et al [11]. The simulation of recrystallization kinetics with various initial microstructures and spatial distribution of nuclei sites can be compared with the experimentally achieved kinetics, conducted by Haase et al. [45]. However, Haase et al.[45] neglects the effects of recovery which is known to influence the evolution of the critical sub-grain size with time, as explained in subsection 2.4.2.

Therefore, the parameters such as the dislocation density, stored energy and nucleation rate do not remain constant and hence evolve with time due to recovery [11]. Finally, this influences the avrami constant which is known to be greater than 2 when the recovery effects are not taken into consideration. In continuation to the JMAK model in Eq.2.17 and the defined parameters of K and n, the equation can be re-written as shown below in Eq.2.18 by taking the logarithm on both sides.

$$ln[-ln(1 - X_{\text{re}})] = n\ ln\ t + ln\ K \tag{2.18}$$

On using the data in a plot as a linear fit of ln [-ln (1-X_{re})] against ln t, the n value can be estimated from the slope obtained and the K value can be obtained from the intercept of the plot, as seen in Fig.2.10(d). So, the avrami constant that is calculated when the incubation time is taken into account is, 1.29 (shown in Fig.2.10(d)). This is in good agreement with the experimental results which is found to be between 1 and 2, as it is taking into account the recovery effects [11].

Besides the JMAK model, there is an empirical relationship concerning the recrystallization fraction X_{re} and interfacial area A between the recrystallized and non-recrystallized grains, known as the Speich-Fisher (SF) equation. The SF equation can be written, as shown in Eq.2.19.

$$\frac{X_{\text{re}}}{1 - X_{\text{re}}} = bt^m \tag{2.19}$$

Here, the constant, m, can be related with the Avrami constant. The matching of the JMAK equation with the experimental results is marginally better only during the early stage of recrystallization process, whereas the similarity of SF equation with the experimental results is marginally better in the subsequent stage of annealing [28]. However, it is important to note that this study[28] involved the presence of precipitates, and so results can deviate for the SRX phenomenon free-precipitate case in Ni-30 Fe alloy.

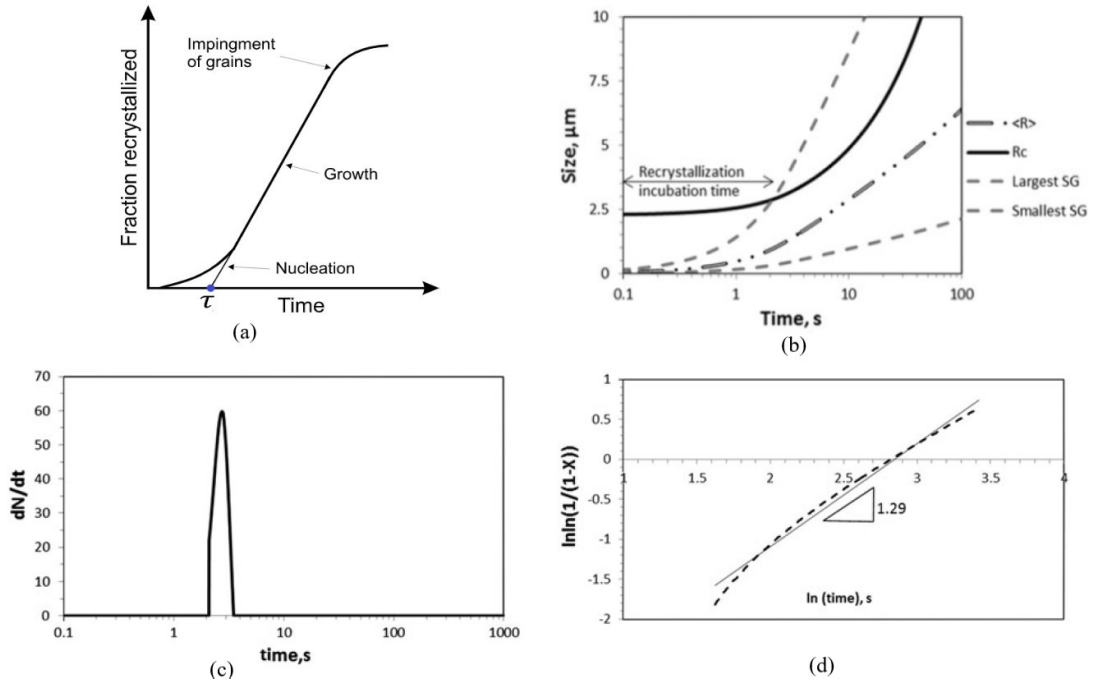

FIGURE 2.10: **(a)Recrystallization kinetics and incubation time (b) Evolution of of different sub-grain sizes, and the critical radius for bulging. (c) Evolution of rate of nucleation. (d) Avrami constant evolution [11]**

2.6.2 Grain Size Distribution

The theoretical addition of the heterogeneous nucleation sites to the classical JMAK theory was introduced by Villa and Rios [50]. The study conducted by Cahn used the decreasing Avrami component (n), to show the deceleration of the recrystallization kinetics due to selective impingement of grains from heterogeneous nucleation. However, the Avrami component is known to be influenced by the difference in the the stored energy between grains, and hence cannot be used as the sole measure of the spatial microstructural heterogeneity for the nucleation stage [45].

Haase et al. [45], utilized a special neighbouring distribution function, G, to distinguish in greater detail regarding the discrepancies from the homogeneous spatial arrangement of nuclei. The utilization of the G function, showed that the nucleation taking place at grain boundaries deviate substantially as compared to the random bulk nucleation[45]. More rapid impingement of nuclei during nucleus growth is probable at triple junctions and nuclei necklaces at grain boundaries, due to the high likelihood of one nucleus facing another within the critical radius. This is proven by previous CA based studies [51], where a larger amount of quick clustering of nuclei leads to a deceleration of recrystallization kinetics. Hence, this implies that assuming the presence of heterogeneous nucleation sites is essential for a credible simulation of recrystallization in the austenitic alloy [45]. Additionally, the morphology of nuclei clusters, arrangement and shape of recrystallized grains at grain boundaries for 25% and 50% recrystallized volume fraction in the experimental results[45] is in better agreement with the non uniform grain size used in simulation, rather than the microstructures developed from uniform cuboidal grain sizes.

Due to the early impingement of competitive nuclei at triple junctions, the refinement of grain occurs by restricting their growth at such preferred nucleation sites, which have a high nuclei density[45]. The nuclei clusters forming at triple junctions are known to propagate by preferential growth along the grain boundaries that have high stored energy. The final recrystallized grain size after all the deformed grains are consumed can be expressed, as formulated by Sellars and his coworkers in Eq.2.20 [52].

$$D_{\text{rex}} = 0.5 \frac{{D_0}^{\text{n}}}{\epsilon^{\text{p}}} \tag{2.20}$$

where n= 0.68 as obtained from Fig.2.11. The other parameter p is a function of temperature and strain. The effect of strain can be influenced by the deformed grain boundary per unit volume (S_v), as defined in Eq.2.14. Since recovery is known to influence the number of nuclei formed, based on the defined nucleation model in subsection 2.4.2, it is difficult to have an expression for p. It is assumed to be 1 for a C-Mn steel [11].

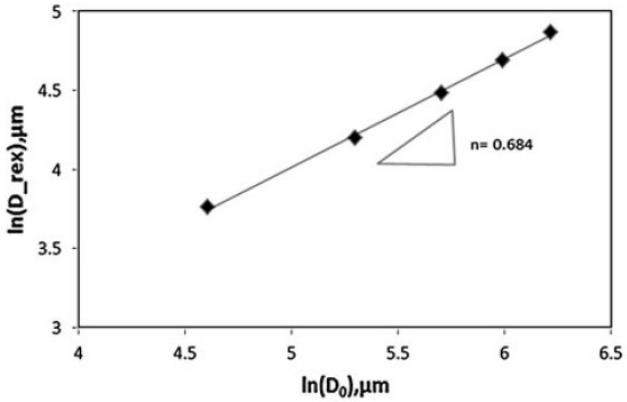

FIGURE 2.11: **The dependency of recrystallized grain size on the initial grain size for a C-Mn steel [11]**

The literature suggests [45] that the nuclei formed as clusters at the triple junctions, would finally have a recrystallized grain size distribution smaller than the average recrystallized grain size, due to impingement of nuclei. However, the nuclei with mobile HAGBs formed at regions of less nuclei density, are known to have the energy advantage and preferred growth rate to consume the surrounding deformed grains, thereby forming larger recrystallized grains than the average recrystallized grain size. The average recrystallized grain size distribution is finally dependent on the grain size distribution before deformation, so that the different nucleation sites are heterogeneously present for grain refinement [11].

2.7 Research Objectives

The primary agenda with this research study is to enhance the hot-rolling of C-Mn steel at an industrial scale using low deformation conditions. So, the main research objective is to experimentally study the SRX phenomenon, by evaluating the nucleation related processes and kinetics that occur after deformation of the austenite phase in steel. However, the austenite recrystallization kinetics are difficult to investigate experimentally, due to solid-state phase transformations of steel during

cooling to room temperature. Therefore, after conducting the literature study, it is evident that the best model alloys to examine SRX are those austenitic alloys such as, Ni-30Fe alloy, that do not showcase visible phase transformation during their hot working over a broad extent of temperatures. Since the theory behind recrystallization is well established, the type of research utilized is a practice-oriented research that is aimed at evaluating the static recovery and recrystallization after initial deformation of the alloy, using an experimental approach. The experimentation methods utilized in this research is a combination of laboratory techniques to induce deformation(Dilatometry) and conduct crystallographic measurements(EBSD), followed by application of a computerized programme(MTEX software) to analyze and obtain results from the measured data.

Initially, a desk-research approach is conducted based on the literature review, to describe the available information for SRX, identifying gaps and formulating the research plan. The sub-research objectives for this practice-oriented experimental study have been stated below:

- To develop, analyze and select an accurate recrystallization separation technique that considers the annealing twins and LAGB regions within a grain. Additionally, the quantification and increase in twins as the annealing treatment progresses is to be described. Finally, the selected separation technique must be validated based on similar recrystallization fractions obtained with the GND density measurement procedure.

- To calculate the initial and final experimental average grain size and estimate their corresponding grain size distribution within the microstructure. Additionally, the grain-size obtained from the experiments is to be validated with the earlier work of Sellars Model [52].

- To utilize the approach from the literature [23] to measure the GND density and capture the effect of recovery within the material accurately. Additionally, the reliability of the dislocation line energy calculated per unit length of the material is to be studied using the two different physical equations for the stored energy.

- To study and discuss the dominant nucleation mechanism and sites present during the recovery and recrystallization processes. The critical size for bulging is to be estimated using the nucleation criteria available in the literature [11], and compared with the recrystallized average grain-size obtained at different time intervals. Additionally, the experimental incubation time must be compared with the calculated incubation time from the mathematical model [14].

- To measure the nucleation rate in 2D using the selected recrystallization separation method. Additionally, the nucleation rate is to be converted for a 3D microstructure using the approach from the literature [8], and subsequently compared with the nucleation modelling results obtained with the physical equations of Rehman et al [11], and observed discrepancies are to be discussed.

- To obtain the experimental recrystallization kinetics for the Ni-30Fe alloy using the validated recrystallization separation technique. The experimental recrystallization kinetics is to be further compared with the JMAK model and SF equation and their respective kinetics behaviour is to be analyzed.

Chapter 3

Experimental Methods

3.1 Overview

The experimental procedures conducted in this current research are described in this chapter. The deformation and annealing treatment of the Ni-30Fe alloy is conducted with the dilatometry technique, shown in section 3.2. Thereafter, the crystallographic information about the austenite deformed microstructure is obtained from the EBSD technique in section 3.3. Finally, the MTEX software has been utilized in section 3.4 to import the data from the EBSD scan, in order to appropriately analyze and describe the SRX phenomenon during the hot-rolling of steel.

3.2 Specimen Deformation: Dilatometry

The model alloy selected based on the literature study for this research purpose is a nickel ferrous alloy with a chemical composition of 70-wt% Ni and 30-wt% Fe. The deformation of the alloy was conducted by dilatometry testing using a Bähr A/D 805 dilatometer, with a deformation unit devised to allow a simple uniaxial deformation mode. The geometry of the specimens used in all cases was that of a cylindrical shape with a length of 10mm and diameter of 5mm. During all the deformation tests the temperature was measured using a S-type thermocouple mounted on the surface, and positioned at the mid-length of the specimen.

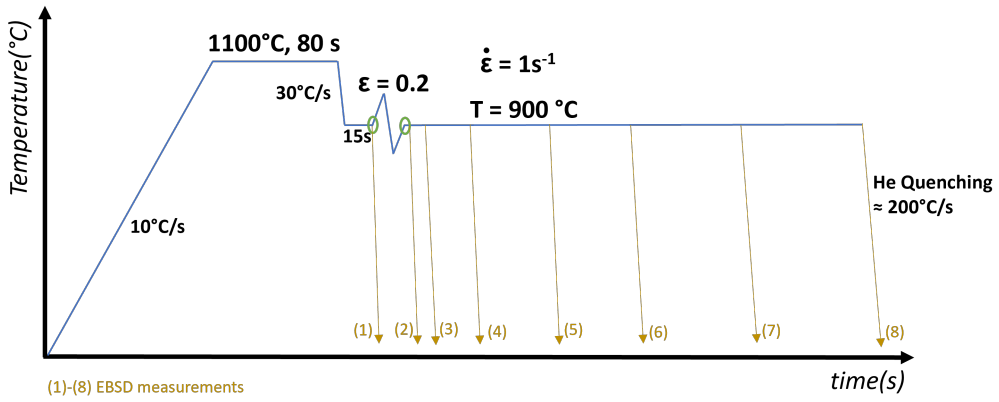

FIGURE 3.1: **Deformation-Dilatometry procedure for the cylindrical Ni-30Fe alloy specimen**

For all the Ni-30Fe alloy specimens, initially an austenitisation heat treatment is conducted at 1100°C for 80s prior to rapid cooling at 30°C/s to obtain a deformation temperature of 900°C. Thereafter, an uniaxial compression deformation mode was

applied to the austenitic microstructure at a strain rate of $1s^{-1}$. Each specimen was deformed in compression at a low strain condition of up to 0.2. Immediately after the deformation, each sample were held at the annealing temperature of 900°C for different time intervals (1s, 2s, 10s, 50s, 100s, 200s and 1000s) to capture the different stages of the SRX phenomenon. Finally, the specimens were quenched to room temperature using helium at a rate of 200°C/s. The schematic representation of the deformation procedure is shown in Fig.3.1, where the quenched samples were further investigated using the EBSD technique.

3.2.1 True stress-strain curves

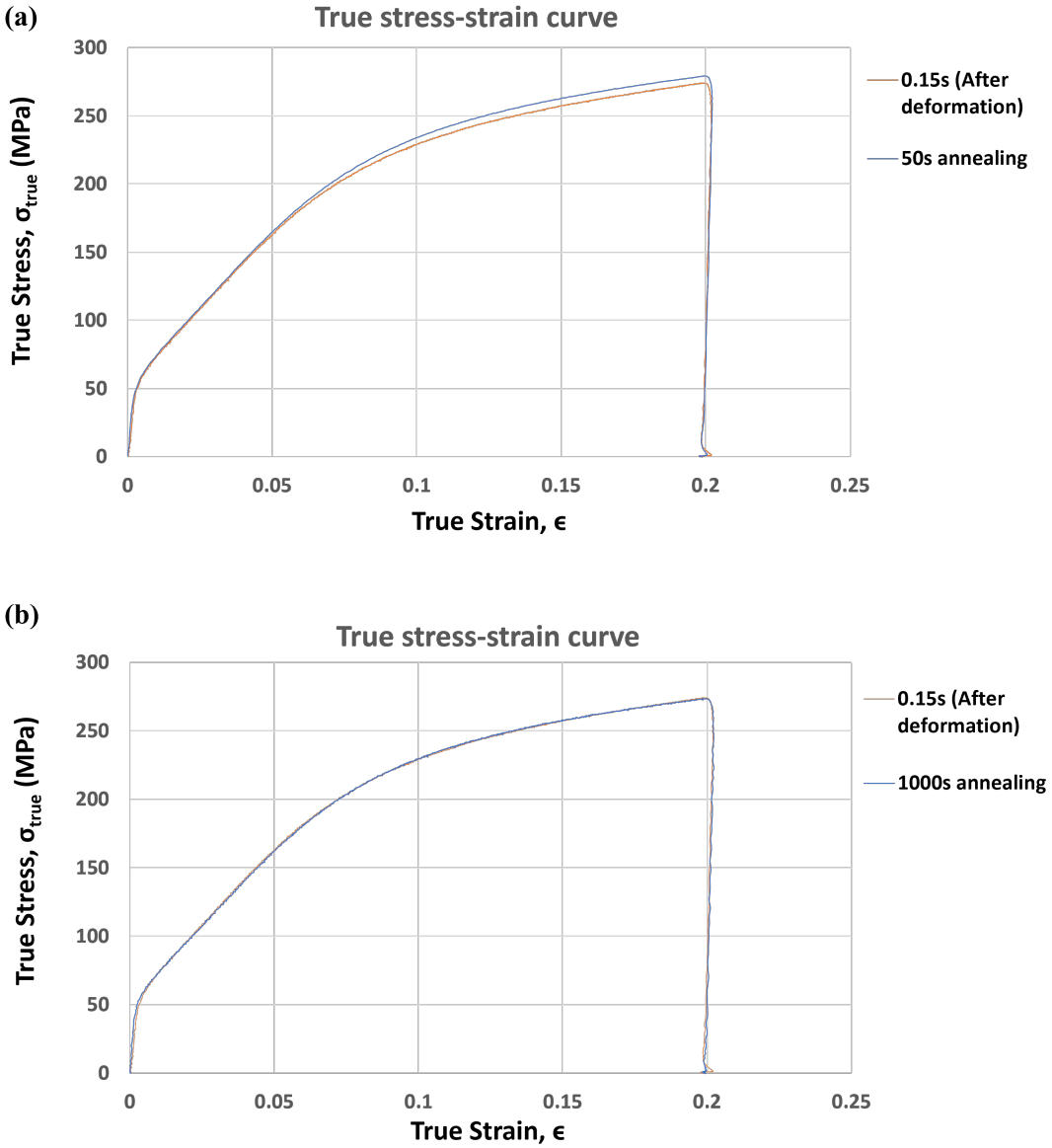

FIGURE 3.2: **Experimental true stress-strain curves for the investigated Ni-30Fe alloy after uniaxial compression. The true stress-strain values for the after deformation specimen are compared with (a) 50s annealed specimen and; (b)1000s annealed specimen**

The deformation behaviour of austenite at different time intervals of the annealing treatment and upto a strain of 0.2 has been shown above in Fig.3.2. The different annealed samples are expected to have a similar flow-curve behaviour, since the material composition, cooling rate, strain rate and annealing temperature are held at constant defined values. Fig.3.2(b), depicts the general flow-curve behaviour observed, where the after deformation and final annealed specimens are super-imposed to confirm similar behaviour. However, there is a slight deviation observed for the 50s annealed sample, as shown in Fig.3.2(a). Therefore, future discrepancies in results obtained with analysis of the 50s annealed specimen can be accounted to the slight experimental deviation produced from the deformation-dilatometry technique.

3.3 Electron Backscattered Diffraction (EBSD) technique

Polycrystalline microstructures can be quantitatively characterized by a powerful technique known as EBSD. This technique provides a desirable spatial resolution along with high accuracy for the determination of the crystallographic orientation and their corresponding changes after deformation. Therefore, this tool makes it highly irreplaceable on comparison with other characterization tools, and is hence utilized in this research study to capture the SRX phenomenon occurring in Ni-30 Fe alloy. This section describes the operating principle, resolution and important parameters involved in the technique. The sample preparation procedure is also shortly described, before the scan results from the technique are analyzed further in section 3.4.

3.3.1 Operational Principle, Resolution and Main Parameters

The EBSD system utilized in this research study is perpendicularly joined to the tilt axis of the microscopic stage, of a Zeiss Ultra55 FEG-SEM. The produced EBSD pattern is detected by the electro-fluorescence impact on a phosphor screen. This pattern is then captured by a digital camera that contains detectors, which is connected to the computer. The EBSD technique is described in more detail below.

Initially, the sample preparation procedure must be conducted, since the EBSD technqiue is more sensitive than other imaging techniques, such as optical microscopy, since the beam parameters and atomic number are highly influential for the measurements. The sample preparation necessitates thorough elimination of any production induced deformed layers at the surface. This is typically accomplished by traditional mechanical grinding with a final polishing stage produced from micron-size abrasives. Grinding of the cylindrical specimen is conducted with 240 grit SiC paper starting until a planar surface is obtained. Subsequently, other grit SiC papers of 800 and 1200 is also used to ground the sample further. Finally, the sample is polished by 3 micron and 1 micron colloidal silica (OPS) suspension, which consists of SiO_2 particles that allows to produce a smooth, polished and slightly etched surface.

The Ni-30Fe alloy prepared specimen that is placed on the microscopic stage is tilted further until the specimen surface obtains a certain angle. This required angle is utilized so that the specimen is tilted towards the phosphor screen, also referred to as the grazing angle. The grazing angle is essentially around 20 degrees and is the angle between the specimen surface and the incident beam, in order to ensure moderate spatial resolution and optimum diffraction conditions.

Using these geometric conditions, the primary electrons enter the specimen surface and some of these electrons escape. However, a prominent fraction of these electrons undergo elastic collisions with the atoms in the specimen. This process of multiple collisions produces scattering of electrons that have a kinetic energy similar to the incident beam. According to the Bragg's diffraction[53], these scattered electrons form the Kikuchi diffraction pattern, which can be made visible by the electron fluorescence when the backscattered electrons hit the phosphor screen. The backscattered electrons signal originates from a tear-drop volume with a size of 1 μm, which is dependent on the accelerating volatge(20V – 30 kV) and the atomic number(Z) of the Ni element.

From Fig.3.3, schematically illustrates the orientation of a certain FCC crystal and the incident primary electron beam which gets diffracted from the 110 plane. The electrons that does follow Bragg's condition for the particular plane will be diffracted into diffraction cones. The acceleration for the SEM is determined to be approximately 30kV, and hence the diffraction angle(2θ) is around 1.4°with a electron wavelength of 0.007nm. Straight lines are observed from Fig.3.3, as a result of the intersection of the cones on the phosphor screen. Additionally, the bands that are visible can be understood as the diffraction plane extensions that have emerged from the FCC lattice. It is important to note that only the elastically scattered electrons that follow Bragg's condition form these patterns. By contrast, the diffused pattern in the background is a result of the in-elastically scattered electrons which have partly lost their energy. Finally, the different patterns are captured by the CCD (Charge-coupled device) camera, and the data is transferred to the computer which automatically locates the positions of each Kikuchi band.

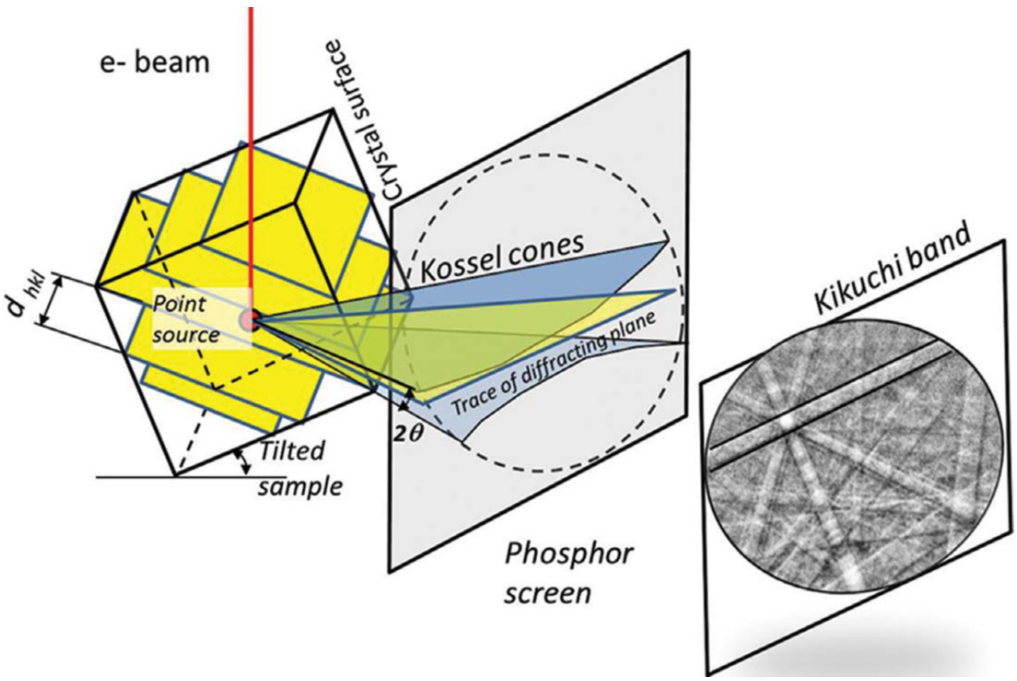

FIGURE 3.3: **Schematic representation of an electron beam diffraction from the {110} plane and the subsequent development of Kikuchi patterns on a phosphor screen [6]**

The generated diffraction pattern as observed in Fig.3.3 is specific and directly translates into the crystallographic structure and its corresponding orientation. Therefore, this provides information regarding the prominent planes that form the diffraction pattern and the crystallographic orientation with respect to the specimen direction. The specimen direction can be further understood in subsection 3.4.3, once the data is stored as *.ang* text file. The EBSD scan for the Ni-30Fe alloy stores a single austenite phase with the x and y pixel coordinates regarding the origination of the diffraction patterns. Then, the orientation of crystal with respect to the pixel coordinates is stored as Euler angles (ϕ_1, Φ, ϕ_2). Additionally, the file uses a parameter known as IQ, which is effectively the image quality parameter (also known as band contrast for the system software Oxford—HKL) that characterizes the contrast of the EBSD pattern correlated with each pixel coordinate. There is also a confidence index CI that defines the reliability of the obtained result (commonly known as the mean angular deviation), by estimating the difference between the measured value of the angles and the theoretical values for the FCC lattice. Finally, the parameters stored in this file are essential in plotting the different types of maps after post-processing of the data using the MTEX software.

3.4 MTEX Software

The analysis of the EBSD data can be conducted using a free add-on to the Matlab toolbox, known as MTEX. Data files such as *.ang* format can be imported into this software as matrices and arrays, and saved into a variable *ebsd*. This variable contains information regarding the composition of the minerals, symmetry, the specimen and crystal coordinate system, the orientation data, scanned area, phase maps and other necessary parameters. For clarity, only a single austenite phase is observed upon quenching to room temperature, which allows us to study the SRX phenomenon, avoiding unnecessary complexity during the analysis. Furthermore, it is important to align the specimen reference frame, based on the spatial coordinates X and Y coordinates, and the Euler Angles ϕ_1, Φ, ϕ_2. Therefore, using the available option 'convertEuler2SpatialReferenceFrame', allows us to modify and keep all the data points within the X and Y coordinate specimen reference system, even if rotation of Euler angles is required at a later stage. For the purpose of this report, the X coordinate refers to the horizontal (east) direction, whereas the Y coordinate refers to the vertical (north) direction. After the initial script is generated and edited for the desired cubic crystal symmetry(Crystallographic Point Group: 432, or Laue Group: *m-3m*) of the Ni-30Fe alloy, the detection of grains based on certain orientation threshold can be conducted. Additionally, denoising techniques must be implemented to reduce the data-noise, generated in both high resolution and low resolution EBSD scans. Finally, the EBSD maps can be plotted with colours for orientation positions, by specifying the specimen direction with respect to their crystallographic direction, which is done by using an inverse-pole-figure (IPF) colour key code.

3.4.1 Grain Detection

The grain detection and reconstruction method is ideally focused on the presence of similar orientations present beside each other, within the scanned selected region of the specimen. Initially, the entire specimen had been scanned for measurements(which can be seen by the total number of orientations before deformation in Table3.1). Thereafter, it is observed that the strain accumulation is concentrated

along the centre of the sample. Therefore,the selected region of these lower resolution scans(step size: 5μm), is used for the statistical analysis with a surface area of 3*3mm^2, approximately near the centre of the sample. For the higher resolution scans(step size: 0.5μm), *three* different regions of approximately 0.7*0.7mm^2 surface area, are selected along the centre axis of the sample, and can be differentiated and defined as: Upper, Central and Lower regions.

Grains are differentiated from each other by grain boundaries, which are lines between neighbouring orientations that exceed a misorientation threshold of 15 degrees, also known as HAGBs. Now, within each grain, it is possible that there are measurements errors with respect to indexing each pixel to a designated orientation, and hence these regions appear as *Not*-Indexed regions. The Indexed(%) regions of the specimen for the low and high resolution of the EBSD scan measurements is reported in Table.3.1 & 3.2, respectively. Finally, on using the grain function *calcGrains*, the grains are detected and stored as a variable, containing information regarding the grain-*id's*, grain-size, grain boundary and triple points.

Annealing Time(s)	Indexed orientations	Not-Indexed orientations	Indexed (%)
0	1241310	40	99.9968%
0.15	1030867	33	99.9968%
1	3006491	5	99.9998%
2	3078798	3	99.9999%
5	3039530	54	99.9982%
10	3045666	4	99.9999%
20	3016019	1	100.0000%
50	3020025	3	99.9999%
100	3045670	0	100.0000%
200	3020028	0	100.0000%
500	3028060	0	100.0000%
1000	3028043	1	100.0000%

TABLE 3.1: Indexed and Not-Indexed Regions of the low resolution EBSD scans (5microns step size)

From the EBSD scans for low and high resolution, it is clear that only a small number of pixels remain *Not*-Indexed. These regions are overlooked and left unindexed for the grain reconstruction method, since they would have negligible influence for the grain calculations. It can be observed that the higher resolution scans have a larger fraction of *Not*-Indexed regions, which is due to the noise generated from

such scans. Additionally, the high resolution EBSD scans at 5s annealing time, is observed to have the highest number of Indexed and *Not*-Indexed orientations as the EBSD measurement was conducted at a 0.3 micron step size. The measurements from this high resolution EBSD scan at 5s annealing time will not be used for statistical calculations, as it is for a smaller scanned region and has an overload of data which is complex to compute. Furthermore, the high resolution EBSD scans from 100s annealing time is observed to have a lower number of total orientations measured, which is due to a larger step size of 0.7 microns utilised. However, since the area scanned from these high resolution scans is still similar to the inital annealing time intervals, it is utilised for our statistical calculations. From these orientations in Table.3.2, we can infer that there is an exponential regression between the resolution of an EBSD scan and its corresponding orientation information measured, given that the scanned area is similar. This exponential regression for a similar scanned area of the high resolution maps, can be approximated as:
No. of orientations measured = $2E+07e^{(-4.235 * \text{step-size in microns})}$

Annealing Time	Indexed orientations	Not Indexed orientations	Indexed (%)
0.15	2264609	808	0.999643333
1	2264609	808	0.999643333
2	2264608	809	0.999642891
5	3208013	962	0.999700216
10	2264609	808	0.999643333
20	2264608	809	0.999642891
50	2264609	808	0.999643333
100	1155578	577	0.999500932
200	1155578	577	0.999500932
500	1155578	577	0.999500932
1000	1155578	577	0.999500932

TABLE 3.2: Indexed and Not-Indexed Regions of the high-resolution EBSD scans (Average of the *three* scanned regions of the specimen: Upper, Central and Lower)

Another criteria of relevance after using the *calcGrains* function, is to segregate the small grains from artefacts(scanning errors or dust particles) that are present during grain reconstruction that disrupts the data accuracy. For the low resolution scans, the pixels<=4 (here, 1 pixel is approximately $3\mu m$) are neglected for the grain reconstruction, since the extremely small grains before deformation are noticed to have a grain-size of at least $12\mu m$. This minimum criteria for the cleaning technique during

grain reconstruction is also commonly observed in other studies [54] [15]. However, it is known that the removal of these extremely small grains can significantly transform the statistical parameters such as average grain-size. Therefore, for the higher resolution scans (0.5 and 0.7 microns step size), it is essential to closely observe and select a limit for this cleaning technique. For the purpose of this study, a value of <=2 pixels has been assigned to the high resolution scans, since there are really small grains present, which coincidentally allow a normal grain size distribution in the microstructure.

3.4.1.1 Grain Oriented Spread

After the grain reconstruction procedure, the orientations that belong to every grain in the scanned region is stored in the variable *ebsd.grainId*. Then, the function *meanOrientation* is used to provide the mean orientations for all the grains in the scanned region, which can be designated as the reference orientation of each respective grainId. Following this step, the deviation for each orientation pixel in the grain with respect to the grain mean orientation can be analysed, more commonly referred to as, GROD (Grain Reference Orientation Deviation). This method helps us to calculate GROD for all the grains using the function *calcGROD*, which essentially computes the misorientation angles for each pixel to the grain mean orientation. Finally, the GOS is calculated by average of these misorientation angles to the grain mean orientation, for each grain. The utilization of this methodology to seperate the recrystallized and deformed grains is further described in subsection 4.3.1.

3.4.1.2 Kernal Average Misorientation and Grain Average Misorientation

Using Eq.2.1, the KAM values of the low and high resolution EBSD scans are stored in a variable *kam*. The KAM measurements are expected to be noisy and hence denoising techniques, as described in subsection 3.4.2 are implemented to improve data accuracy. It is also advised to select the nearest number of neighbours as greater than 1 in order to reduce the noise levels. Hence, this research study conducts the KAM measurement upto the second nearest neighbours. The KAM maps are useful in comparison with the GND density maps as observed in the literature [23], since it is expected to reveal local dislocation structures within the deformed material.

Subsequently, the GAM measurement can be obtained by directly averaging the local grain misorientation from the *kam* variable. Essentially, the procedure of GAM estimation is firstly done by selecting a particular pixel in the grain. The orientation of this pixel is compared with the neighbouring pixels upto its second nearest neighbour. The similar procedure is conducted for all the pixels within the grain. Finally, the averaged misorientation angles between these pixels, within a grain, provides us with the GAM values for each grain. The combination of KAM and GAM methodology is utilized further in subsection 4.3.2 and the accuracy of the recrystallization separation technique is analyzed based on the prior mentioned GOS technique.

3.4.2 Denoising Techniques

The orientation data obtained experimentally from the EBSD technique is unarguably known to contain measurement errors. These errors can be distinguished as random or systematic errors. Systematic errors have barely any possibility for correction with MTEX, since it occurs prior, due to incorrect calibration of the EBSD technique. However, random errors is known to exist due to the noise from the

Kikuchi pattern, which lead to deviation from the true orientation of each pixel. So, such random errors can be reduced by using certain denoising techniques, as shown in Fig.3.4.

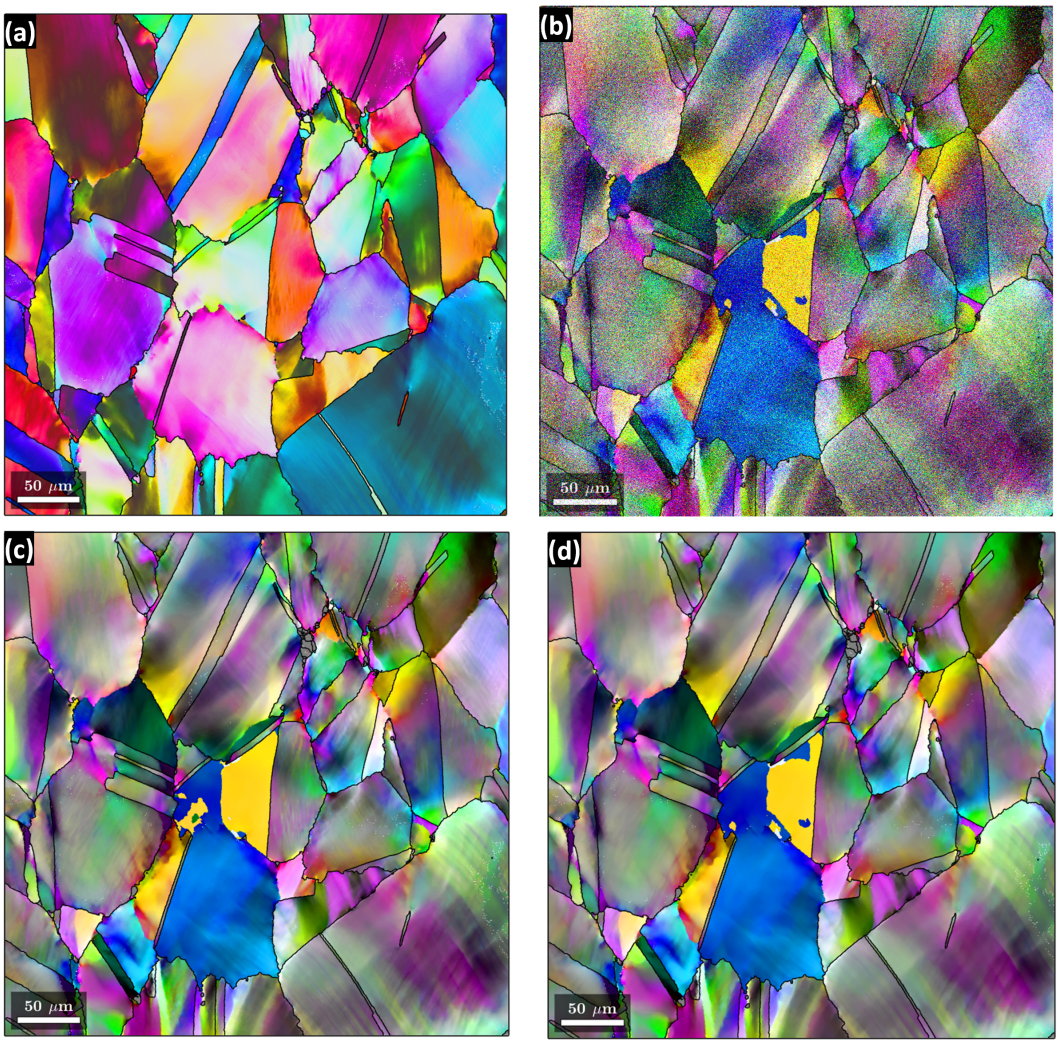

FIGURE 3.4: **(a) High resolution orientation map after deformation for Ni-30 Fe alloy; (b) Representation of noise by colourizing orientation measurements; (c) Mean Filter; (d) Half Quadratic Filter**

Initially on observation of the high resolution map after deformation of the Ni-30Fe alloy, as seen in Fig.3.4(a), the orientation map does not appear to have a large presence of noise from the Kikuchi patterns. In order to observe the noise, the orientation measurements can be colourized with relation to their corresponding misorientation to the grain mean orientations. So, from Fig.3.4(b), the deformation gradients are superimposed by digital noise from the orientation data. Filtering out of noises is possible using either the Mean filter or the Half Quadratic filter, as shown in Fig.3.4(c) and Fig.3.4(d), respectively. The former filter is the most straightforward and linear smoothing type filter. This filter considers the nearest number of neighbours, and replaces all the orientations by the mean orientation of its neighbours. However, this filter removes sub-grain boundaries and is highly sensitive to large deviations to the original map, which is observable on comparing Fig.3.4(b) and Fig.3.4(c).

Therefore, we utilise the Half Quadratic filter in this thesis project, which belongs to the group of total variation filters. The use of a total variation filter on the orientation maps establishes the denoised orientation map as a result of the noise minimization dilemma which is ideally close to the initial map, which can be observed by comparing Fig.3.4(b) and Fig.3.4(d). Additionally, this filter allows the preservation of sub-grain boundaries for extremely high resolution maps in the order of 100nm step-size. However, it is essential to know that this filter is highly dependent on the "smoothness" applied to the map(smoothing value selected here is 4), in order to produce an orientation map that is smooth, and simultaneously indicates the orientation gradients present after deformation. Finally, it is interesting to mention that there is an upgrade to the Half Quadratic filter being designed for the MTEX software known as the Infimal Convolution filter, but is still not recommended to be used for research purposes, as it is currently in its trial phase.

3.4.3 Specimen and Crystal Direction

Initially, the symmetry of the EBSD indexed measurements need to be declared using a variable type, *crystalsymmetry*. The cubic crystal symmetry of the Ni-30Fe alloy can be designated by the crystallographic axes, $\vec{a}$, $\vec{b}$, $\vec{c}$ and its corresponding axes length of 3.56 Å. This crystal reference system consists of the inscribed specimen reference system with vectors, $\vec{x}$, $\vec{y}$, $\vec{z}$, such that $\vec{x}$ // $\vec{a}$, $\vec{y}$ // $\vec{b}$, and $\vec{z}$ // $\vec{c}$. The crystal direction is dependent on the alignment of these crystallographic axes and its corresponding coordinates (u, v,w), also known as Miller indices, such that it provides a vector for the crystal lattice direction. This vector can be written as: $\vec{m} = \vec{a}\cdot\mathrm{u} + \vec{b}\cdot\mathrm{v} + \vec{c}\cdot\mathrm{w}$

So, the crystal direction from this vector is denoted by [uvw] with its Miller indices as corresponding coordinates for the crystallographic axes. Additionally, the normal vector with respect to the lattice direction, provides the crystal plane (hkl), given by the vector: $\vec{n} = \vec{a}^*\cdot\mathrm{h} + \vec{b}^*\cdot\mathrm{k} + \vec{c}^*\cdot\mathrm{l}$, where $\vec{a}^*$, $\vec{b}^*$, $\vec{c}^*$ is the reciprocal of the crystal coordinates.

After the uniaxial compression test is conducted on the cylindrical specimen, the deformed sample is polished with respect to the plane parallel to the vertical cylinder axis. Additionally, the vertical cylindrical axis is also parallel to direction of compression applied as shown in Fig.3.5(a). Therefore, this polished plane which is parallel to both the compression direction and vertical cylinder axis is ideally a rectangular sectioned plane in 2D (as observed in the 2D EBSD scans). This rectangular shaped plane from the cylindrical specimen will observe a single compression direction and a single extension direction, which will be normal to each other (seen in Fig.3.5(b)). Therefore, the compression direction of the specimen from this rectangular section needs to be captured in the EBSD plot, and will be denoted as the Normal Direction(ND). Subsequently, the extension of the specimen occurring normal to the compression direction will be denoted as the extension direction(ED).

By contrast, the plane normal to the vertical cylindrical axis, would ideally be observed as a circular section for the 2D EBSD scan. This circular sectioned 2D plane of the cylindrical specimen will not be able to capture the compression direction and solely consist of the multiple extension directions, since it is perpendicular to the compression direction (seen in Fig.3.5(c)). Finally, the positioning of the specimen

under the microscope for the EBSD technique determines the actual specimen directions(ND and ED). The specimens before and after deformation have been rotated by 90°based on Fig.3.5(b) and subsequently observed during the EBSD technique. The other specimens for this project have obtained their corresponding EBSD scans with the similar positioning of ND and ED, as shown in Fig.3.5(b).

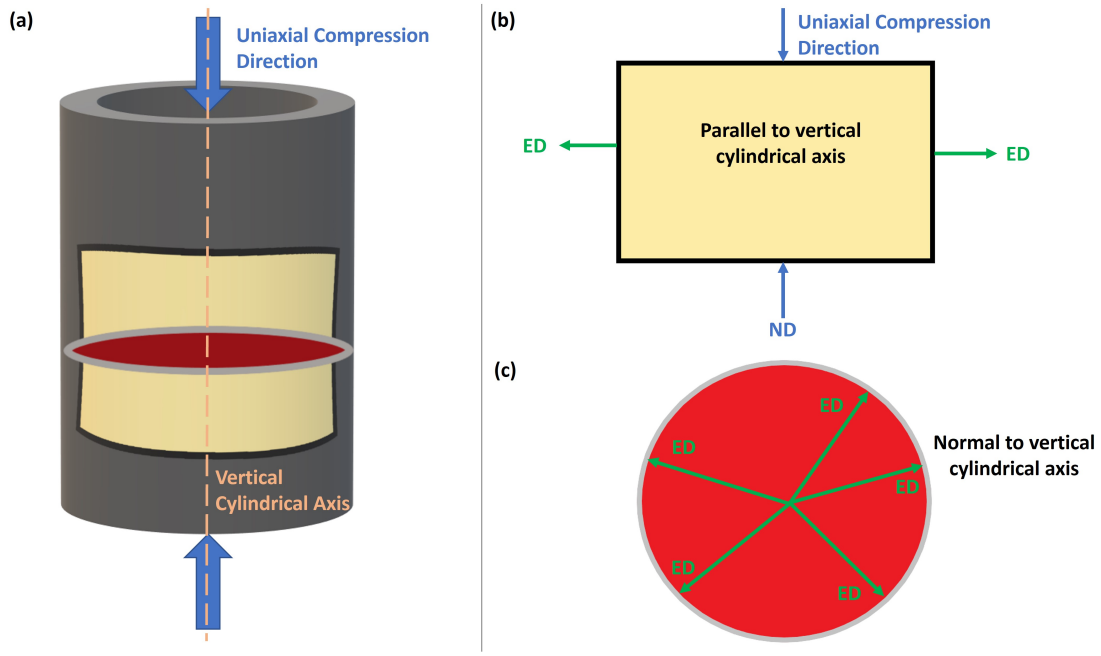

FIGURE 3.5: **(a)Schematic Representation of the cylindrical specimen; (b) Rectangular sectioned plane in 2D capturing ND and ED; (c) Circular sectioned plane in 2D capturing multiple ED's**

The specification of an orientation can be estimated by the crystal lattice directions that point towards the ND or ED, which is more commonly associated to an IPF. The 2D representation of orientations through an IPF is highly dependent on the crystal symmetry of the Ni-30 Fe alloy. The initial point of obtaining an IPF map is to define the specimen direction, which would be the ND or uniaxial compression direction. Thereafter the different crystal directions are computed for the ND, based on the orientations of the ND, which is finally plotted as a spherical projection. It is important to note that the ND is in the horizontal east direction (X direction) for the specimens before and after deformation. The following specimens at different annealing times: 1s, 2s, 5s, 10s, 20, 50s 100s, 200s, 500s and 1000s have their corresponding ND in the vertical north direction (Y direction).

The orientation of the crystal face within a grain, which is pointing outwards (towards the frontview) is the main concept for the IPF colouring map. The coloured crystal is initially in the shape of a ball. Thereafter, the colour present in the centre of this crystal ball is taken as the orientation that represents the corresponding grain. With the colours designated for each of the grains, the crystallographic axis pointing in the ND of the specimen can be determined, as shown in Fig.3.6. During deformation, it is expected that there are different colours present in different crystals of the grain, which provides the corresponding orientation gradients within the grain, as observed in Fig.3.4(a).

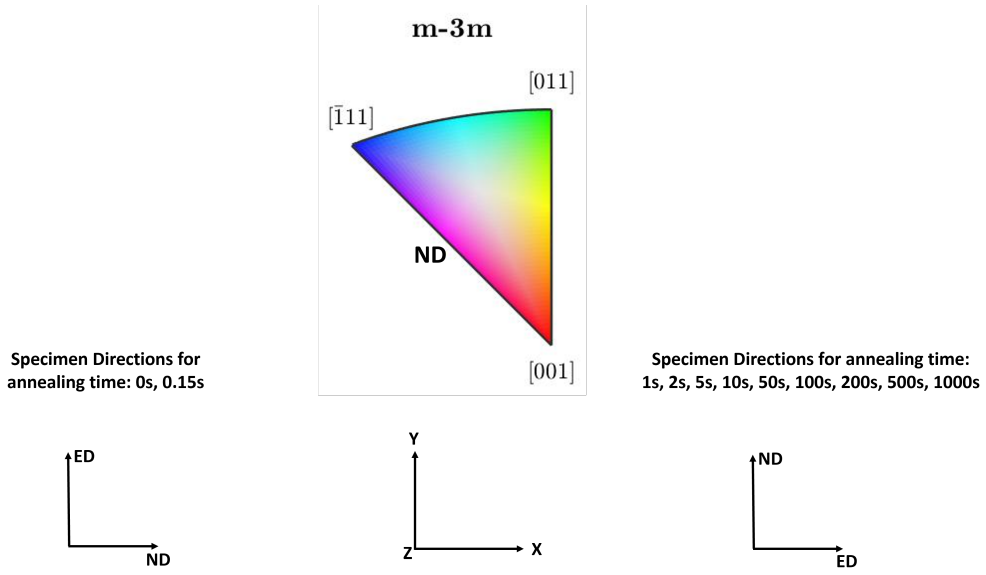

FIGURE 3.6: **IPF colour code along ND**

In conclusion to this section, we observe that MTEX provides us with many essential tools that can be used effectively to study the SRX phenomenon. This technical computing software provides us with the mathematical functions for optimization, filtering and analysis of the 2D EBSD scans. The high quality indexed regions provide us with the necessary orientation information to detect grains at a microstructural level. However, the compilation of large quantitative data in the from of matrices and arrays utilizes high computation time, which could reduce the efficiency of the EBSD analysis. Nevertheless, the flexibility and availability of different inscribed functions allows us to formulate, capture and develop the EBSD maps required for obtaining accuracy-driven results, based on the current research objectives.

Chapter 4

Results and Discussions

4.1 Overview

On the basis of the research objectives formulated in section 2.7, this chapter utilizes the described experimental techniques to report the SRX phenomenon that occurs during the annealing treatment. Initially, the former twin boundaries and the subsequently formed annealing twins are accounted in section 4.2 for the FCC structured Ni-30 Fe alloy. Thereafter, the separation technique in order to clearly distinguish the recrystallized and deformed grains has been analyzed using multiple approaches in section 4.3. Then, the selected separation technique is incorporated in section 4.4 to quantify the grains in the microstructure and study the grain size distribution during the annealing treatment. Additionally, the deformation measurements in section 4.5 have been carefully considered with the dislocation densities and stored energy within the Ni-30Fe alloy. Consequently, the effects of recovery and recrystallization have been utilised to describe the nucleation process in section 4.6. Finally, the recrystallization kinetics have been estimated experimentally and compared with the available models in section 4.7.

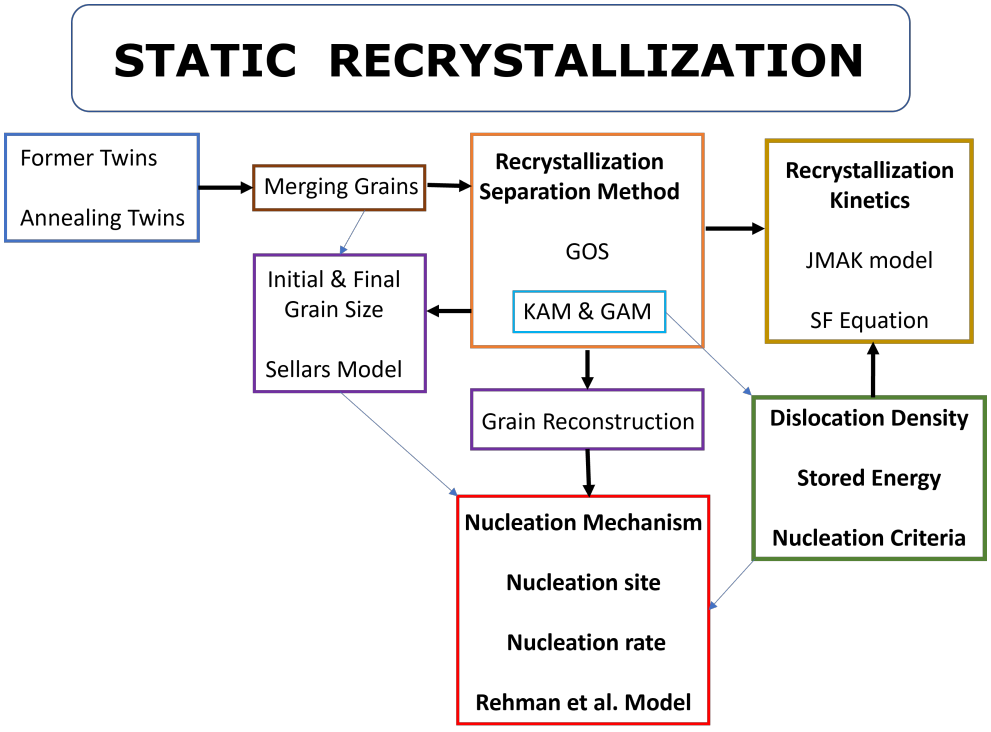

FIGURE 4.1: **Research overview flowchart for the practice-oriented research study**

4.2 Twin Boundaries and Annealing twins

The theory involving twins and CSL misorientations is an important concept to determine the relative orientation of two grains, with respect to each other. This section describes the grain boundary character observed for the alloy before and after deformation, followed by the annealing twins formed with time as a result of grain boundary migration. Finally, a function is defined for merging grains that involve common twin boundaries to avoid inaccuracies in grain size calculations.

The misorientation of grains is calculated by the standard modulo crystal symmetry, as an angle between both the orientations of the two grains. This angle of misorientation would be the lowest possible angle from the list of symmetrically equivalent orientation pairs. Besides the misorientation, the interfacial plane is known to contribute to the two different types, namely coherent and incoherent twin boundaries. The former type of twin is known to exist in the {111} plane behaving as a mirror between two adjacent crystal lattices, whereas the latter type of twin is known to exist in another plane. However, for the purpose of this project, the twins are not particularly distinguished with this criteria, since this difference is only vital when interfacial properties such as mobility is taken into consideration.

The coherent and incoherent twin boundaries are generally defined as the same misorientation angle between two crystal lattices, which is 60°<111>, with one-third of the atomic positions being common with each other, corresponding to $\Sigma = 3$ CSL. Additionally, second order twin formation is possible by multiple twinning and intersection of $\Sigma 3$ twins, leading to the formation of $\Sigma 9$ boundaries. The common misorientation observed for $\Sigma 9$ boundaries is 38°<101>, which is also categorized as one of the special boundaries.

4.2.1 Grain Boundary Character: Before and After Deformation

The CSL boundaries are defined by the misorientation and their coincident lattice planes. The grains that are present before deformation are known to produce different CSL boundaries to reduce the grain boundary energy. From the analysis of the CSL boundaries, it is observed that the Ni-30Fe alloy pre-dominantly contains a large fraction of $\Sigma 3$ boundaries, due to the close packed planes in the austenite phase and intermediate SFE of the material [12]. Beyond the grain boundary energy, these former twins are known to be defects that can positively impact the microstructure after deformation, by participating in the recrystallization mechanisms, since multiple twinning can lead to the required instability and higher mobility of twin boundaries [12]. This has been further analyzed in section 4.6.1.

On conducting the uniaxial compression test, it is observed that there are changes occurring in the grain boundary character due to rotation of the crystals within the grain. This leads to randomized misorientations(grain boundaries categorized as Random HAB) that do not have the necessary misorientation for the defined former twin boundaries, as seen in Fig.4.3. Additionally, in terms of quantification, Fig.4.2 indicates that there is a decrease in former twin boundary density for the $\Sigma 3$ twins, from 48.83% to 10.04% after deformation ($\epsilon = 0.2$) at 900°C. The similar phenomenon is observed for the second order twins, where $\Sigma 9$ twins is negligible after deformation. The other specific Σ boundaries, where Σ = 5,7,11 do not have any influence

on the Ni-30 Fe alloy microstructure, as seen from the quantitative calculations, and hence can be neglected for the experimental analysis.

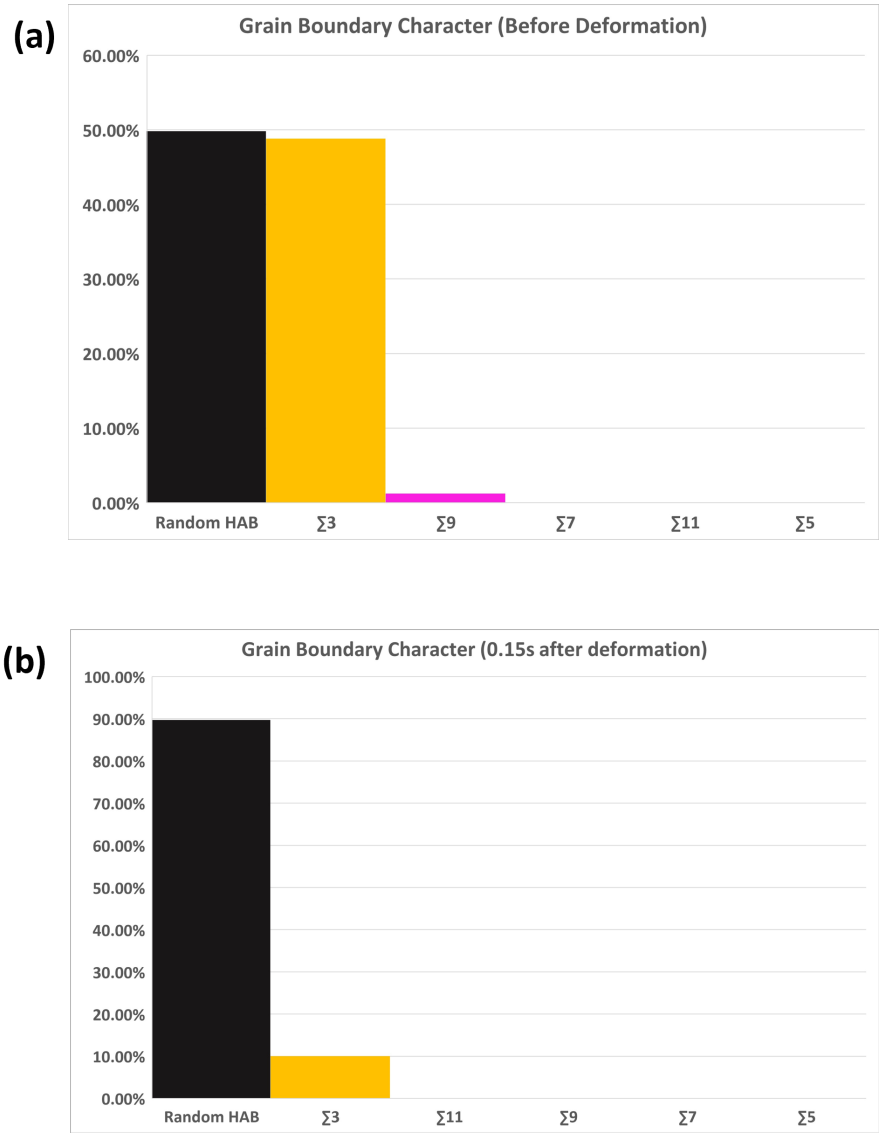

FIGURE 4.2: **(a) CSL boundaries before deformation; (b) CSL boundaries after deformation**

For this analysis, a tolerance has been incorporated into the twin detection procedure since the accuracy of the EBSD technique for orientation measurements accounts for half a degree deviation. This tolerance equation is borrowed from Brandon et al, shown in Eq.4.1 [43], where θ_m is the minimum orientation threshold for HAGBs, which is estimated to be 15°from the literature [55]. The other parameter, Σ, is related to the degree of coincidence for the lattice defined above. So, the tolerance for detection, ω, is calculated from Eq.4.1 to be 8.66°for the Σ3 twin boundaries.

$$\omega = \theta_m \cdot \Sigma^{(-1/2)} \tag{4.1}$$

There is a noticeable decrease from the predominant misorientation angle(60 °) for the grain boundaries due to induced deformation, as seen from the histogram in Fig.4.3. These quantified results are similar to the previous work done for the alloy

[12]. The presence of coherent twin boundaries in the microstructure is known to possess the lowest energy configuration, whereas incoherent twin boundaries are expected to possess higher energy, as they do not lie in the predominant {111} plane. Therefore, the former twin boundaries present after deformation(within the tolerance value) are expected to mainly possess coherent configuration of twins, which are stable and immobile. The former twin boundaries still present during the annealing treatment dissociates only after consumption of the deformed grains, i.e. during the recrystallization and grain growth processes. Thereby, the loss in the grain boundary character for the Σ3 twins, illustrated in Fig.4.3, correlates to the increase in stored energy within the material, since a large density of GNDs can be accommodated in these boundaries after deformation. This can be experimentally validated using the recrystallization nucleation mechanism and sites described in subsection 4.6.1.

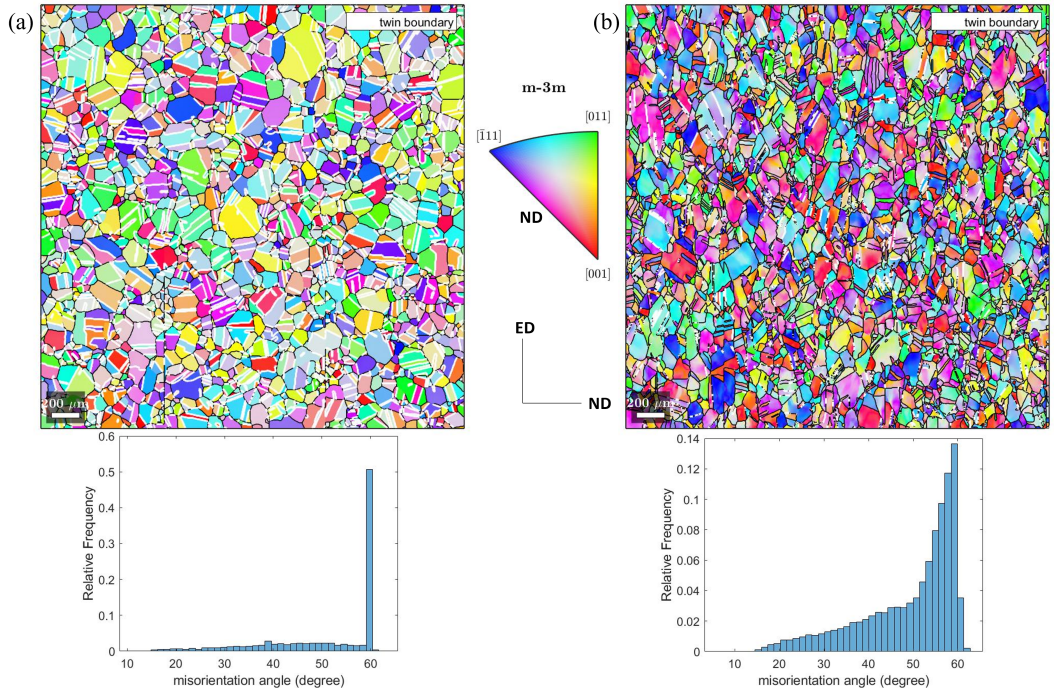

FIGURE 4.3: **(a & b) Respective EBSD IPF map before and after deformation, and their corresponding relative frequency for the grain boundary misorientation angle**

4.2.2 Annealing Twins during different time intervals

The former twin boundaries present prior to deformation as observed in Fig.4.3(a), are known to occur by Shockley partials at the {111} plane of the grain boundaries. However, once the deformation conditions are applied, we observe from Fig.4.5(a) that these former twins can expand in area, by migration of the recrystallization front, validating the proposed twinning mechanism by Mahajan et al.[56]. The expansion of these former twin boundaries at 1s annealing time could be due to the increase in stored energy from the external stress field, which leads to gliding of the partial dislocations. Therefore, these former twin boundaries could behave as regions of high stored energy, which would permit the driving force required for their expansion. This is discussed further in subsection 4.6.1.

Thereafter, it is observed from Fig.4.4 and Fig.4.5(b), that the overall twin density for the scanned region begins to increase gradually upto 10s time interval. This increase in twin density is due to the process of recovery and recrystallization, where the stored energy from deformation is known to gradually decrease, forming new grains. These newly formed grain boundaries need to compensate based on the requirements of the recovery process, which can be done by developing twin boundaries (also referred to as annealing twins), since it reduces the interfacial energies and improves ductility properties [12].

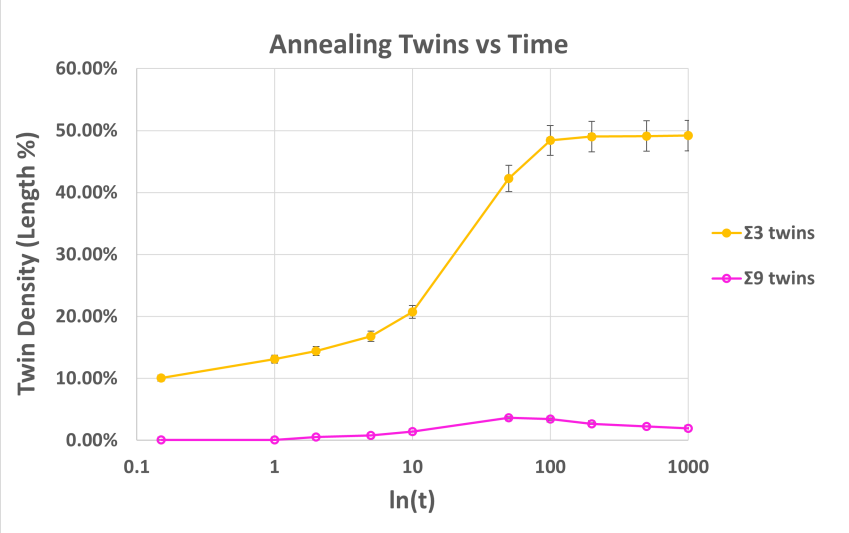

FIGURE 4.4: **Annealing Twin formation during recovery, recrystallization and grain growth**

The dominant increase in annealing twin density is observed after 10s annealing time, once the recovery process is complete and the recrystallized grains begin to grow consuming the deformed grain boundary and former twin boundaries. At 50s annealing time it can be observed quantitatively that there is a maximum density of second order twin(Σ9) relation formed, with a twin density percentage of 3.63%. However, after 50s annealing time, we can quantitatively observe that the Σ9 twin density gradually decreases at 100s, and continues to decrease during the grain growth process(until the end of the annealing treatment). Subsequently, the Σ3 twins increases from the 50s annealing time until the end of the recrystallization and grain growth processes. Therefore, on consideration of an extremely small error for the Σ9 twins, this decreasing phenomenon after 50s annealing time allows: the reduction in total grain boundary length, and the transformational merging of Σ9 to Σ3 twins, thereby reducing the interfacial energy. As a result, the annealing twins present after recrystallization and grain growth will predominantly be coherent Σ3 twins which are stable, immobile and possess low interfacial energies.For the topological 2D observation of this quantitative decrease in Σ9 twins, two subsequent EBSD measurements must be conducted after the recrystallization process(E.g. 100s and 102s annealing time).

Fig.4.5(c) & (d) compares the annealing twin density present during recrystallization(50s annealing time) and grain growth(500s annealing time). The annealing twin density is slightly lower during recrystallization, approximately 42.26% twin density, as compared to the twin density after grain growth with approximately

49.11% twin density. Besides the transformational merging of Σ9 to Σ3 twins, the slight increase in Σ3 twins can be accounted by the difference in recrystallized grain size between the recrystallization and grain growth process. So, the twin density slightly increases as the grain develops and grows during the grain growth process, improving interfacial stability within the microstructure. Additionally, the significantly lesser annealing twins generated after the 100s annealing treatment is expected, since the grain boundary velocity is predicted to be lower towards the end, rather than during the recrystallization process. During grain growth the annealing twins become coherent in nature, which can be observed by straight line traces through the grain (as seen in Fig.4.5(d)). For future research it is essential to carefully categorize annealing twins seperately as recrystallization twins and grain growth twins, as it would accurately depict the different stages of the SRX phenomenon.

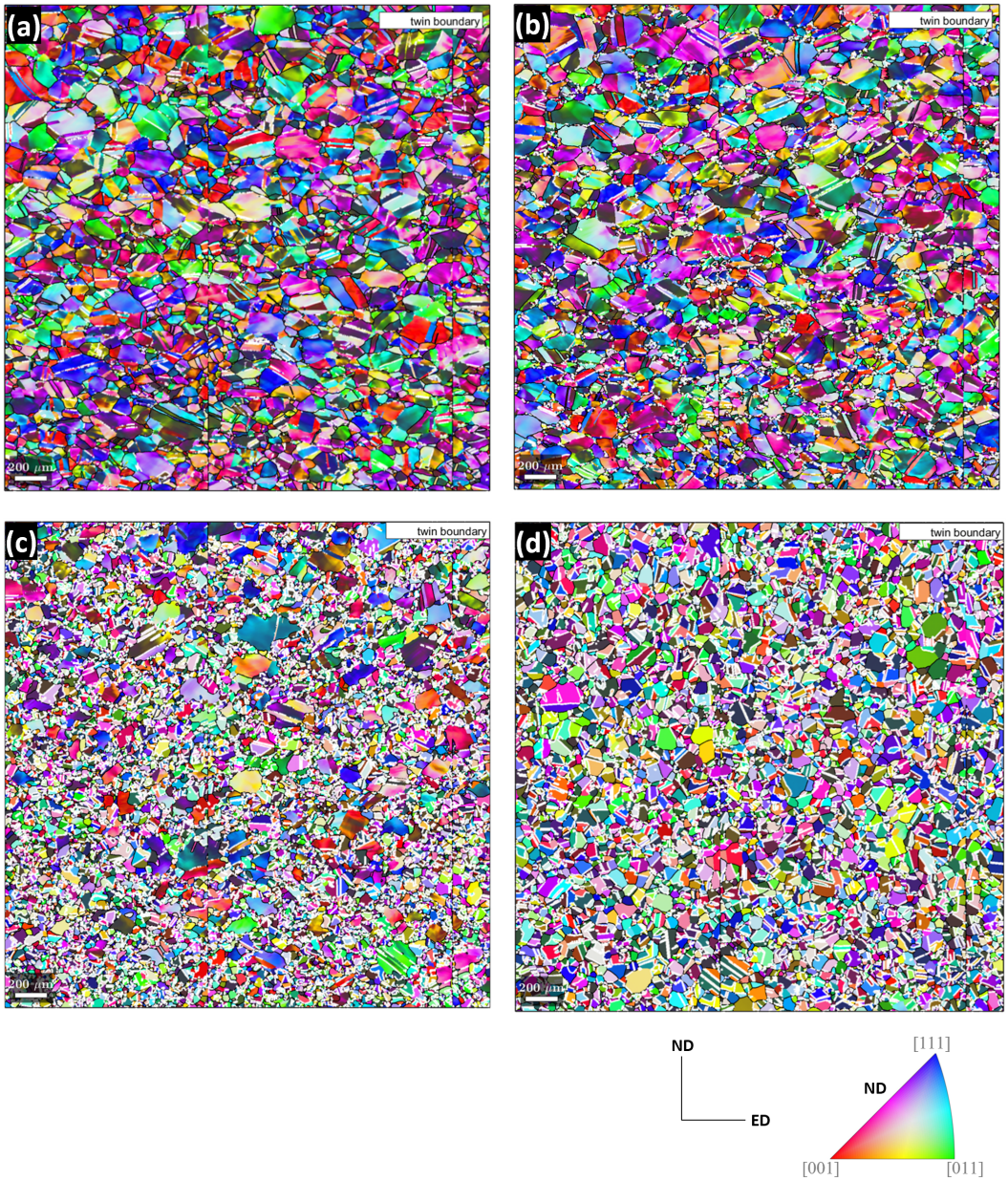

FIGURE 4.5: **EBSD IPF map for different annealing time: (a)1s, (b)10s, (c)50s, (d)500s. Twin boundaries represented in white colour**

4.2.3 Merging Grains

The grain boundaries categorized as HAGB, by detection of the minimum orientation threshold(θ_m) between pixels is stored in a variable, known as gB. Then, the $\Sigma 3$ twin boundaries defined above are detected by the MTEX software and saved in the variable *twinboundary*, which is coloured differently to the HAGBs for identification purposes. As observed in subsections 4.2.1 and 4.2.2, almost half the fraction of the total grain boundary length consists of $\Sigma 3$ twin orientation relation for the alloy. The presence of these twins must be carefully considered/avoided for statistical calculations, since each parent grain consists of inconsistent number of twins. MTEX is provided with a function known as *merge* which is useful in conducting grain size calculations, using the information of only the parent grain structures without twinning. Essentially, this function merges grains that belongs to a common twin boundary, which is consequently used in the next section to separate the recrystallized and deformed grains using different orientation gradient measurement methods. The merging method incorporated in this research study, as will be seen in the following sections has to be used appropriately, since it is not absolutely accurate, producing minimal statistical errors of approximately 2-7% for the recrystallization kinetics during the recovery and recrystallization process(observed in more detail in subsection 4.3.4.

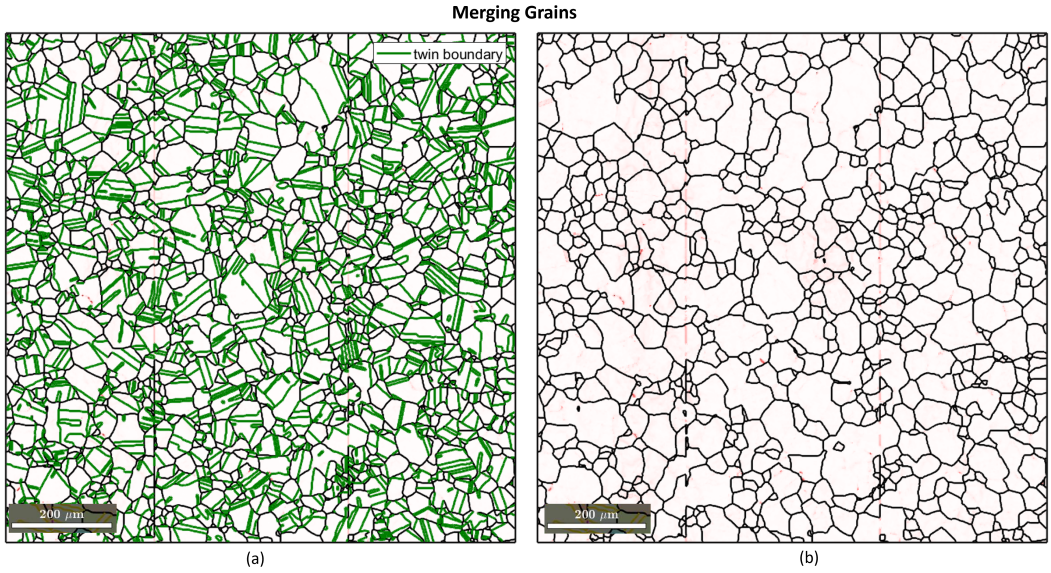

FIGURE 4.6: **Merging grains with common twin boundaries, where, (a) Before Merging and; (b) After Merging. The EBSD maps here include the data for before deformation specimen**

4.3 Recrystallization Separation Method

The separation technique of the deformed grains from the newly formed grains is essential for the recrystallization kinetics and nucleation rate estimation. This section describes the initial method developed to articulately separate grains during SRX, using the Grain Oriented Spread (GOS) method in subsection 4.3.1. The section goes on to describe another approach for separation using the combination of Kernal Average Misorientation (KAM) and Grain Average Misorientation (GAM) in subsection 4.3.2. Finally, both the techniques are compared and evaluated to finalize

the most accurate separation technique in subsections 4.3.3 & 4.3.4.

The Ni-30Fe alloy used in this research for the study of SRX is observed to obtain recrystallized nuclei at a very early stage in the annealing treatment. The deformation conditions for the alloy, at $\epsilon = 0.2$, and an annealing temperature 900°C, using the calculations from the literature is supposedly sufficient to avoid dynamic recrystallization of grains. It is however possible for nucleation to occur during deformation, even at such low strain conditions due to presence of initial sub-grains in the alloy [57]. Nevertheless, the nuclei initially formed during the deformation are known to be unstable and disappear with subsequent annealing time [57]. Hence, development of such nuclei during deformation is considered insignificant and irrelevant for this research study, since the definition of SRX phenomenon requires recrystallization nucleation to transpire only after deformation of the specimen. The EBSD scans used to estimate the recrystallization fractions are based on the different annealed samples at: 1s, 2s, 5s, 10s, 50s, 100s, 200s, 500s and 1000s annealing time.

4.3.1 Grain Oriented Spread (GOS)

The distribution of orientation measurements from the EBSD scan is an important concept used for determining the recrystallization separation technique.

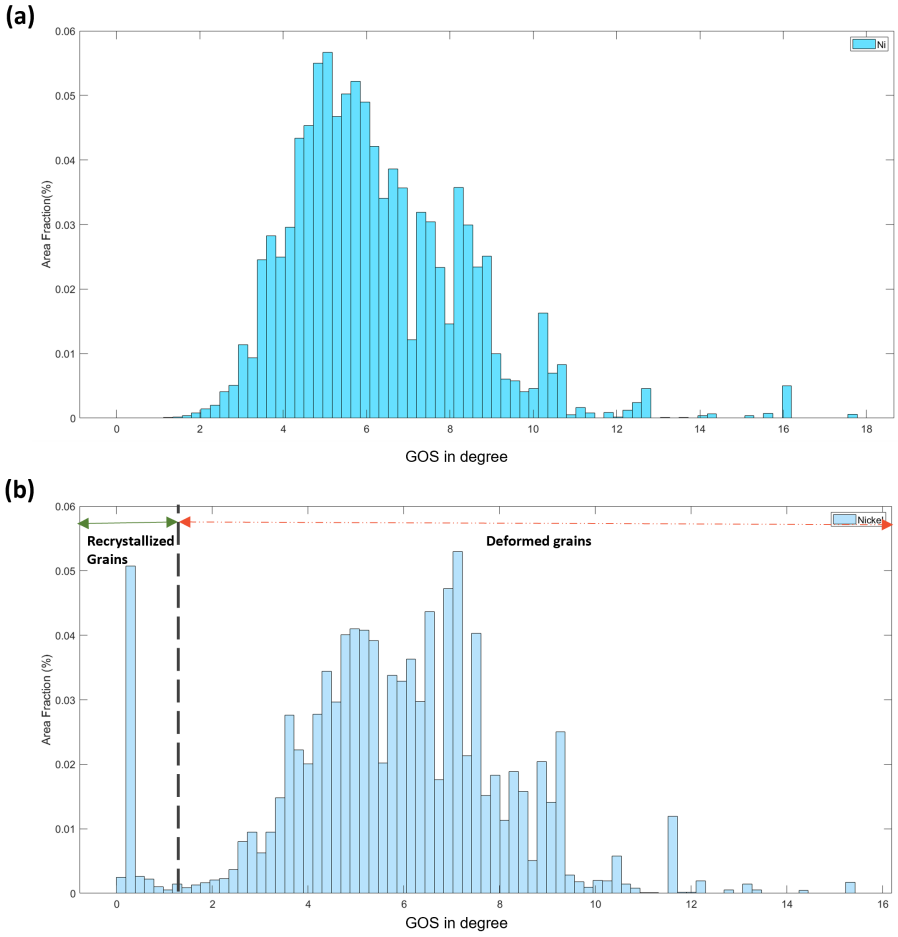

FIGURE 4.7: **(a) GOS measurements after deformation; (b) GOS measurements after 10s annealing time**

The distribution of GOS in degree for the relative area fraction(%) after deformation and subsequently after 10s annealing time can be observed in Fig.4.7(a) and (b), respectively. Initially, the specimen has a randomized distribution of GOS values, due to the deformation induced. However, due to the effects of recovery, we observe that recrystallization nucleated grains have a lower GOS value. The histogram generated from the 10s annealed sample is an example of finding the separation point between the recrystallized and deformed grains, by observing a cut-off point. The cut-off value found from these results are 1.25°, where grains that have GOS values lower than this value are considered recrystallized, whereas grains larger than this value are considered deformed. The determination of the cut-off GOS value is conducted by using error bars at the upper and lower limits of 1°and 1.5°, respectively. Additionally, another method of accurately selecting the cut-off GOS value and further reducing the error is by increasing the number of bins, so that the number of data points in each bin is reduced.

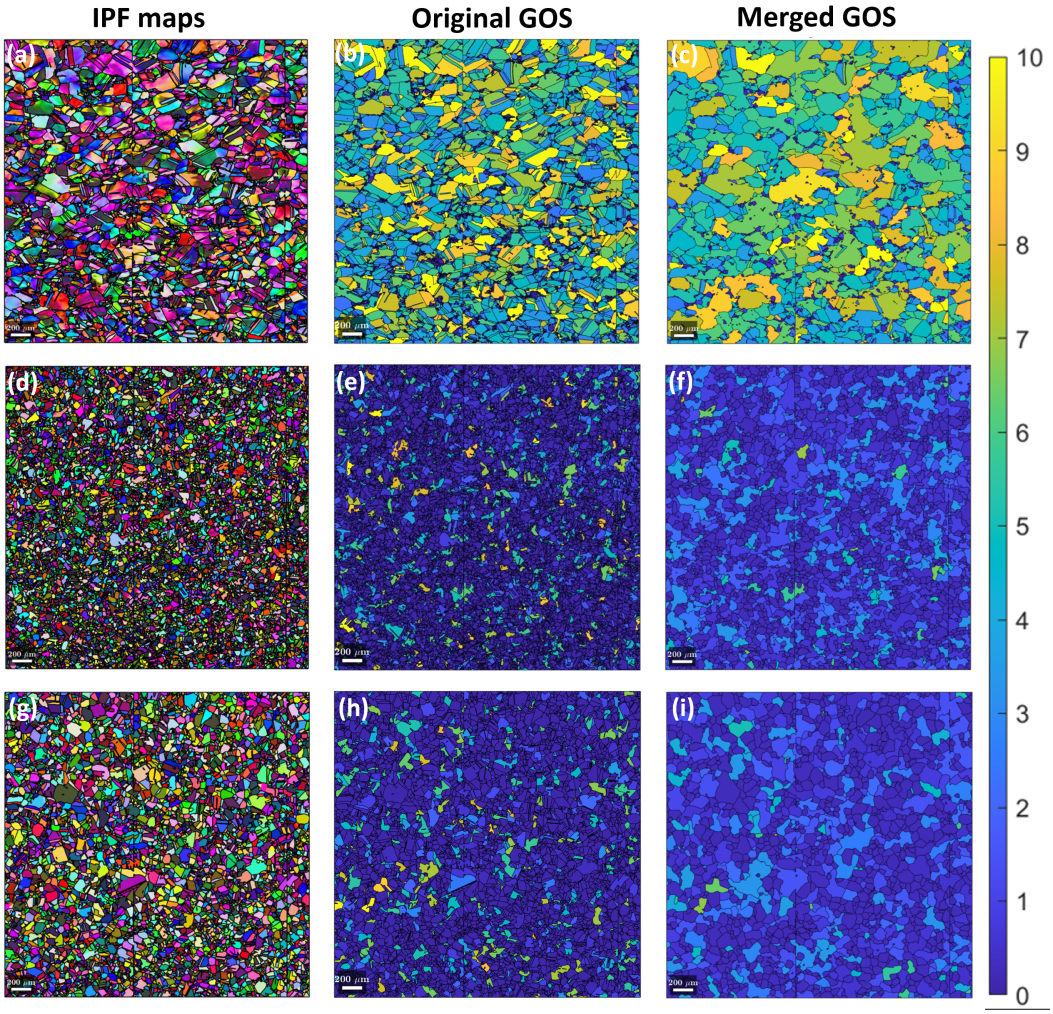

FIGURE 4.8: **(a), (b) and (c) 10s annealing time; (d), (e) and (f) 100s annealing time; (g), (h) and (i) 1000s annealing time. The first(left) column shows the EBSD IPF maps, the middle column shows the original GOS maps, and the last column shows the merged GOS maps for the mentioned annealing periods. The scale indicates GOS in degree. The IPF colour coding is the same as Fig.4.5.**

The GOS is calculated for the grains in the scanned region for different annealing times(as shown in Fig.4.8(b), (e) and (h) for 10s, 100s and 1000s, respectively). Subsequently, the merged GOS can be incorporated(using subsection 4.2.3) into this separation technique, so as to consider the presence of twin boundaries that causes slight deviations to the original GOS values. These discrepancies between the original GOS and merged GOS can be seen from the middle and last column of Fig.4.8, where original GOS has slightly higher values for the respective grain regions. The decrease in GOS values for the merged GOS maps is because the grain mean orientations are altered after the grains are merged, providing lower misorientation (deviation) angles between the orientation pixels in the merged grain and the merged grain mean orientation. The merged GOS cut-off value observed experimentally for the EBSD scans is 1.2°. However, these discrepancies for the original GOS and merged GOS is observed to be extremely minute for the recrystallized grains and the recrystallization kinetics. Therefore, we adhere to the mergedGOS maps to determine the recrystallization fraction (using the histograms as shown in Fig.4.7) at different time intervals of the annealing treatment.

The merged GOS maps in Fig.4.8(f) and (i), experimentally show the merged grain GOS values for 100s and 1000s annealed specimens, respectively. From these two maps, we observe that the mergedGOS after the recrystallization process is not accurate for the separation technique. The GOS colured merged grains in the map, for the 1000s annealed treatment specimen have almost the similar fraction of unrecrystallized grains as that of the 100s annealed specimen. So, the grain growth process depiction, where the unrecrystallized grains become fully consumed by the growth of the recrystallized grains cannot be verified from the merged GOS technique. This is because the average of the misorientation angles from the merged grain mean orientation, is still comparatively high due to the presence of different crystallographic orientations for a particular region within the grain, rather than orientation gradients which define an unrecrystallized grain. Such grains in the 1000s annealed sample may not be separated by a random HAGB, since they may have misorientations smaller than 15 degrees(LAGB) or have annealing twins within the grains. Moreover, it can be observed from the IPF maps in Fig.4.8(d) that the 100s annealed specimen has orientation gradients within few grains which translates accurately in the merged GOS map, whereas the 1000s annealed specimen in Fig.4.8(g) does not have such orientation gradients within grains, to be considered as unrecrystallized grains. Therefore, a different approach has been used in the next section for the separation technique.

4.3.2 Kernal Average Misorientation (KAM) and Grain Average Misorientation (GAM)

Following the literature research from section 2.3, we can define KAM as the intragranular average misorientation angle per orientation pixel that is dependent on many factors such as: the nearest number of neighbours (n=2), number of pixels within the kernel, the threshold angle ($\Delta\theta$ = 2.5°), the scanned area of the sample (9mm^2) and its corresponding step size (5μm). Using Eq.2.1 and the methodology described in section 3.4.1, the KAM values of the low resolution EBSD scans are plotted in Fig.4.9(a),(d) & (g), with a scale ranging from 0-2 for each pixel in the micro-graph. The cut-off for the GAM value (shown in Appendix section A.1) is estimated using the similar technique for the cut-off GOS value. The resulting cut-off

GAM value to determine the recrystallized grains and recrystallization kinetics is 0.25°(using error bars for the upper and lower limits of 0.2°and 0.3°, respectively).

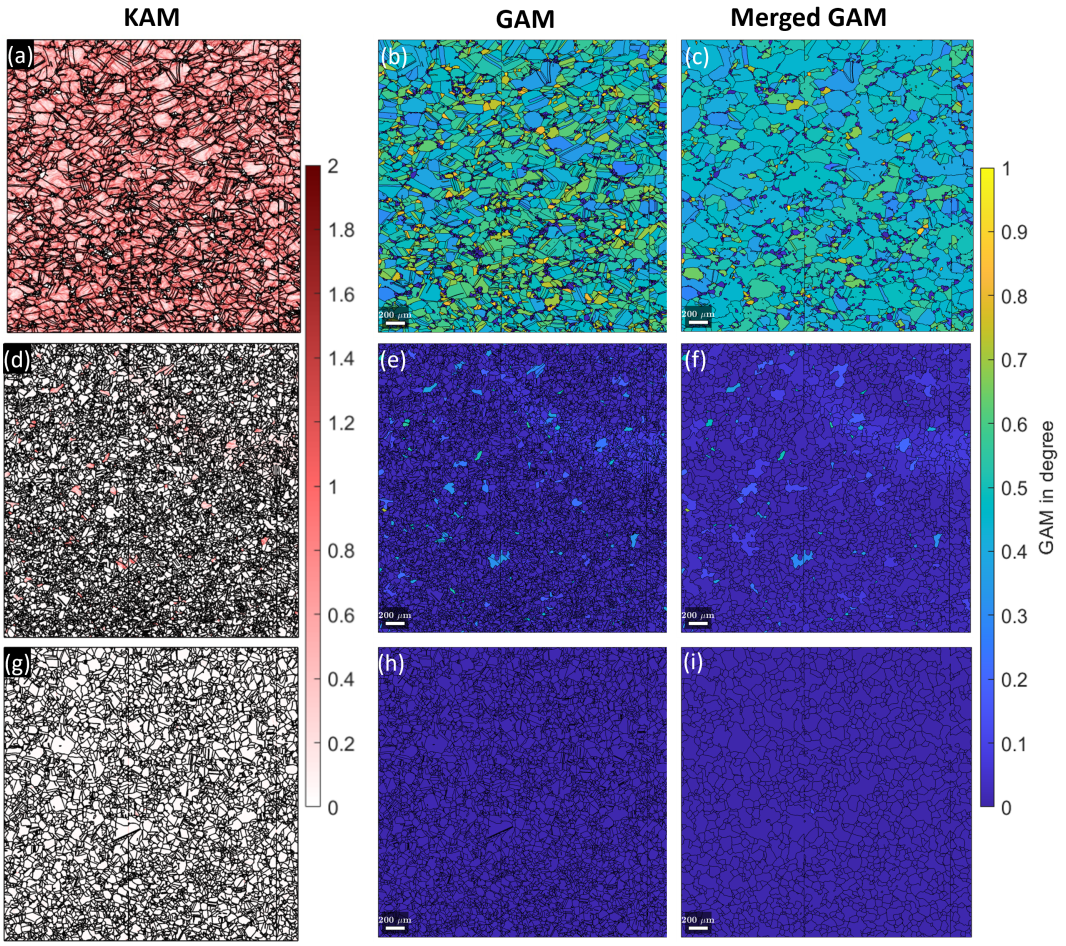

FIGURE 4.9: **(a), (b) and (c) 10s annealing time; (d), (e) and (f) 100s annealing time; (g), (h) and (i) 1000s annealing time. The first(left) column shows the KAM maps, the middle column shows the GAM maps, and the last column shows the merged GAM maps for the mentioned annealing periods.**

The GAM maps and merged GAM maps have been plotted in Fig.4.9(b), (e) & (h) and Fig.4.9(c), (f) & (i), respectively for the different annealing time intervals, using the cut-off GAM value. The merging method used for GAM is similar to previous procedure used for GOS, and it is observed that there are small discrepancies between the GAM and merged GAM, which will be further analyzed in subsection 4.3.4. The merged GAM cut-off value used in the experimental analysis of the EBSD scans is 0.25, similar to the GAM cut-off value calculated.

Furthermore, we can state that the overall merged GAM values are drastically smaller than merged GOS values, which is a first indication that the merged GAM technique could be more accurate in terms of determining the average misorientation angles within a grain. The comparison between merged GOS and merged GAM, so as to determine the more appropriate recrystallization separation technique (especially after the 100s annealing time interval) is reported in the following subsection.

4.3.3 Merged GOS and Merged GAM: Comparative Analysis

Following the GOS and GAM results from subsection 4.3.1 and 4.3.2, we observe several discrepancies in the recrystallization fractions obtained for the respective EBSD scans at different annealing periods. The recrystallization kinetics estimation using the two techniques is shown in Fig.4.10.

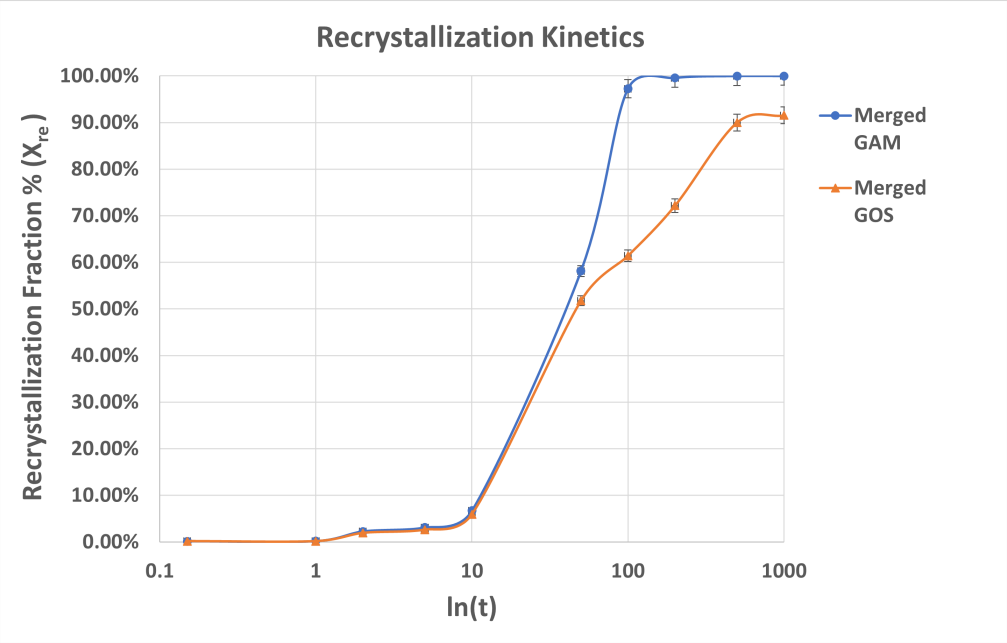

FIGURE 4.10: **Recrystallization kinetics comparison for merged GOS and merged GAM**

With the calculations of the recrystallization fractions, we can infer that the GOS and GAM seperation techniques follow a similar trend during the initial period of the annealing treatment when the alloy experiences the recovery and recrystallization nucleation process. However, once the SRX phenomenon transitions to the grain growth process (from 100s annealed sample), there is a large deviation in the recrystallized fractions. Additionally, the recrystallization fractions from the merged GAM separation technique follows the customary sigmoidal pattern of the JMAK recrystallization kinetics model, whereas the curve obtained with the merged GOS is more atypical in nature with much slower recrystallization kinetics. The comparison of the final experimental results with the JMAK model is conducted in subsection 4.7.3. Furthermore, as observed in Fig.4.8(i) for the 1000s annealed specimen, there is still a significant area of unrecrystallized fraction, approximately 8.5%, which should not be the case, since literature suggests[11] that the alloy would be completely recrystallized by the end of the annealing treatment.

To analyze these issues more closely, the experimental results of the 200s annealed sample is shown in Fig4.11. The recrystallized fraction of the 200s sample from Fig.4.10 for the merged GOS and merged GAM techniques are 72.15% and 99.55%, respectively (using the respective cut-off values mentioned in the previous two subsections). This large discrepancy between the two techniques is also distinctly visible between the micro-graphs in Fig.4.11. The IPF map for the respective annealed sample, indicates only a few grains that still comprise of orientation gradients within

them, whereas large proportion of the grains(99.55% area fraction) do not comprise of randomized orientations, and can be classified as recrystallized grains.

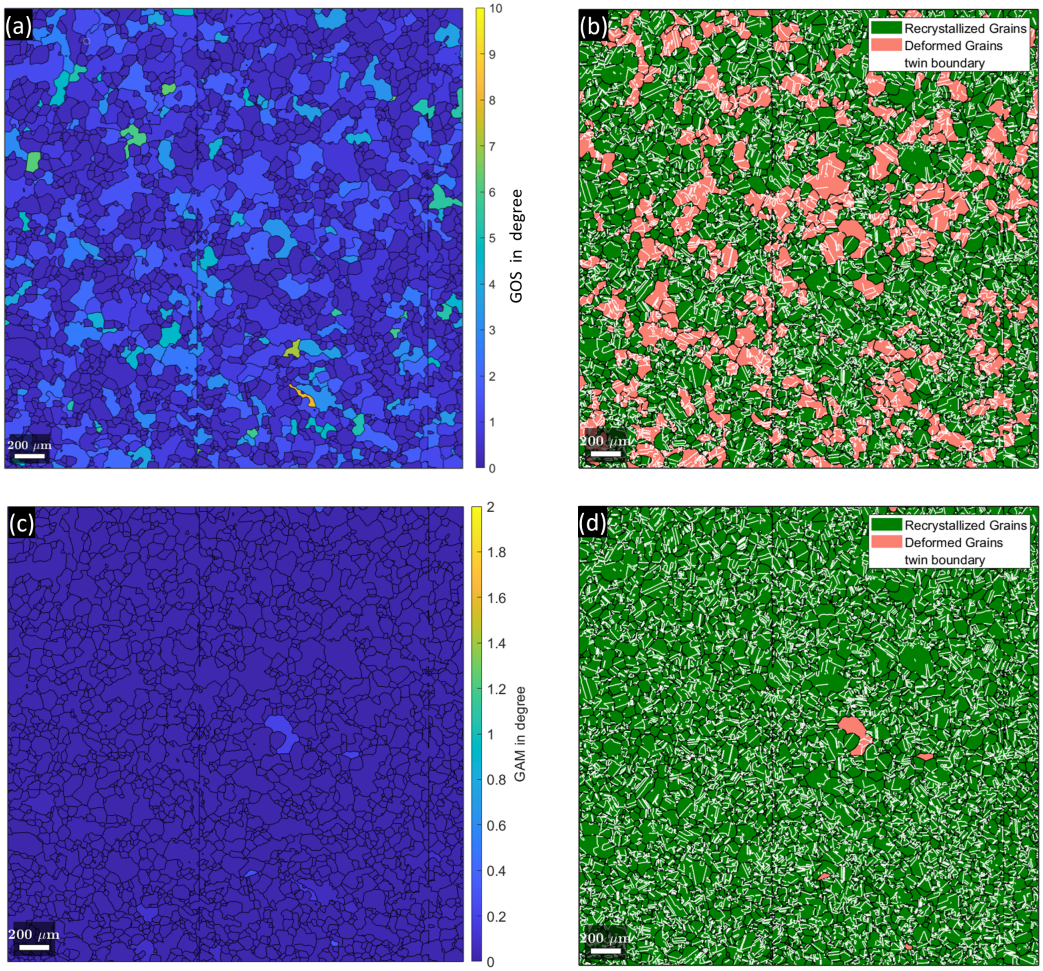

FIGURE 4.11: **Recrystallization Separation method for 200s annealed sample: (a) & (c) merged GOS and merged GAM maps, respectively. (b) & (d) Micro-graphical representation of recrystallized and deformed grains using merged GOS and merged GAM, respectively**

Separating recrystallized grains more accurately with the merged GOS technique is not achieveable, since there are recrystallized grains that comprise LAGBs and annealing twins within a grain that can separate different regions of the grain toward a particular set of orientations. Therefore, when the average of the misorientation angles are calculated with respect to the merged grain mean orientation, there appears to be comparatively larger deviations(misorientation angles) within the grain. This complication causes the recrystallized grains to be misinterpreted as deformed grains. By contrast, the merged GAM technique is more accurate in this regard, since the average misorientation angles is calculated with respect to its second nearest neighbouring pixels within a grain. This allows the recrystallized grains to be classified correctly, despite the presence of different sets of orientations within the recrystallized grains that form LAGBs and annealing twin orientation relations. Therefore, the separation technique selected for this experimental research study is the merged GAM technique. However, it is observed that even the merged GAM

technique is not absolutely accurate and is compromised on certain instances, which will be observed in the following subsection by comparison with the original GAM technique.

4.3.4 GAM and merged GAM: Comparative Analysis

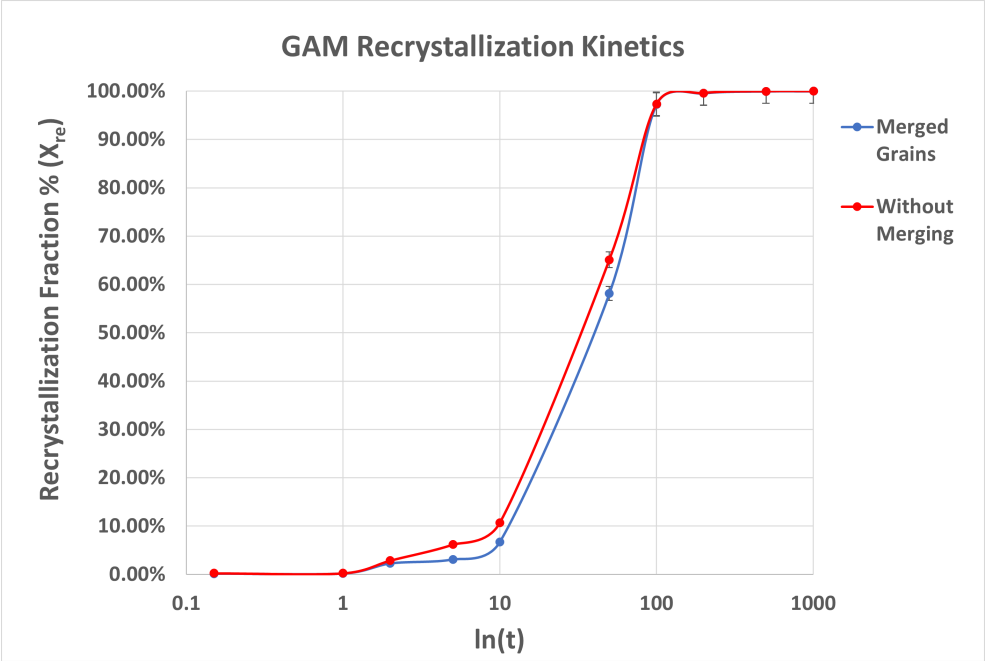

FIGURE 4.12: **Recrystallization kinetics comparing GAM and merged GAM techniques**

The recrystallization kinetics of the merged GAM is compared with the original GAM, shown in Fig.4.12. Unlike the previous comparison in subsection 4.3.3, here, the GAM and merged GAM do not observe a similar trend of recrystallization kinetics during the initial period of the annealing treatment, where recovery and recrystallization nucleation occur. However, the discrepancy intensity is not as large as the previous case, and both the curves with these separation techniques follow the predicted sigmoidal pattern of the JMAK model. Nevertheless, this discrepancy has to be analyzed, which is done with the experimental results of the 50s annealed specimen, shown in Fig.4.13.

From Fig.4.13(a) & (b), the process of merging can be observed where, grains that have a common twin boundary are merged together. However, on application of this method, we observe that the deformation gradients within the grains is altered. Additionally, it is seen from section 4.2 that a large proportion of the recrystallized grain boundaries contain annealing twins, as a result of the twinning phenomenon in the alloy. The presence of these annealing twins alongside a deformed grain boundary can be a potential drawback, since the merging function neglects a common twin boundary, connecting both a recrystallized and deformed region into a single grain. The possibility of this occurrence can be observed by the recrystallization kinetics deviation during the initial stage in Fig.4.12 between GAM and merged GAM. This drawback can also be observed experimentally from the highlighted yellow boxes in Fig.4.13.

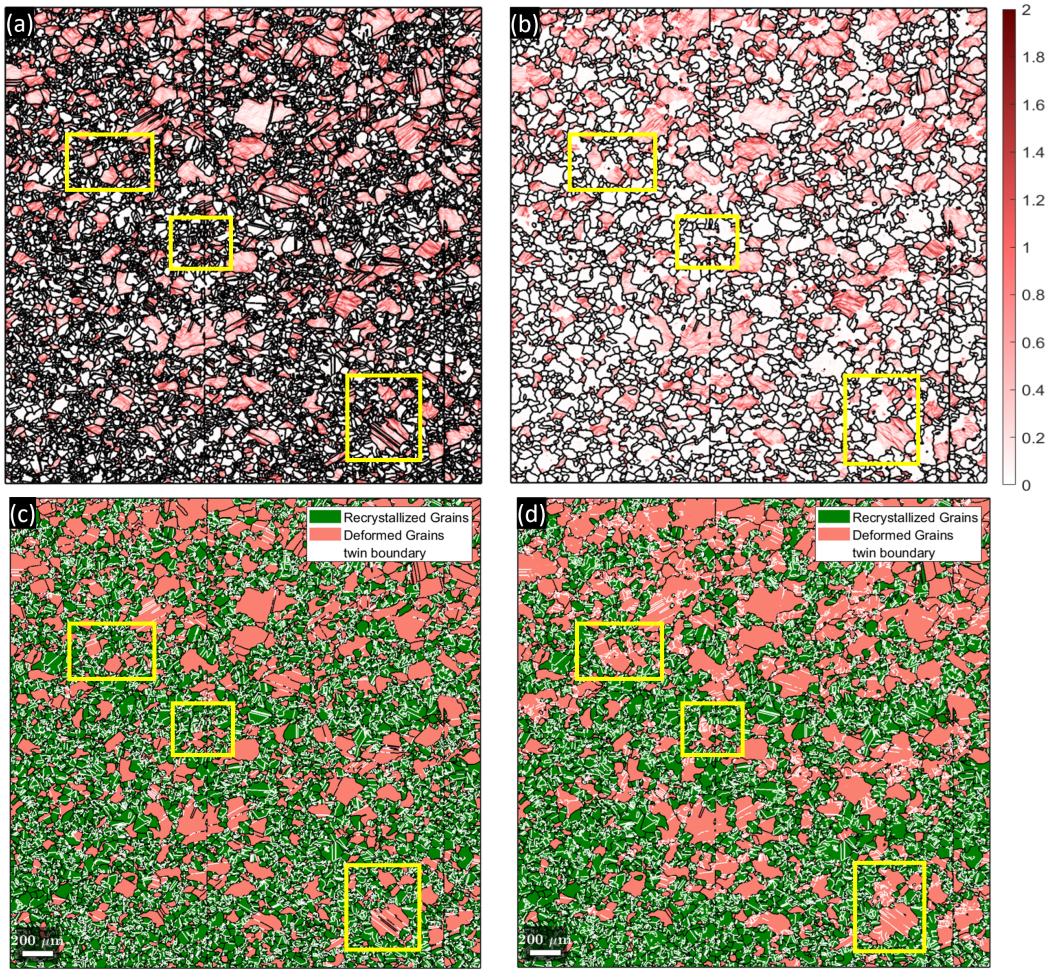

FIGURE 4.13: **Recrystallization Separation method for 50s annealed sample: (a)&(b) KAM and merged KAM maps, respectively. (c)& (d) Micro-graphical representation of recrystallized and deformed grains using GAM and merged GAM, respectively**

By merging the grains, few newly recrystallized nuclei become part of the deformed grains, depending on the position of the annealing twins. Therefore, the merged KAM and merged GAM values change accordingly for some recrystallized regions(as shown in the highlighted yellow boxes), constraining them to be included with the deformed grains. Since the deformed region is still prominent during the recovery stage, these merged regions have a greater area fraction of deformation than recrystallization, causing such grains to be on the right-hand side of the cut-off merged GAM value. Eventually, this leads to the recrystallization fractions of the merged GAM to be lower than the original GAM(without merging) during the recovery and recrystallization process of the annealing treatment, as seen from the recrystallization kinetics in Fig.4.12. Finally, once the recrystallization process is completed(after 100s of the annealing treatment), the grain growth kinetics is similar irrespective of using the merging process, since the deformed region is consumed by this point in the annealing treatment.

In conclusion to this section, the inaccuracies and atypical results obtained with the GOS separation technique, especially during the grain growth kinetics, slowing down the recrystallization kinetics process, allows us to categorize it as a flawed

technique for our research study. The GAM and merged GAM are observed to be the most prominent recrystallization separation methods. Additionally, even though the experimental observation of the original GAM(without merging) is more accurate for the recrystallization kinetics, the merging function is useful for other purposes. Therefore, as mentioned earlier, the merging function must be used with careful consideration since it can be vital for grain size calculations(seen in the following section), but is not recommended for the recrystallization kinetics estimation as experimentally validated in this section.

4.4 Grain Size Distribution

The literature research for grain size distribution in 2.6.2, shows the importance of the SRX phenomenon in order to attain refinement of grains by the end of the annealing treatment. The refinement of grains is essential to improve the desired mechanical properties of the alloy. This section reports the quantified values of recrystallized and deformed grains per mm^2 in subsection 4.4.1. Thereafter, the average grain size at different periods of the annealing treatment is measured in subsection 4.4.2, and the dependency of the recrystallized grain size on the initial grain size from Eq.2.20 is evaluated. It is important to mention here that the grain size calculations is associated to the equivalent grain diameter, using the area of the respective grain. The process of the refinement of grains to form equiaxed granular structures can be illustrated with the shape factor. Finally, the initial and final grain size distribution, which is experimentally calculated is compared with Sellars equation (Eq.2.20) in subsection 4.4.3.

4.4.1 Quantification of Recrystallized Grains and Deformed Grains

The quantification of recrystallized and deformed grains is estimated using the GAM technique described in the previous section. As predicted from the literature, the recovery and recrystallization nucleation process allows the formation of new grains that begin to grow with continuous annealing time, eventually consuming the deformed grains, as a result of the driving force. The experimental observation of the SRX phenomenon for this alloy has been depicted in Fig.4.14. The high resolution maps with a step size of 0.5μm are selected for this illustration, since the experimental results have suggested that the high resolution maps provide higher accuracy for the quantification of grains, in comparison to the lower resolution maps despite having a larger scanned region.

In order to experimentally validate the quantification results of the smaller scanned region, additional sets of data are required for comparison. Therefore, the high resolution EBSD scans for three different regions of the specimen are utilized and subsequently compared in this research study. These three different regions along the central axis of the specimen have been defined in subsection 3.4.1 as: upper, central and lower regions.

From Fig.4.5(b) & (c), we observe that recrystallization nucleation transpires in the deformed sample within 1s annealing time, which indicates that the recovery process is extremely accelerated, in comparison to other alloys in the literature[15]. The accelerated recovery process in this research study could be due to the absence of

micro-alloying elements such as Niobium, which is known to retard the recrystallization process via the solute drag and grain boundary pinning effects [11]. Nevertheless, the recrystallization process is observed to continue upto 50s of the annealing time, and gradually reduces at 100s annealing time, where the SRX phenomenon eventually transitions into the grain growth process. The grain growth process which begins after 100s consumes the smaller recrystallized grains, and reduces the overall recrystallized grain boundary area, as seen finally in Fig.4.14(f) & (i) for the 500s annealed specimen. Similar trends have been experimentally observed for the other two regions of the specimen and their discrepancies have been reported below, using the graph in Fig.4.15.

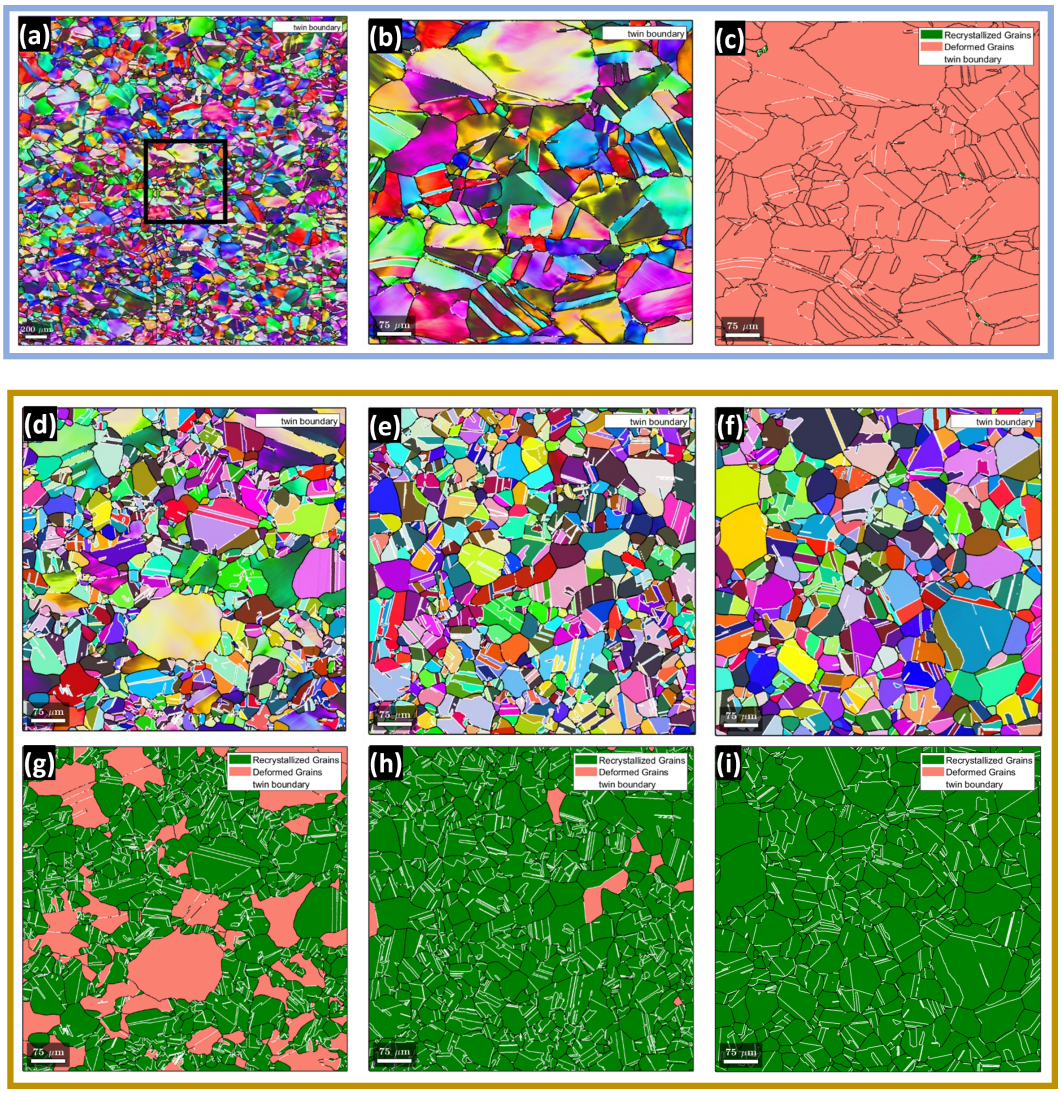

FIGURE 4.14: **(a) A central region of the 1s annealed specimen is selected. (b) High resolution EBSD IPF map of 1s annealing time. (c) Corresponding micrographical representation of recrystallized and deformed grains. (d), (e), (f) High resolution EBSD IPF maps of 50s, 100s and 500s annealing time, respectively. (g), (h), (i) Representation of the recrystallized and deformed grains for 50s, 100s and 500s annealing time, respectively. The twin boundaries are represented in white and the IPF maps follow the similar colour code using Fig.4.5.**

From Fig.4.15, the number of deformed grains present after deformation for the 3 regions in the specimen is similar for all three regions of the specimen. The central region of the specimen is observed to have an intermediate value of 730 deformed grains/mm^2 after deformation. There is a minute possibility for few recrystallized grains to be present from these 730 grains/mm^2, as observed in the maps after deformation, which has been carefully reported in this graph. However, as literature suggests [15], these recrystallized grains are presumed to be formed during deformation, and hence considered to be an experimental error, which is neglected for further nucleation rate calculations. Additionally, the statistical error bars have been calculated as statistical standard deviation for every data point in the graph.

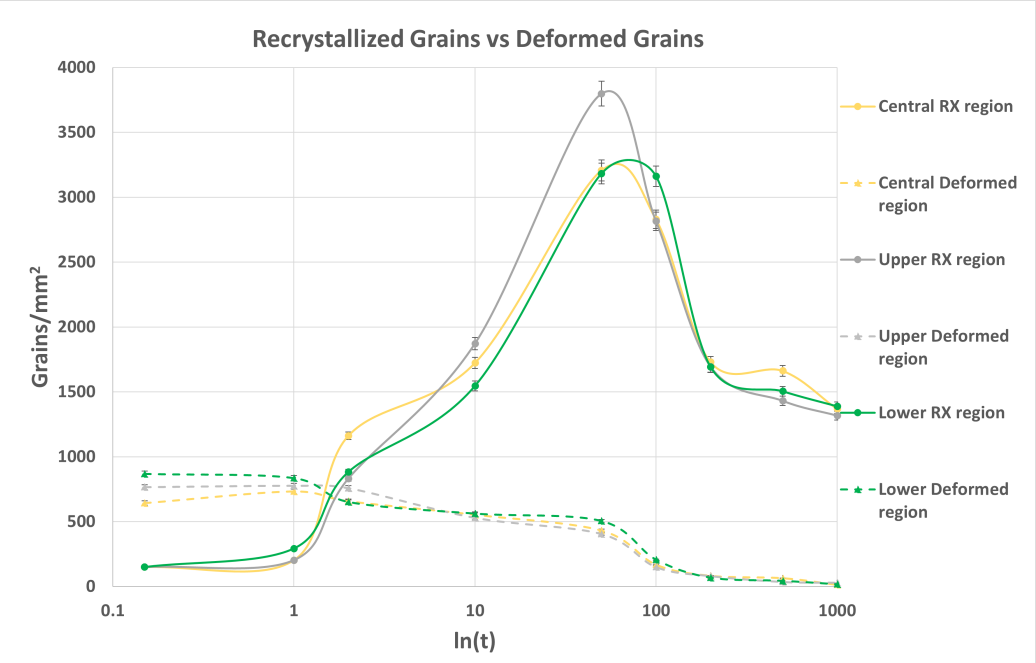

FIGURE 4.15: **Quantification of Recrystallized (RX) and Deformed grains in the 3 different regions of the specimen, for different annealing time intervals**

The quantification results from Fig.4.15 distinctly describe the expected SRX phenomenon described in the literature. Initially at 1s annealing time, the lower region of the specimen experiences highest recrystallization nucleation due to presence of the greater number of deformed grains, which directly provides more number of potential nucleation sites for the SRX phenomenon, as compared to the other two regions. Also, deformation accumulation in the lowest region could be the most prominent, which will be investigated in the next section. The number of initial nuclei formed at 1s annealing treatment for the lower region of the specimen is approximately 100 recrystallized grains greater than the other two scanned regions. The highest nucleation effect at this lower region, finally results in the reduction of the number of deformed grains, as seen after 1s annealing time. This effect observed from the experimental results confirms the consumption of deformed grains at a much earlier stage, if there are greater number of nuclei formed. After the substantial development of the number of nuclei at 1s for the lower region, the recrystallization nucleation process thereafter decreases here continuously (compared to the central and upper regions), which causes the deformed grains also to be consumed

at a much slower rate thereafter. The reason for this change in nucleation trend for the lower region could be due to the consumption of significant nucleation sites initially at 1s. Therefore, after 10s of annealing treatment for the lower region, the number of deformed grains is the greatest in comparison to the other two regions, and consequently, the number of recrystallized grains present becomes the least. Furthermore, this decrease in recrystallization nucleation after 1s, for the lower region of the sample, is compensated by additional recrystallization nucleation rate after 50s, seen from the wider green peak in the graph. The other two regions observe a much faster decrease in the number of recrystallized grains since all the nucleation sites have been consumed, and the SRX phenomenon can transition into the grain growth process.

For the upper region of the specimen, the number of recrystallized grains increases steadily at every point of the annealing treatment, indicating that steady-state nucleation is achievable for some regions of the specimen. Also, after the 50s peak, the decrease in the number of recrystallized grains in the upper region, decreases at a steady-state until the end of the recrystallization phenomenon. This steady-state decrease in the number of recrystallized grains for the upper region is however faster than the other two regions, since all the potential nucleation sites are consumed, based on the substantially larger number of recrystallized grains for the upper region at 50s annealed specimen. However, the number of recrystallized nuclei at 50s in the upper region has a large deviation in comparison to the other two regions, by comparing the maximum peaks of the different recrystallized curves. This large difference could be an experimental error, which requires to be investigated further, since the 50s annealed specimen is known to have slight deviations in the stress-strain curves, as seen in Fig.3.2(a).

Finally, the central region of the specimen is known to observe a large number of recrystallized grains at 2s annealing time, as compared to the other regions. The central region is observed to have approximately 350 more total recrystallized grains after 2s of the annealing treatment, which can be observed by the yellow bulge at 2s of the annealing treatment. This is an intensified phenomenon similar to the earlier described phenomenon in the lower region of the 1s annealed specimen. Finally, between 200s and 500s, the total number of recrystallized grains at the central region does not considerably decrease like the other two regions, thereby delaying the final grain growth process. This unusual trend provides an inference that there could be a period during the grain growth process, where the recrystallized grains have lesser driving force (dependent on the boundary curvature) to grow in the central region, as compared to the other two regions. However, at the end of the annealing treatment (1000s), we observe that all the 3 regions of the specimen have a similar number of recrystallized grains that are fully grown (approximately, 1350 grains/mm^2). Therefore, this declares that after 500s, the central region of the specimen acquires the necessary driving force and higher grain growth rate required to complete the grain growth process. Towards the end of the annealing treatment, it has been experimentally observed that there are a few deformed grains still present, which occupy a negligible fraction of the scanned region. These deformed grains which have a negligible grain size after 1000s of the annealing treatment can be considered as an experimental error due to inaccessibility to calculate the average misorientation angles for the grain because of insufficient pixels within the grain, thereby predicting high GAM values that do not remain lower than the cut-off GAM values.

4.4.2 Average Grain size at different annealing times

Using the grain detection and denoising techniques from subsection 3.4.1 and 3.4.2, the grains can be computed from the EBSD scans. Additionally, on incorporating the merging grains function from subsection 4.2.3, the grains consisting of former twin boundaries and annealing twins can be avoided when calculating the grain size of the parent grains. Therefore, the grain size can be calculated from the different EBSD scans, without considering the irregular distribution of the Σ3 twin orientation relation within grains. Additionally, the grains along the corners of the scanned region can be removed to avoid statistical errors in the grain size. However, neglecting such grains have not shown any deviation in the overall grain size calculations, and hence is not conducted in this research study.

The grain size calculations can be done using two different functions that involve the diameter or the equivalent diameter. The function *diameter* is the special case of the Feret or caliper diameter, which is essentially a one dimensional projection of the longest distance between any two grains. The diameter measured from this function is only accurate when all the grains are spherically shaped(circular in 2D), whereas experimentally the grains are either elongated/pancaked after deformation and equiaxed after recrystallization. By contrast, the function *equivalent.radius*, provides us with a more realistic and equivalent measurement of the grain size, since it calculates the diameter of the circle that has the same area as the grain. For the purpose of this research study, the grain size is defined using the approximation method of the equivalent grain diameter. Finally, from experimental grain size calculations, the two different diameter measurement methods provide a relation such that the Feret diameter is approximately 1.4 times larger than the equivalent grain diameter.

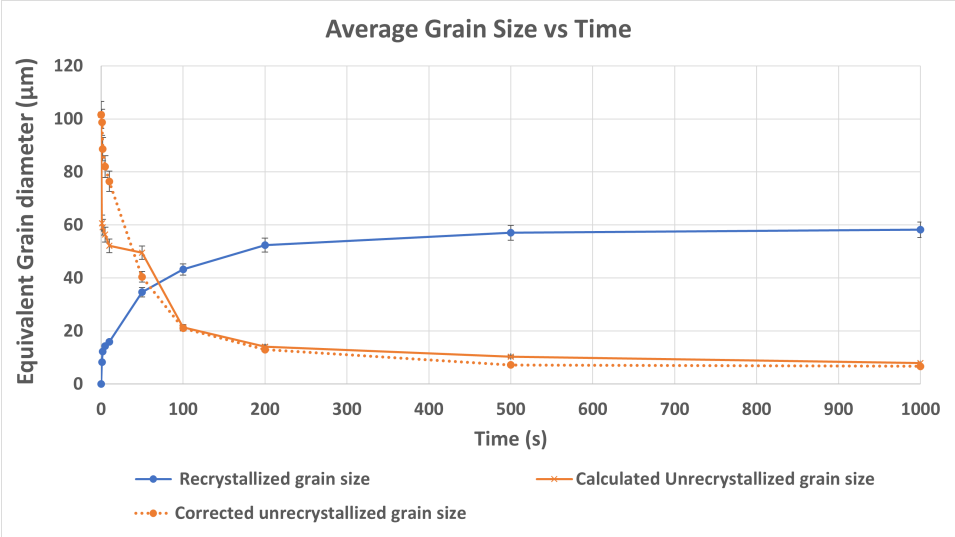

FIGURE 4.16: **Average grain size for different annealing time intervals, measured by the equivalent grain diameter method**

Fig.4.16 provides the results of the average grain size for the different annealing time intervals. The error bars are estimated using the standard deviation for each data point. The recrystallized grain size(referred to as D_{rex}) is observed to increase gradually upto 10s annealed sample, where the recrystallized grain size is assumed to be approximately zero for the EBSD scans before and after deformation. The initial

recrystallized grains have an average grain size of 8.25μm at 1s annealing treatment and increases gradually to 16μm at 10s annealing treatment. This gradual increase in grain size can be accounted due to the continuous recrystallization nucleation occurring at the different nucleation sites. Thereafter, the recrystallized grain size increases quickly to 34.60μm and 43.18μm at annealing time intervals of 50s and 100s, respectively. Thereafter, the final spike in the recrystallized grain size is observed after 200s with 52.36μm, mainly due to grain growth process. The recrystallized grain size continues to grow by a minute margin until the end of the annealing. The marginal increase in grain size between 500s and 1000s can be attributed to the rapid grain growth process occurring only in the central region of the sample, as verified in subsection 4.4.1.

On the contrary, the deformed/unrecrystallized grain size(referred to as D_{urx}) calculations are far more complex due to the loss in grain boundary character of the former twins after deformation. Therefore, the current merging grain function used for these grain size calculations is not beneficial for the unrecrystallized grain size, as seen by the vast decline of approximately 40μm, before and after deformation. Practically, such a drastic decline is unreasonable. This complication is not encountered in the recrystallized grain size calculations, because of the annealing twins formed in the recrystallized grains during the annealing treatment. Hence, a different pragmatic approach is attempted to predict the unrecrystallized grain size by taking into consideration the former twin boundaries that have lost their grain boundary character. This approach assumes the similar former twin density (before deformation) of 48.83% with respect to the total grain boundary length, for the deformed grains in the respective EBSD scans. Finally, the adapted merged grain function from this approach estimates a much smaller and reasonable decline in the unrecrystallized grain size of approximately 3μm, where the grain size before deformation(D_0) and after deformation(D_{urx}), is 101.50 μm and 98.60μm, respectively. In other words, the assumed corrected unrecrystallized grain size (at different annealing time intervals) is approximately 2 times larger than the unrecrystallized grain size calculations conducted without merging. The unrecrystallized grain size without merging has been reported in Appendix section A.2. Towards the end of the annealing treatment, the calculated and corrected unrecrystallized grain size are similar, since the number of deformed grains present in the scanned region is almost negligible. Finally, predicting the corrected unrecrystallized grain size using this assumption, allows us to comprehend the consumption of the deformed grains during the SRX phenomenon.

4.4.3 Initial and Final Grain size distribution

The initial grain size is known to be a crucial parameter for industrial purposes. The deformation of a coarse-grain material is known to provide inhomogeneities within the grain that allow the formation of deformation bands. These deformation bands can behave as nucleation sites but require higher deformation strains for the accumulation of deformation [45]. By contrast, the deformation of a fine-grain material is known to facilitate highly rapid recrystallization kinetics, because of the presence of greater grain boundary length [45]. So, the presence of fine-grains in the microstructure can provide a large driving force between grain boundaries, behaving as nucleation sites for the SRX phenomenon. Therefore, to measure the recrystallization kinetics accurately, the initial microstructure must comprise of a combination of both fine-grains and coarse-grains to guarantee a desired final grain size, based on the applied deformation conditions. The Ni-30Fe alloy used for this study comprises

of both coarse-grains and fine-grains, as observed from the EBSD IPF in Fig.4.3(a), and the grain size distribution in Fig.4.17. Using the grain size calculations from subsection 4.4.2 and consideration of the former twin boundaries with the merging grain function, the initial average grain size, D_0, is 101.50 $\pm$ 2.53 μm.

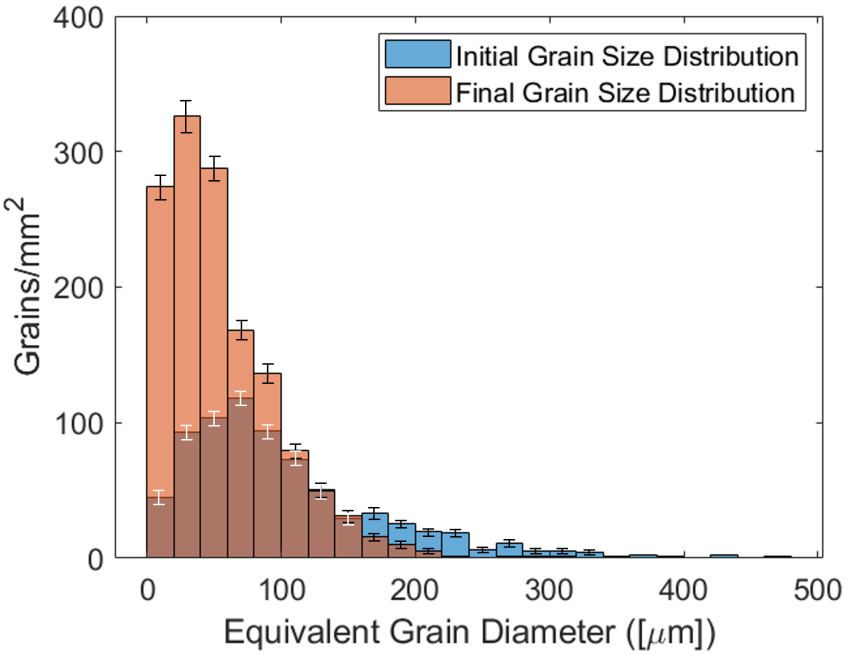

FIGURE 4.17: **Initial and Final Grain Size Distribution (mm^{-2} of the Ni-30 Fe alloy**)

From Fig.4.17, the initial grain size distribution is compared with the final grain size distribution, where the error bars have been calculated using the standard deviation for each bin count. From this grain size distribution, we can confirm that the annealing treatment with the defined strain and temperature conditions, has allowed the refinement of grains to occur within the material. The log-normal distribution from these two EBSD measurements is a good indication that the grains have a combination of both fine-grains and coarse-grains, with the recrystallized grains attaining the peak in the distribution prior to the initial grain size. The final grain size after the annealing treatment(1000s annealed specimen) has an average grain size of 58.18 $\pm$ 1.45μm.

These experimental grain size calculations using the equivalent grain diameter measurement method can be compared with Sellars equation described in Eq.2.20. The dependency of the recrystallized grain size on the initial grain size is calculated using the logarithmic form of the average grain sizes at different annealing periods. The slope from this dependency, referred to as n, is calculated to be 0.67, which is in good agreement to the Sellars model [52]. The other parameter from the Eq.2.20, p, is a function of the temperature and strain, which is assumed to be 1 for a C-Mn steel. Finally, the average recrystallized grain size D_{rex}, is predicted to be 56.92μm with the Sellars model [52]. This is in good agreement with the experimental value calculated at the end of the annealing treatment.

As observed from the literature, one of the main requirements from the SRX phenomenon is to achieve the refinement of grains and an equiaxed structure with respect to the initial microstructure. The refinement of grains has already been validated with the statistical calculations of the final grain size distribution in Fig.4.17. Additionally, from Fig.4.18, the shape factor has been calculated for the initial and final microstructure after deformation. The shape factor can be defined as the ratio between the actual perimeter measured and the grain polygon equivalent perimeter (measured as 2πR, where R is the equivalent radius). The rule of thumb states that the shape factor will consistently be greater than 1, since the actual perimeter is always greater than the equivalent perimeter, because the grains are not absolutely spherical in shape. It is desirable the that oddly shaped and elongated grains after deformation(from Fig.4.18(a)), subsequently acquire an equiaxed microstructure (Fig.4.18(b)), which would be similar to or better than the microstructure before deformation. The elongated grains are highly unstable due to presence of residual stresses which can lead to hot tearing of the rolled sheet [15]. Therefore, the grain growth process ensures that the recrystallized grains which have initially developed, continue to grow in all directions attaining an equiaxed(rounded) microstructure, after consuming the elongated deformed microstructure.

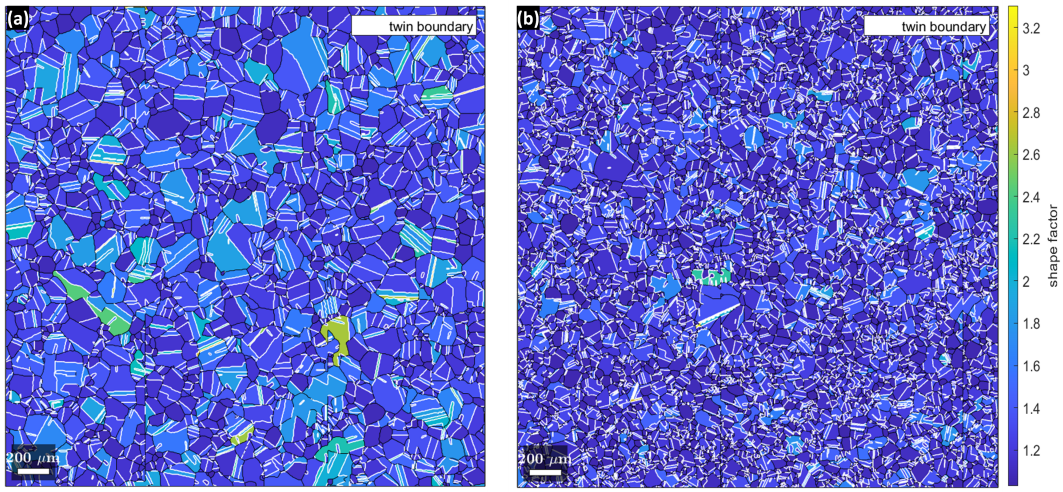

FIGURE 4.18: **Shape factor for EBSD scans, where, (a) After Deformation specimen and; (b) 1000s annealed specimen**

Finally, the outcome of the grain growth process is determined by the initial recovery and recrystallization nucleation processes. These processes have been further investigated in the following sections by experimentally estimating the deformation measurements, the dislocation densities, the driving force for nucleation, its corresponding nucleation mechanism, and ultimately predicting the recrystallization kinetics.

4.5 Dislocation Density and Stored Energy

After deformation, the phenomenon of static recovery and recrystallization during the annealing treatment can be formulated and analyzed using the dislocation densities. The dislocation densities are experimentally measured with the MTEX software using the adopted approach from literature [23]. The high resolution maps with

0.5μm step size and scanned regions of approximately 0.49mm^2 are used for the determination of the dislocation densities. The high resolution maps are proposed to capture a greater number of dislocations, since the number of indexed pixel orientations measured is much higher (validated from Table.3.2), as compared to the bulk dislocation density which have lower indexed pixel orientations shown in Table.3.1. It is important to note that the dislocations measured from 2D EBSD only comprise of GNDs. Even though the SSDs are to be considered for the total dislocation densities, they have been neglected in this research study, since only the GNDs are quantifiable from the 2D EBSD scans. Future research using anelastic measurements are being conducted to capture the deformation behaviour and total dislocation densities for the Ni-30Fe alloy. In this section however, the GND density measurements are initially compared with KAM maps, in order to validate the methodology used in the literature. Thereafter, the effect of recovery and recrystallization is analyzed by the change in the average dislocation density. Then, the measured dislocation densities is utilized to estimate the stored energy(S_E) using the Dislocation Line Energy(DLE) method, and compared with the approximation method.

4.5.1 KAM and Dislocation Density

The high resolution KAM maps are determined in the similar method as done for the low resolution KAM maps. The KAM maps can be determined for each pixel by incorporating Eq.2.1 and taking into consideration the number of nearest neighbours (neighbouring pixels are considered only in the same grain), and the threshold angle ($\Delta\theta_{\text{threshold}}$). The KAM maps for the central region of the specimen are shown for 1s, 10s, 50s and 100s in Fig.4.19 (b), (d), (e) and (f) respectively. Correspondingly, the GND density maps for the central region of the specimen are shown for 1s, 10s, 50s and 100s in Fig.4.19(c), (d), (e) and (f), respectively.

The GND density map is dependent on four main parameters as defined in Eq.2.2. Firstly, the local misorientation calculated from the KAM maps are stored for the parameter, $\Delta\theta$. Secondly, the curvature tensor is stored for the parameter, κ, is defined as a rank two tensor (matrix) that is specifically designated for every pixel in the EBSD scan, by the directional derivatives in x, y and z direction. Thirdly, the principle dislocations are defined by their Burgers or line vectors, calculated to be b=2.48Å from the dislocation system for an FCC material, which is also confirmed from the literature [23] for the Ni-30 Fe alloy. Finally, the step size of the scanned specimen Δx = 0.5μm is detrimental for the GNDs, as mentioned above, which is essentially the distance between the measured pixels.

After the consideration of these 4 parameters, the dislocation tensors generated can be assigned to each pixel in the map by a method of "fitting", carried out by the *fitDislocationSystems* function. It is important to note that this GND estimation procedure contains tremendous data noise. Hence, denoising techniques(Half quadratic filter) from subsection 3.4.2 is implemented, to avoid the noisy orientation data that may possibly lead to overestimation of the GND density. Furthermore, with respect to the unit of the GNDs, a factor of 10^{16} is multiplied with the dislocation tensors for conversion to SI units (m^{-2}). This factor considers the units of the curvature tensor and burgers vector, which is initially estimated in μm and Å, respectively.

Finally, the error for the GND densities are estimated using Eq.2.3 from the literature. This error percentage mainly accounts for curvature tensor, such that $\delta\kappa/\kappa$ = 13%,

given that $\Delta\theta$ = 15°(with a misorientation error of $\delta\theta$ = 0.5°), and Δx = 0.5μm(with a spatial resolution error of δx = 0.05μm) [23]. This curvature tensor error is incorporated after the average of the GND density is calculated, by measuring all three regions(upper, central and lower) of the annealed specimens, for: the recrystallized grains, deformed grains and the whole sample. The three regions of the specimen have similar recrystallization fractions at the different annealing time intervals, and hence the calculated average from the three regions improves the accuracy and reliability of the calculated GND densities.

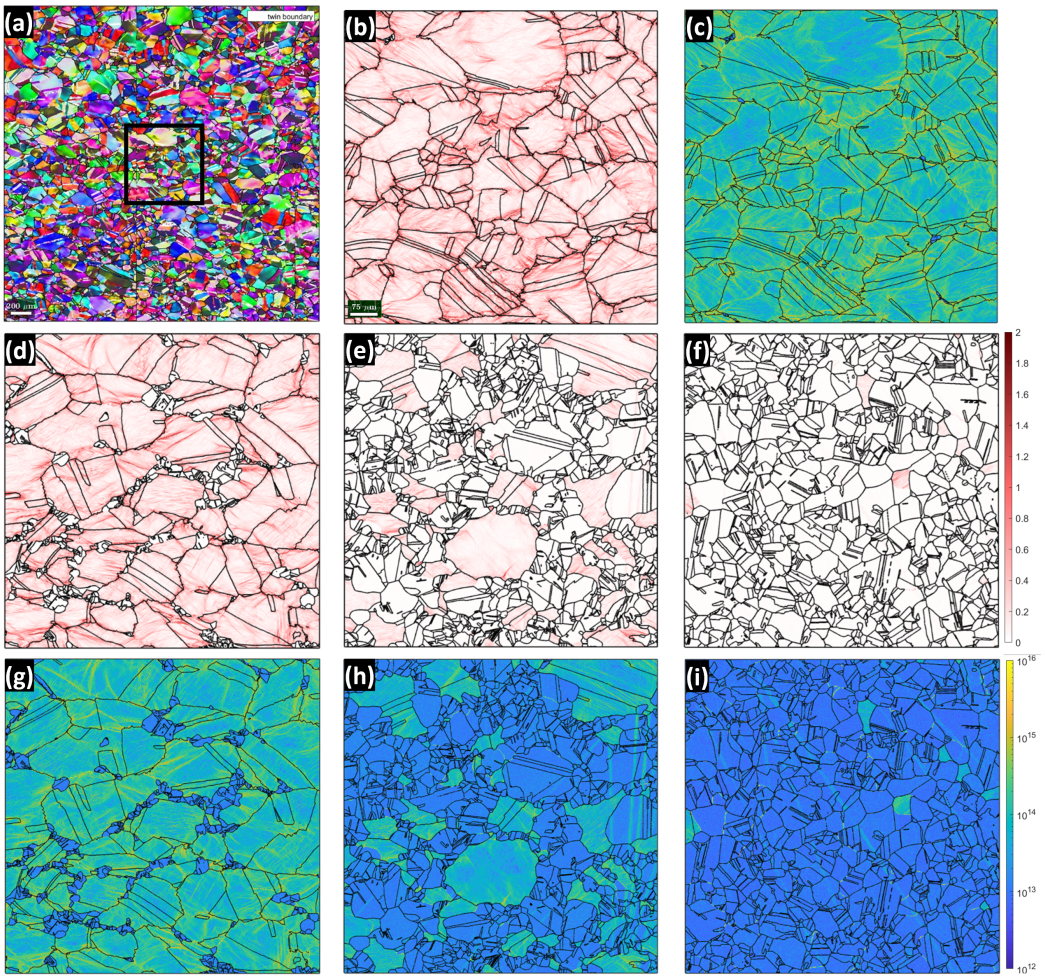

FIGURE 4.19: **EBSD IPF map of the 1s annealed specimen is shown in (a). The central region is selected to investigate the corresponding KAM and GND density maps in (b) and (c), respectively. (d), (e) and (f) are the KAM maps for the central region of the 10s, 50s and 100s, respectively. (g), (h) and (i) are their corresponding GND density maps. The colour coding scale for the KAM map is shown from 0-2°and; the colour coding scale for the GND is shown from 10^{12}-10^{16} m^{-2}**

4.5.1.1 Effect of Recovery and Recrystallization

The evolution of the GND densities, followed by arrangement and annihilation of the GNDs during static recovery and recrystallization has been captured individually for the three different regions of the specimen. The average of the GNDs for

the different regions of the specimen have been quantified in Fig.4.20, along with the reported 13% error for the curvature tensor. The highest amount of deformation is observed by the KAM intensity in the 1s annealed specimen, where deformation bands are visible in the deformed coarse-grains (seen in Fig.4.19(b)). Additionally, deformation accumulation is visible mainly along the grain boundaries and triple junctions, as experimentally observed in Fig.4.19(c). These GNDs are expected to exist as forests which can be found as kinks or jogs, with intricate tangles and pile ups [15].

The slight increase in GND density between the after deformation and 1s annealed specimen for the deformed grains is due to the GND density discrepancy in individual grains. The whole sample GND density however remains the same for the two cases as a result of the recrystallization nucleation that begins around 1s of annealing. The recrystallization nucleation process is experimentally visible from Fig.4.19(c) at few triple junctions of the GND density map. The mechanism and nucleation sites for the recrystallization process is discussed further in subsection 4.6.1. Finally, the deformed GND density is observed to be maximum for the lower region of the specimen during the 1s annealing treatment (approximately 5 x 10^{14}m^{-2} shown in Appendix section A.3), validating the hypothesis from section 4.4.1, i.e, the number of recrystallized grains formed, is approximately 100 grains greater as a result of deformation accumulation in comparison to the other two regions (where, the GND density is approximately 4.7 x 10 ^{14}m^{-2} shown in Appendix section A.3). This similar situation for the deformed GND density has been observed for the central region of the 2s annealed specimen.

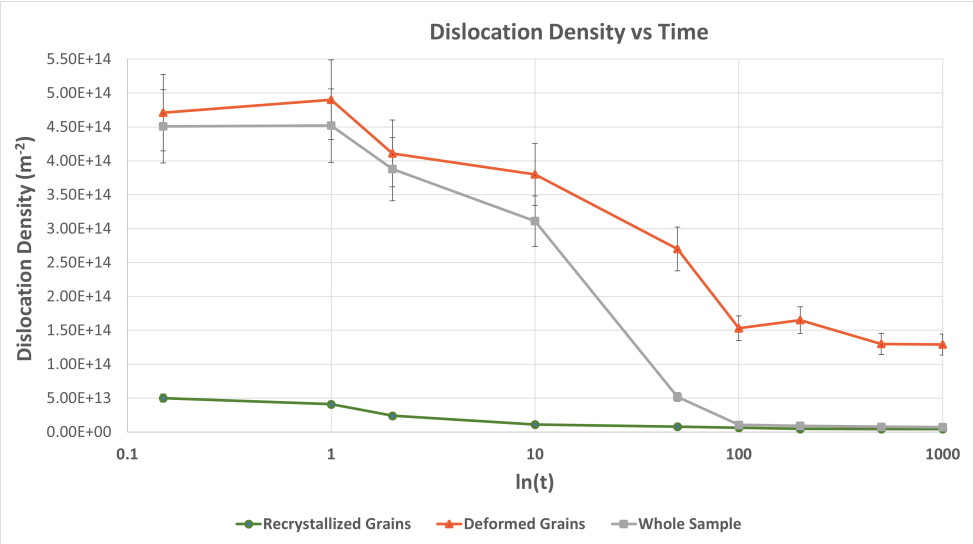

FIGURE 4.20: **GND density for different periods of the annealing treatment**

The KAM intensity in the 10s annealed specimen is of a lower deformation degree (seen in Fig.4.19(d)) compared to the 1s annealed specimen, as a result of the static recovery occurring within the material. The result of static recovery is also visible in the graph, where the dislocation density of the whole sample decreases from approximately 4.52 x 10^{14}m^{-2} to 3.11 x 10^{14}m^{-2} after 10s of the annealing treatment, validating the annihilation of dislocations. The new recrystallized grains formed

along the grain boundaries and triple junctions are distinctly visible by the KAM and GND density maps (seen in Fig.4.19(d) and (g)).

The micro-graphical representation of the GND density clearly differentiates between recrystallized and deformed regions, which is further validated by the quantification of the GND densities in Fig.4.20. The static recovery in the specimen which allows the annihilation of dislocations, can be observed by the difference in GND densities (approximately of the order $10^1 m^{-2}$) between the deformed and recrystallized grains. Further research can be conducted to extensively study the recovery process by utilizing the modified version of of Friedel's model in the literature [58]. Finally, the recrystallized regions visible in the GND density maps, which essentially involves the KAM measurements, is similar to the GAM technique that averages the KAM measurements for a grain. The similarity observed with the estimation of recrystallized grains and fractions using the GND density procedure, in comparison to the earlier utilised GAM technique, validates the selected recrystallization separation method. The experimental recrystallization kinetics is further discussed in section 4.7.

Thereafter, as the recrystallization fractions increase as a result of the SRX phenomenon, the GND density observes a drastic decline to approximately $5.18 \times 10^{13} m^{-2}$ after 50s of the annealing treatment. Additionally, the GND density of the deformed grains also continuously decreases as a result of the static recovery, as observed in Fig.4.19(h) and the quantification in Fig.4.20. Finally, it is observed that the recrystallization process is completed at 100s of the annealing treatment, where the overall GND density in the whole sample is more or less similar to the recrystallized GND density. Therefore, majority of the grains are expected to have low KAM deformation degree and low GND density as observed in Fig.4.19(f) & (i), respectively. The remaining deformed grains at this stage are further consumed by the grain growth process, based on the mobility of the recrystallized grain boundaries. At the end of the annealing treatment, the effect of the static recovery and recrystallization process can be observed by the overall decline in the GND density of the whole sample to approximately $7.28 \times 10^{12} m^{-2}$. The measured GND densities from this subsection is essential to estimate the driving force required for the SRX phenomenon, which is reported in the next subsection.

4.5.2 Quantification and comparison of Stored Energy

The GND density calculations carried out in this research are essential, since it affects the deformed stored energy(S_E) present in the material. The continuous decrease in the GND density of the whole sample as observed from Fig.4.20 is a result of the recovery taking place. The effect of recovery can also be captured by taking the stored energy as a function of time (t). As recovery continues during the annealing treatment, the formation of sub-grains occurs as a result of the arrangement of the dislocations in a lower energy configuration. The migration of the sub-grain boundary provided by the stored energy difference(driving force) between grain boundaries causes the recrystallization process to take place during the annealing treatment. The driving force can be estimated using the subgrain size and subgrain boundary energy [15]. However, this would require a higher resolution EBSD scan in the order of 100nm to be conducted for an extremely small scanned area. This approach to calculating the driving force for recrystallization can be used for future research.

In the current research study, the stored energy is estimated using the GND density, which is directly proportional to the stored energy, as seen from the literature in Eq.2.5 and Eq.2.6. The difference between the two equations essentially lies in the calculation of the dislocation line energy(DLE) per unit length of dislocation. The DLE is dependent on 3 main parameters. Firstly, the higher and lower radius limit for separating the dislocations, which is estimated to be 1μm and 6.25Å, by using $\sqrt{\rho_{GND}}$ and doubling the length of the burgers vector, respectively. Secondly, the DLE is also dependent on the shear modulus, *G*, estimated to be 42GPa at 900°C, using the approximation from the literature [11]. Thirdly, the Poisson's ratio function is estimated for 12 edge and 6 screw dislocation systems. Finally, on averaging the dislocation systems for the edge and screw dislocations, the estimated DLE per unit length of the dislocation is 1.38 x 10^{-9} J/m. Thereafter, the combination of the DLE with the measured GND densities at different annealing times, results in the stored energy as a function of time(t), which is reported in Appendix section A.4. Using the recrystallization fractions validated with the GAM technique, the stored energy follows a similar trend to the GND density graph, since the stored energy consists of the above mentioned parameters that do not change irrespective of time.

The stored energy is estimated to be: 5.67x10^4J/m^3, 6.78x10^5J/m^3 and 6.26x10^5J/m^3 for the recrystallized grains, deformed grains and whole sample, respectively, after 1s of the annealing treatment. This DLE method is dependent on the formation of dislocation forests, which can be observed by the orientation gradients in the figures of subsection4.6.1. By contrast, the stored energy approximation method from Eq.2.6 considers only the GND densities, shear modulus (*G*) and the burgers vector norm (b). The stored energy from this approximation method is estimated to be: 5.04x10^4J/m^3, 6.03x10^5J/m^3 and 5.56x10^5J/m^3 for the recrystallized grains, deformed grains and whole sample, respectively, after 1s of the annealing treatment. The reported values in the literature [15], states that the stored energy is estimated to be between 2x10^6 - 2x10^7 J/m^3, after the deformation of a material. However, these values are a further approximation for different materials. Therefore, for our alloy compositions and deformation conditions, the reported stored energies using the above methods is relevant for this research, considering the percentage error estimated from the dislocation densities to be 13% using the curvature tensor approach. Ultimately, despite the precision obtained for the stored energy quantification, there has to be the addition of this 13% error for the stored energy, which is the consistent error during the entire annealing treatment.

Following the recovery, recrystallization and grain growth processes, the stored energy using the DLE method is estimated to be: 9.95x10^3J/m^3, 1.79x10^5J/m^3 and 1.01x10^4J/m^3 for the recrystallized grains, deformed grains and whole sample, respectively, after 1000s of the annealing treatment. By comparison between the start and end of the annealing treatment, we observe that the stored energy decreases by approximately 5.4x10^4J/m^3 for the whole sample, as a result of the static recovery and recrystallization process. Subsequently, the stored energy using the approximation method is estimated to be: 8.81x10^3J/m^3, 1.59x10^5J/m^3 and 8.96x10^3J/m^3 for the recrystallized grains, deformed grains and whole sample, respectively, after 1000s of the annealing treatment. Finally, the evaluation of both the measurement methods allows us to infer the reliability of the measured DLE per unit length of the dislocation. The DLE method is observed to be slightly higher as compared to the approximation method, such that: *DLE method = 1.13 * Approximation method*. This validates that Eq.2.5 and Eq.2.6 produce similar results. However, the slightly

higher estimation of the stored energy using the DLE method could be due to the complexity involved in calculation of the average Poisson's function, which uses the edge and screw dislocation systems of the FCC material.

In conclusion to this section, the dislocation densities have been measured by adopting the approach from the literature, where only the GNDs have been obtained. The effects of recovery and recrystallization has been validated by the continuous reduction in stored energy with time. The quantification and comparison of the stored energy using physical equations from literature explains the importance of the dislocation line energy per unit length of the dislocation. Finally, the measured values in this section for the annealing treatment provides the required driving force for the SRX phenomenon. However, this arises relevant issues regarding the mechanism, nucleation sites and the nucleation rate, which will be experimentally investigated and compared with physical models in the following section.

4.6 Primary Static Recrystallization

The residual dislocations during the recovery process is known to arrange themselves in lower energy configurations which allow the formation of sub-grains. The growth of these sub-grains formed during recovery results in recrystallized nucleation, which involves a particular mechanism experimentally depicted in this section. Additionally the mechanism of this nucleation occurs at certain nucleation sites which are explored in this section. Then, the critical size for bulging is calculated from Rehman et al.[11] model, and plotted with the average recrystallized radius, using the experimental grain size calculations from subsection 4.4.2. Thereafter, the nucleation rate is estimated, using the quantification of recrystallized grains from subsection 4.4.1. Finally, the nucleation framework modelling described in the literature is incorporated in this research study, which is subsequently compared and discussed with the experimental nucleation rate.

4.6.1 Nucleation: Mechanism and Sites

The earlier work conducted by Bailey and Hirsch[59], suggests that the recrystallization nucleation process for single-phase materials proceeds by SIBM during low strains($\epsilon < \epsilon_c$). The other mechanism for nucleation, by continuous sub-grain growth is only viable for larger strains, where $\epsilon > \epsilon_c$, and hence observed to be more prominent for dynamic recrystallization of the material. Since, SRX phenomenon is the main focus of this research study, the SIBM mechanism has relevance, where the driving force for nucleation is generated by the difference in measured dislocations between grains, which has to be greater than the capillary forces, $2\gamma_{SE}/r(t)$. This nucleation criterion allows us to develop the requirements for the critical sub-grain size required for bulging, as described by Eq.2.9 in the literature. From this equation, the critical sub-grain size for bulging(r_c) is inversely proportional to the stored energy between grains(driving force) and directly proportional to the grain boundary energy(γ_{SE}). As mentioned in the literature [11], the capillary forces is initially expected to be greater than the stored energy between grains, due to the induced homogeneous deformation. However, as the sub-structural recovery continues after deformation, the driving force becomes sufficient enough to overcome the capillary forces due to the growth of the sub-grains along the boundary. Even though the growth of the sub-grains cannot be currently captured, the bulging of the HAGBs is clearly visible in the purple circled regions of Fig.4.21(a) and (c), indicating that the

capillary forces is overcome by the growth of the sub-grains, thereby allowing the migration of the HAGB. This experimentally validates that the primary mechanism for the recrystallization nucleation is by SIBM, which can be defined as the bulging of an already present HAGB that consumes the nearby deformed microstructure, leaving a dislocation annihilated zone behind the migrating boundary.

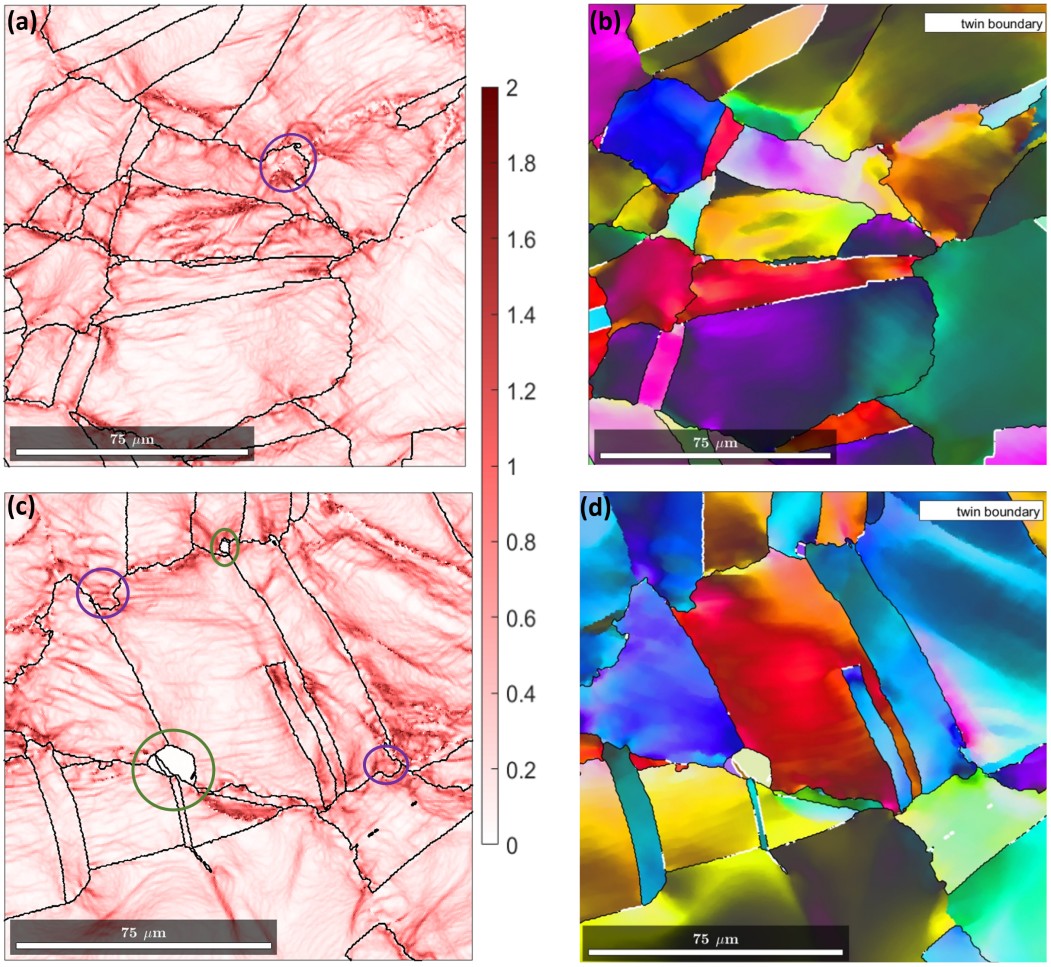

FIGURE 4.21: **Nucleation mechanism after 1s of the annealing treatment. (a) & (c) KAM maps of different regions in the 1s annealed specimen and; (b) & (d) Respective EBSD IPF maps of the corresponding zoomed in regions.**

The purple circled regions of prominent bulging zones after 1s of the annealing treatment can be further observed in the corresponding EBSD IPF maps shown in Fig.4.21 (b) and (d). The misorientation accumulation from the orientation gradients in such regions, can be interpreted as the dislocation annihilation that allow the growth of the sub-grains into the surrounding grain, due to the presence of a higher driving force. The presence of a higher driving force is observed for certain regions of the microstructure, which can be described by the different potential nucleation sites for recrystallization nucleation. The validated SIBM mechanism is observed to occur primarily at triple junctions in the initial phase of the annealing treatment (1s and 2s annealed specimen), as observed by the viable nuclei already formed at some triple junctions (seen in the green circled regions in Fig.4.21(c)).

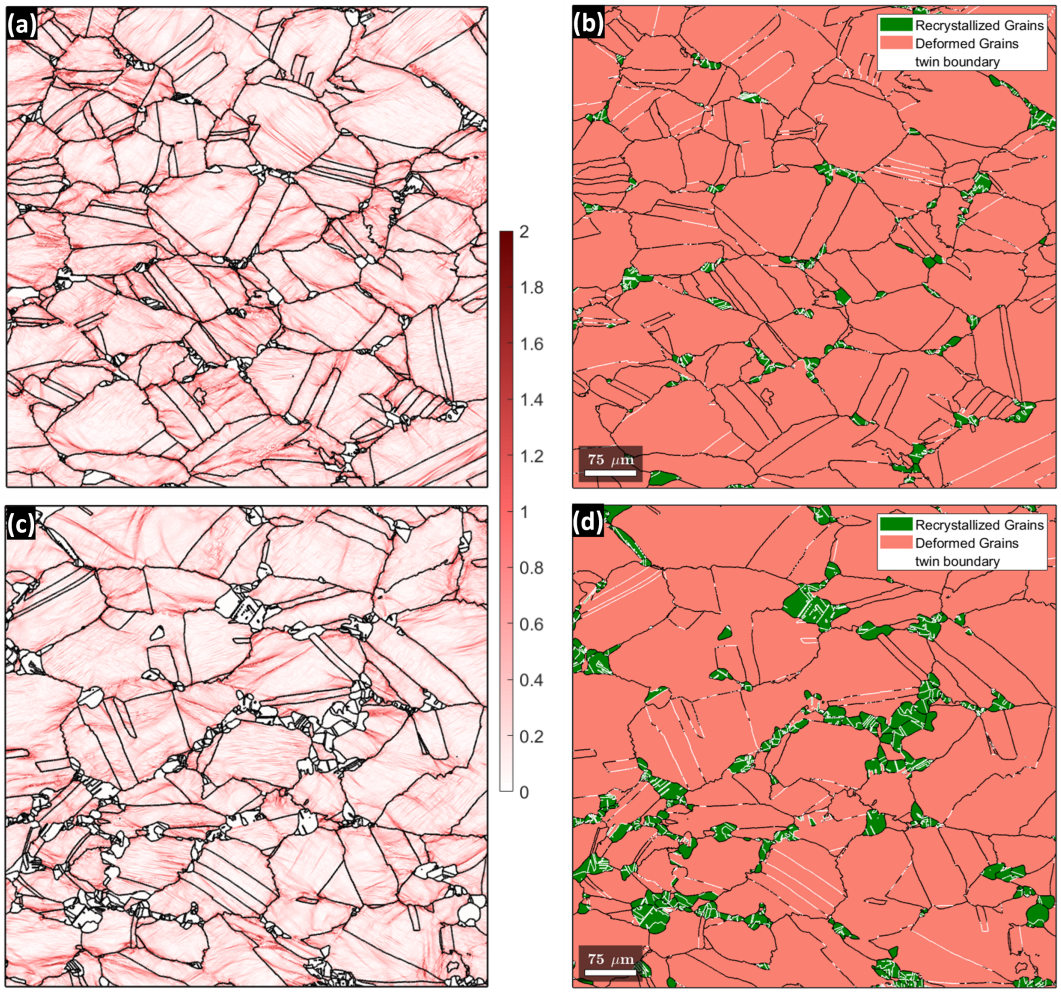

FIGURE 4.22: **Nucleation sites for 2s and 10s annealing treatment. (a) & (c) The high resolution KAM maps for 2s and 10s annealed specimen respectively, respectively. (b) & (d) Micro-graphical representation of nucleation at 2s and 10s, respectively.**

The triple junctions may comprise of different types of boundaries such as: random HAGBs, LAGBs, or former twin boundaries. In Fig.4.21(a), the bulging of the grain occurs at a triple junction consisting of two random HAGBs and one LAGB. The LAGB of such a triple junction is essentially referred to as the deformation band within a coarse-grain. The LAGB is visible in Fig.4.21(b) by the clear distinction in orientation change within the grain. The sub-grains formed at this triple junction possess an energy advantage due to the accumulated misorientations from the deformation band. Another special case of the triple junction where the nuclei has already formed is shown in Fig.4.21(c) & (d), consisting of two random HAGBs and one former twin boundary that has lost its grain boundary character. This characteristic triple junction validates the hypothesis in subsection 4.2.2, that a former twin boundary can behave as a potential nucleation site, due to the gliding of the partial dislocations. Also, the driving force available for the expansion of a former twin boundary is evident from Fig.4.21(c) . Therefore, the work conducted by Beladi et al.[19], quantifying the sigma boundaries involved in triple junctions has relevance, which is validated by the experimental results of these EBSD maps. Finally, further research is being conducted to extensively analyze the different triple junctions

present in the alloy and the quantification of these activated triple junctions during the initial phase of the annealing treatment.

The recrystallization nucleation process facilitated by the effects of recovery, leading to the formation of nuclei is displayed in Fig.4.22. In addition to the nucleation mechanism and triple junctions observed in the 1s annealed sample, Fig.4.22(a) & (b) continues to confirm that the primary and dominant nucleation site for the alloy is at the triple junctions. These triple junctions is initially favoured over the grain boundaries for nucleation, as a result of multiple collaborating factors. Firstly, highest dislocation accumulation occurs at triple junctions as observed in Fig.4.19(c), providing the necessary driving force required for bulging. Secondly, two adjacent sub-grains that have a larger size difference is known to behave as a nucleation site. However, this criterion is not necessary at triple junctions, since there is a high possibility for the accumulation of misorientations for sub-grains at triple junctions [15]. This trade-off by accumulating misorientations allows the sub-grains at triple junctions to form nuclei irrespective of their requirement to grow and produce a large size difference [15]. Finally, the main aim of the SRX phenomenon is the consumption of deformed grain boundary [11]. So, the formation of nuclei at the triple junctions allow for a quicker consumption of deformed grain boundary (since it involves three adjacent grain boundaries) in comparison to grain boundary nucleation.

The dominance of triple junctions as a nucleation site during the initial phase of the annealing treatment is gradually replaced by grain boundary nucleation at 10s of the annealing treatment, as observed in Fig.4.22 (c) & (d). Once the nuclei are initially formed at triple junctions, they either continue to grow along the adjacent grain boundary forming annealing twins within the grain, or they provide necessary driving force for new nuclei to be formed along the adjacent grain boundary. There is a competition experimentally observed between the growth of the triple junction nuclei and the new nuclei that is formed along the grain boundary. The growth of the triple junction nuclei is observed to consume the potential grain boundary nucleation sites, thereby reducing the total number of nuclei formed, and increasing the average recrystallized grain size. This competitive effect between growth of triple junction nuclei and the possibility of new nuclei along grain boundaries finally determines the nucleation rate, which is experimentally calculated and compared with physical models in the following subsections.

4.6.1.1 Calculation of Critical Size Required for Bulging

The nucleation mechanism experimentally validated above, can be further categorized as multiple sub-grain SIBM and single sub-grain SIBM. Based on the information available in the literature [15], there have been speculations between these two mechanisms for the Ni-30 Fe alloy. The multiple sub-grain SIBM mechanism requires a net driving force obtained by the difference in stored energy between two successive grains. In other words, the measurement of the dislocation density on either side of the grain boundary is essential for the calculation of the critical sub-grain size for bulging. By contrast, the single sub-grain SIBM is dependent on a well recovered sub-grain structure, and possesses the highest stored energy difference between the two grains. Single sub-grain SIBM would be mainly dependent on the sub-grain boundary energy and sub-grain size distribution. Currently, it cannot be experimentally validated based on the available EBSD scans. However, it can be

assumed that the combination of both multiple and single sub-grain SIBM is experimentally possible for the Ni-30Fe alloy, with one being slightly more dominant than the other. The dominance between the two SIBM mechanisms can be hypothesized by using Eq.2.9 for the critical size required for bulging. From this equation, the critical size for bulging according to the SIBM mechanism is dependent on: specific grain boundary energy (γ_{SE} = 0.712 J/m^2), shear modulus (G = 42 GPa), burgers vector magnitude (b = 2.48 Å), and the dislocation density difference between two grains ($\Delta\rho_{GND}$).

As already observed in the literature, the measurement of the dislocation densities on either side of a grain boundary to obtain the net driving force is complicated due to variability of the GND density throughout the specimen. So, a factor is utilised with the captured GND densities, in order to estimate the difference in dislocation densities between adjacent grain boundaries ($\Delta\rho_{GND} = 0.5\rho^*_{GND}$, where, ρ^*_{GND} is the global GND density). The literature [11] suggests 0.5 for this factor with the global dislocation density, since it is an intermediate value. The factor proximate to 1 would indicate that single sub-grain SIBM is the dominant mechanism, since the difference in dislocation density between the two grains is similar to dislocation density of the bulging grain. Fundamentally, this signifies that the grain that is bulging would contain a single sub-grain that is predominantly larger than others, and thereby composed with majority of the dislocations, whereas the adjacent grain has almost negligible dislocations. By contrast, the factor lower than 0.5 would indicate that multiple sub-grain SIBM is the dominant mechanism, since both the grains contain almost similar dislocation density, and hence the nucleation of the recrystallized grain occurs by multiple sub-grains bulging simultaneously. Initially, the factor of 0.5 is utilized in this research study for the experimentally measured GNDs in the specimen. Consequently, this would cause the critical size for bulging to be actually larger than the recrystallized average radius (obtained from grain size calculations). This would be unrealistic, since ideally the critical size for bulging(r_c) is expected to be lower, in order for the recrystallization nucleation to proceed. Furthermore, this would signify that the measured GNDs are not entirely captured with the methodology utilised. On the other hand, making the assumption that GNDs have been entirely captured and are essentially the global GND density (ρ^*_{GND}), permits us to reconsider the 0.5 factor used in the literature [11]. Therefore, we utilise a slightly higher factor of 0.75 with with experimentally measured GNDs to obtain reasonable results for the critical size for bulging, as illustrated in Fig.4.23.

By comparison with the experimentally obtained recrystallized average radius, we can confirm that the critical size for bulging is sufficiently and realistically lower during the recrystallization process when the factor selected is 0.75. So, the utilization of this factor promotes single sub-grain SIBM to be dominant, as compared to multiple sub-grain SIBM, based on the reasoning provided above. However, this hypothesis would require clarification from experimental evidence that needs to be obtained from higher resolution EBSD scans. From the modelled calculations of the critical size for bulging in Fig.4.23, recrystallization is expected to proceed from 1s of the annealing treatment until shortly after the 50s time interval. The error bars for the data points are estimated based on the dislocation density deviation and grain size calculation errors for the critical size for bulging and recrystallized average radius values, respectively. Initially at the 1s interval point, the average critical size for bulging is nearly similar to the average recrystallized radius, indicating that only the

largest sub-grains developed in the deformed microstructure would form recrystallized grains. However, as the microstructure continues to recover, the critical size for bulging becomes more distant from the recrystallized radius values, permitting more amount of nucleation to potentially occur. Nonetheless, the possibility of a higher nucleation rate at 10s is dependent on the presence of potential nucleation sites. As observed earlier, the growth of the initial triple junction nuclei (at 1s and 2s annealing treatment) could potentially lead to a decrease in nucleation rate due to consumption of nucleation sites. This could be experimentally validated with the experimental nucleation rate reported in subsection 4.6.2.

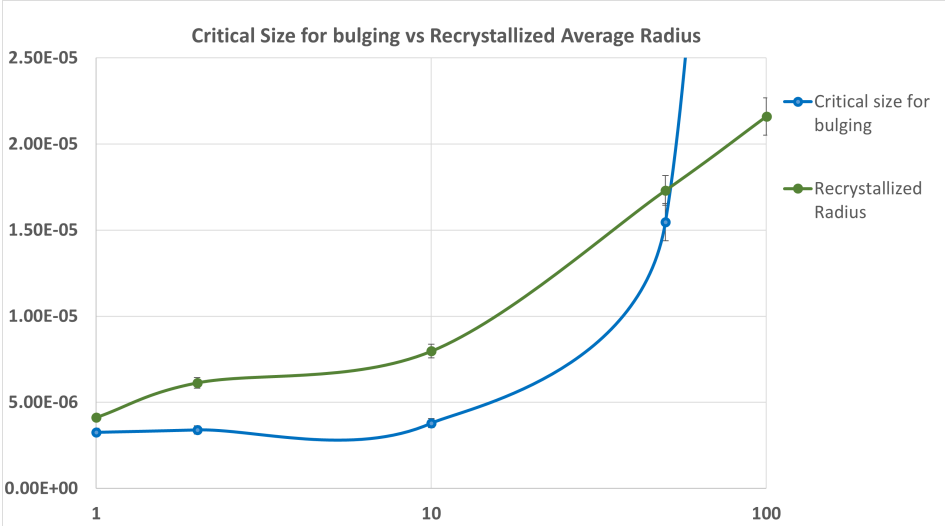

FIGURE 4.23: **Critical size required for bulging(r_c) *vs* the experimentally calculated average recrystallized radius (R_{rex})**

Shortly after the 50s annealing time interval, the critical size for bulging exceeds the experimentally obtained average recrystallized radius, which signifies that the SRX phenomenon transitions to the grain growth process. The calculation of the experimental nucleation rate is thereby also essential for validation of the predicted time interval at which the recrystallization nucleation process is completed. Finally, the exponential increase in the critical size for bulging with time is validated by the effect of recovery, which consequently reduces the deformed stored energy with time, as experimentally observed in subsection 4.5.1.1.

4.6.2 Nucleation Rate: Experimental Quantification

The formation of sub-grains through the polygonization process(rearrangement of the GND forests into LAGBs) is the essence of recrystallization nucleation at the prior HAGBs. The impingement of the sub-grain (single or multiple subgrains) on the HAGB allows migration through bulging, as shown in Fig.4.21. Finally, the new recrystallized grains emerged at nucleation sites that contained deformation heterogeneity as measured by the KAM value, the GND density and the corresponding stored energy. The quantification of the recrystallization process associated with the observed nucleation mechanism, has been shown in Fig.4.24. The calculated experimental nucleation rate is not a constant parameter since the classical nucleation theory is irrelevant for the SRX phenomenon, as explained in the literature [15]. The driving force for recrystallization nucleation which is dependent on the deformed

stored energy is much lower than solid state reactions [15]. Therefore, nuclei begin to form even at initial stages of the deformed microstructure, during the recovery phase itself. This has been experimentally observed by presence of nuclei at 1s of the annealing treatment, as shown in Fig.4.21.

Additionally, with the results reported in subsection 4.4.1 & 4.6.1.1, the experimental nucleation rate during the annealing treatment can be quantified for the different regions of the specimen (shown in Fig.4.24). The recrystallized grains are highly dependent on the separation technique and time of observation as described earlier. The nucleation rate is estimated using Eq.2.7, where the increment of the recrystallized grains(using GAM technique) for an incremental observed time interval is calculated for 1mm^2 specimen area. This methodology has been incorporated separately for the three different regions of the specimen: upper, central and lower. The experimental error for the nucleation rate has been estimated by the standard deviation for each data point.

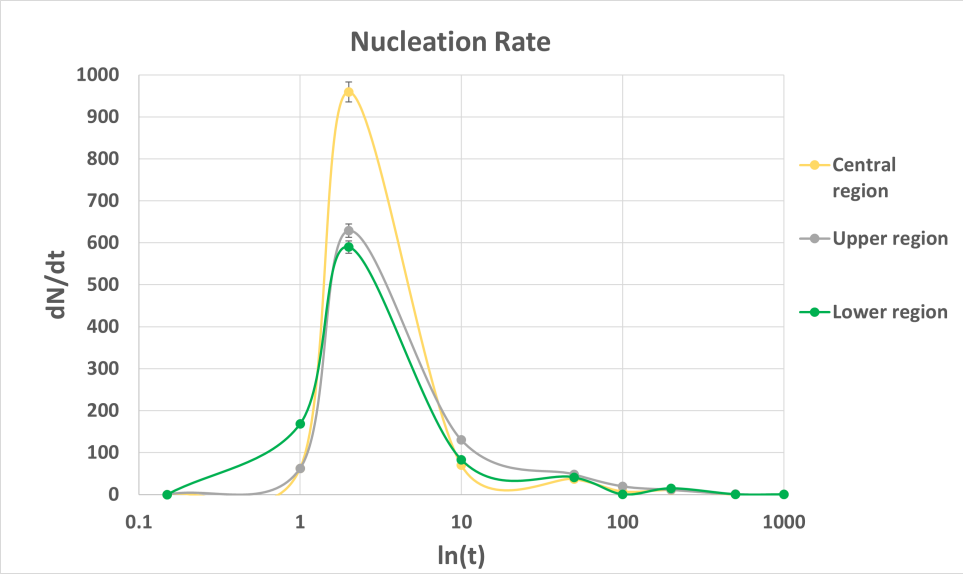

FIGURE 4.24: **Experimental Nucleation rate estimated during the annealing treatment for the three different regions of the specimen**

The nucleation rate estimated at 1s for the lower region of the annealed specimen is maximum, confirming the results from subsection 4.4.1. The similar trend which is observed at 2s for the central region of the annealed specimen, is further substantiated by observing Fig.4.25. The reason for different regions of the specimen behaving differently in terms of the nucleation rate, during the initial phase of the annealing treatment, is dependent on the number of potential nucleation sites and the distribution of deformation heterogeneity throughout the specimen. The transformation in nucleation rate from lowest to highest between 1s and 2s, for the central region of the specimen is an indication of the change in local deformation accumulation after the uniaxial compression test. Initially, when the specimen is uniaxially compressed, the ends of the specimen would consist of maximum deformation, which is experimentally validated by the GND density measurement. As the sample is further annealed, the accumulated deformation is maximum at the centre of the specimen (shown in Appendix section A.3), providing a maximum nucleation rate of 960 recrystallized grains mm^{-2} s^{-1}, at 2s of the annealing treatment.

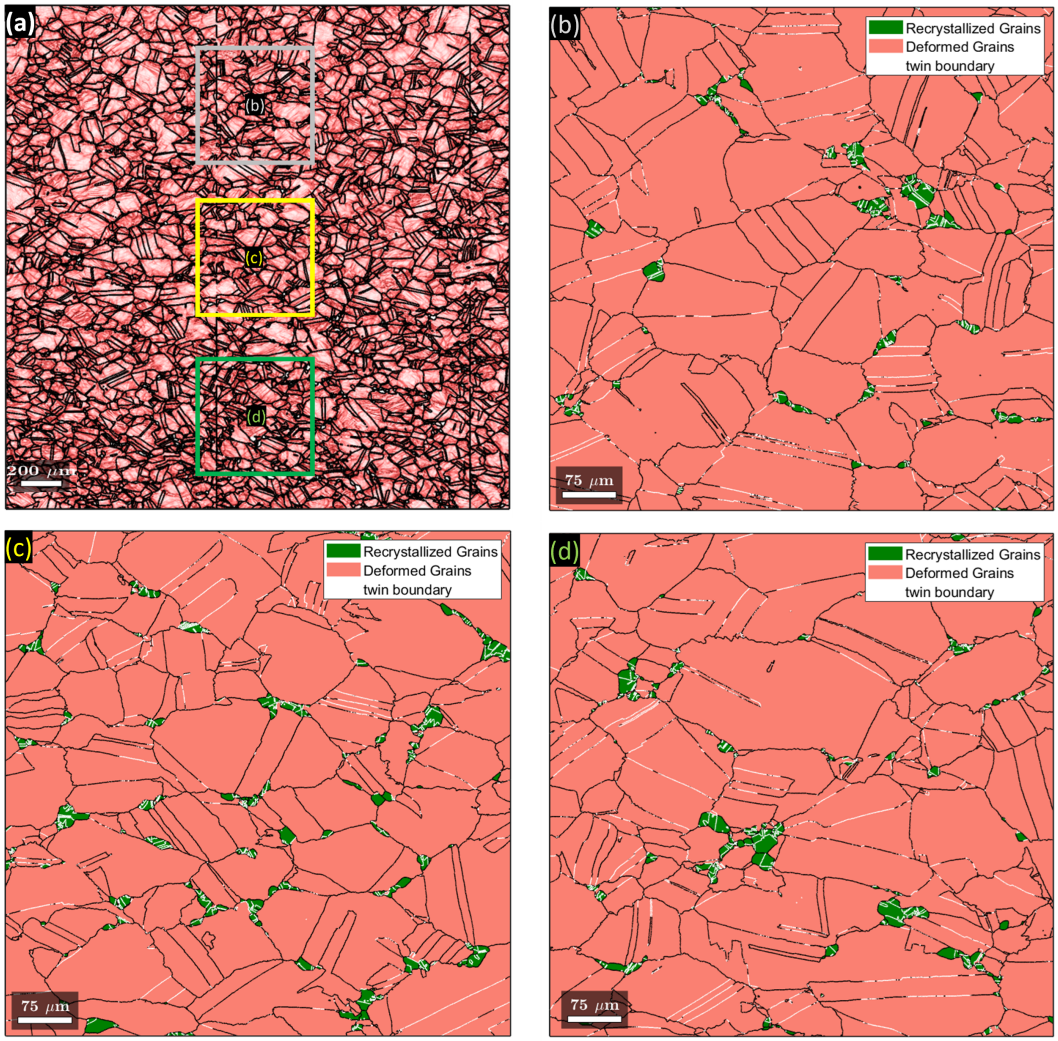

FIGURE 4.25: **Recrystallization Nucleation for 2s annealed specimen. (a) KAM map for the low resolution EBSD scan indicating the upper, central and lower regions of the specimen. (b), (c) & (d) Corresponding recrystallization nucleation representation of the upper, central and lower regions, respectively.**

An alternative explanation for the difference in nucleation rate physically observed in Fig.4.25 can be accounted for by the growth of the triple junction nuclei initially formed after deformation. These triple junction nuclei formed at the upper and lower regions of the specimen continue to grow because of the presence of higher driving force. This consequently leads to the consumption of nucleation sites which causes the observable decrease in nucleation rate at 2s, in comparison to the central region. Fig.4.25 (c) confirms that the average recrystallized grain size for the central region is lower than the other two regions of the specimen at 2s of the annealing treatment.

There is an overall drop in the nucleation rate after 2s of the annealing treatment. Despite the low critical size for bulging required at 10s, as observed in Fig.4.23, where the nucleation rate is almost similar to that of 1s, which confirms that majority of the nucleation sites have been consumed by this point in the annealing treatment. Therefore, the driving force present at grain boundaries allows the growth of the

triple junction nuclei at a very early stage in the annealing treatment. Nevertheless, even with the consumption of majority of the nucleation sites at 10s, the nucleation rate is not observed to reach zero until after 100s of the annealing treatment. This phenomenon explains that nucleation continues until site saturation is attained, and all GNDs are annealed out of the specimen. The presence of deformation at 100s of the annealed sample can be observed by the GAM technique in Fig.4.9(e), validating that there are local concentrations of GNDs that are present at 100s (also seen in Fig.4.19(i)). Additionally, the prolonged nucleation process observed until 100s could also be a result of the annealing twins being formed in order to reduce the interfacial energies of the microstructure.

4.6.3 Nucleation Model: Predicted 3D Experimental Nucleation Rate and Comparison with the Physical Model

The literature [8] suggests that the conversion of results from 2D to 3D for the SRX phenomenon is currently more accurate, as opposed to using the 3D measurement methods, since the alloy is opaque, it provides no direct way of examining the actual volume distributions of grains within the specimen. Therefore, this research study incorporates the new stereological procedure based on the Saltikov technique. It is observed counter-intuitively and mathematically by taking different class sections[8] that the 2D distribution of grains underestimates the experimental grain size calculations in a 3D microstructure. Essentially, if the grains sizes are expected to be larger in a 3D model, the number of grains present in $1mm^3$ will be smaller than the 2D model. So, a nucleation rate relation from 2D to 3D can be approximated by using a conversion factor, $c_1 = 0.799$ [8]. Finally, the nucleation rate that has been calculated separately for 3 different regions in the previous subsection, is averaged for a $1mm^2$ area distribution, and consequently estimated in 3D for $1mm^3$ volume distribution. The results from this approximation have been shown above in Fig.4.26.

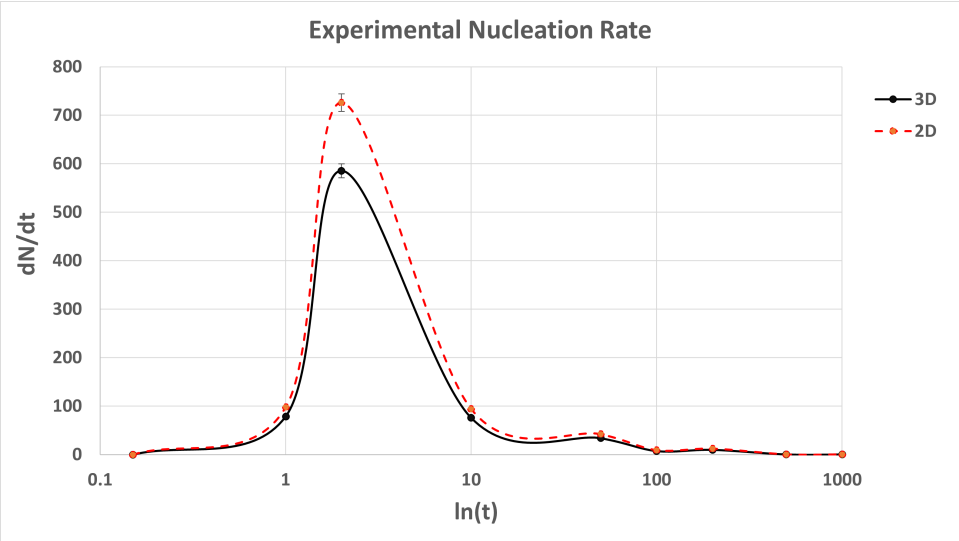

FIGURE 4.26: **Estimated experimental nucleation rate in 3D**

The concept of recrystallization nucleation is found to be essential for predicting the SRX phenomenon and the recrystallization kinetics. The literature suggests that the nucleation rate can be predicted by 4 main parameters as seen in Eq.2.13. Firstly, the fraction of sub-grains that can form viable nuclei based on the critical size for bulging

is calculated and denoted by *df/dt*, which is an analytical value. Secondly, the number of potential nuclei developing is estimated by the deformed grain boundary area per unit volume (S_v with units: m^{-1}), divided by the area of a viable nucleus (A_{nucl} with units: m^{-2}). The deformed grain boundary area is calculated using Eq.2.14 and the area of a viable nucleus is estimated using the area of a circle with the radius of the critical size for bulging (considering the grains are spherical in shape). Then, the last defining parameter which is the unrecrystallized fraction ($F_n[t]$) has been initially predicted from Eq.2.15, but is not utilized in this research study as it predicts that the non-recrystallized fraction increases with time, which is contradictory since the ($F_n[t]$) is expected to reach zero at the end of the recrystallization process. So, the unrecrystallized fraction($F_n[t]$) in this research study has been experimentally estimated for the different time intervals using the recrystallization fractions obtained from the validated GAM technique. These defined parameters for the nucleation rate model has been reported in Table.4.1 for the different time intervals of the annealing treatment. Finally, the predicted values of the nucleation rate using the above described model, are converted from number of recrystallized grains in S.I units to $mm^{-3}s^{-1}$, in order to compare with the experimental nucleation rate in 3D.

Annealing Time (s)	df/dt	A_{nucl} (m^2)	S_v (m^{-1})	$F_n[t]$(%)	dN/dt ($m^{-3}s^{-1}$)	dN/dt ($mm^{-3}s^{-1}$)
1	1.999988373	1.72143E-10	45362.30964	99.76%	5.26E+14	5.26E+05
2	3.999952363	4.51482E-11	45362.30964	97.13%	3.90E+15	3.90E+06
10	19.97571128	7.52073E-10	45362.30964	89.28%	1.08E+15	1.08E+06
50	78.22827588	4.91297E-08	45362.30964	34.91%	2.52E+13	2.52E+04
100	66.82725934	6.12023E-08	45362.30964	2.64%	1.31E+12	1.31E+03
200	2.319521621	8.44296E-08	45362.30964	0.41%	5.09E+09	5.09E+00
500	6.19768E-14	1.13496E-07	45362.30964	0.04%	9.91E-06	9.91E-15
1000	2.91562E-66	1.27953E-07	45362.30964	0.02%	1.98E-58	1.98E-67

TABLE 4.1: Parameters incorporated to calculate the predicted nucleation rate using Rehman's model

The predicted nucleation rate values from the last column in Table.4.1 have been plotted in Fig.4.27 for the different time intervals, which can be compared with the experimental 3D nucleation rate in Fig.4.26. Despite the similar trend in the nucleation rate peak between the experimental and physical model, there is a large discrepancy in terms of the quantity of nuclei formed at every stage of the annealing treatment. The discrepancy is approximately of the order $0.6x10^4$ number of nuclei $mm^{-3}s^{-1}$ greater with the physical model at the peak of the nucleation process. The reason for this discrepancy between the experimental and predicted results have been proposed below:

- The statistical distribution and fraction of sub-grains that achieve the average critical size for bulging has to be altered, since the nuclei is observed to form by the gradual consumption of the deformed-area available based on sub-grains larger than the critical size. Currently, the model assumes that nearly the entire sub-grain fraction forms nuclei for the initial 10s of the annealing treatment,

which is unrealistic based on the proposed SIBM nucleation mechanism. Ideally, the smaller sub-grains would be consumed by these large sub-grains that bulge along a boundary to form a recrystallized grain.

- Furthermore, the contradictory behaviour of the modelled non recrystallization fraction in the polycrystalline material assumes the volume of the recrystallized grains to be a spherically shaped shell with an initial deformed grain radius. Ideally, as seen in the EBSD maps of the alloy, the experimental results indicate that the deformed grains are elongated and pancake shape. Hence, the deformed grain shape could potentially have an influence on the non-recrystallized fraction in the material.

- The recrystallization process observed experimental growth of the nuclei instantly after development. This has been typically observed for the initial triple junction nuclei that grow between 2s and 10s annealing time. On doing so, the other potential nucleation sites along the boundary are consumed, reducing the outcome of the nucleation rate. However, in the current model, the growth of the nuclei is predicted only after site saturation and consumption of all the nucleation sites occurs, which is unrealistic. This impracticality is observed in the model by the continuously high nucleation rate even after 10s of the annealing treatment.

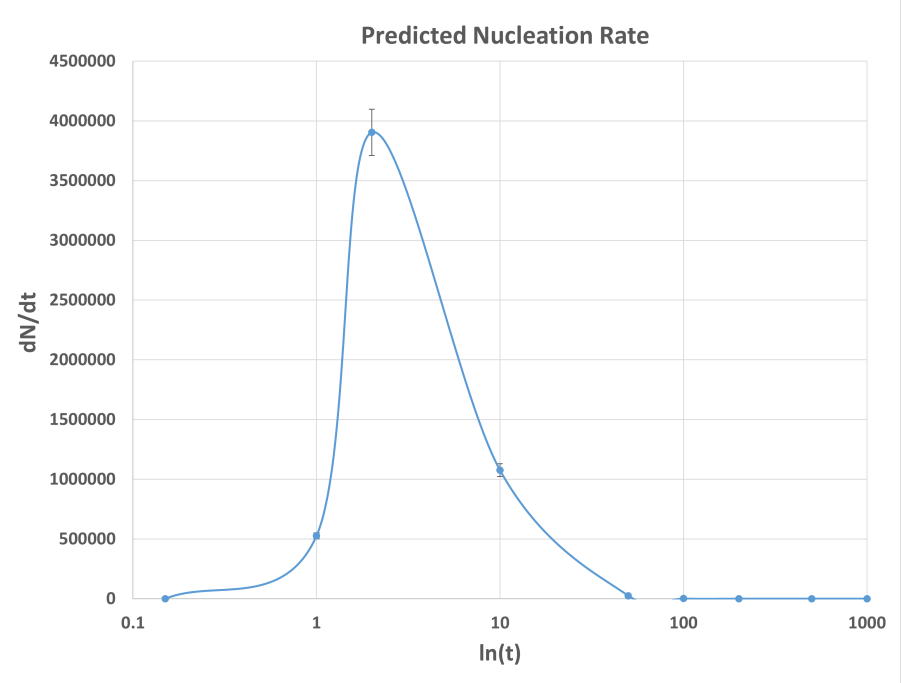

FIGURE 4.27: **Predicted nucleation modelling in 3D using the physical equations from Rehman's model**

- Additionally, the predicted nucleation model by Rehman et al. [11] estimates the parameters for the nucleation rate by only considering a single grain. However, in the experiments, a polycrystalline material with much larger scanned regions are considered, in order to obtain accurate and deterministic values. Therefore, the attempt by Rehman et al. [11] to reproduce the SRX behaviour

of a polycrystalline material through a single representative grain could be an excessive approximation, as observed by the large deviation.

In conclusion to this section, the dominant nucleation mechanism has been proposed to occur by single sub-grain SIBM since the Δ factor, 0.75 is selected for the calculation of the critical size for bulging. However, this is an approximation of the difference in dislocation densities between grain boundaries and can deviate for different grains. Nevertheless, the nucleation rate has been experimentally calculated and estimated for a 3D microstructure. Additionally, the large discrepancies between the predicted physical model and the experimentally calculated nucleation rate is discussed in detail. Finally, with the experimental nucleation rate results, the recrystallization kinetics can be estimated and compared with models/empirical relationships, as shown in the section below.

4.7 Recrystallization Kinetics

Initially, a specific value of softening ratio for estimating the start of recrystallization is not completely appropriate, since the softening ratio deviates largely based on the deformation conditions. Therefore, it is important to incorporate an incubation time into the model for the quantitative onset of the SRX phenomenon, as done in subsection 4.7.1. The development of the nuclei based on the nucleation rate calculated from the previous section is estimated to grow linearly at a constant growth rate. As the recrystallized grains begin to impinge one another due to site saturation, the nucleation rate decreases tremendously and the recrystallization fraction (X_{re}) approaches 1. This has been experimentally observed and validated in subsection 4.7.3 by the experimental recrystallization kinetics, incorporated from the recrystallization fractions of the GAM technique. The experimentally estimated recrystallization kinetics can be further compared with the JMAK model in the literature, since this model assumes nucleation sites to be randomly distributed. The recrystallization kinetics is also estimated with the empirical relationship of the Speich-Fisher(SF) equation as determined in the literature research. Finally the experimental recrystallization kinetics of the Ni-30 Fe alloy is also discussed with these available models, using the calculations of the Avrami constant(n) and the SF constant (m), shown in subsection 4.7.2.

4.7.1 Incubation Time and recovery

After the deformation of the alloy, the amount of deformation reaches its maximum, as observed by the dislocation densities at 0.15s time interval. Consequently, annihilation of dislocations is experimentally observed for the whole sample after the 1s annealing treatment, as shown in subsection 4.5.1.1. The static recovery process can therefore be described with the results of the stored energy as a function of time. At 1s of the annealing treatment, recrystallization nucleation has been experimentally observed by the SIBM mechanism, shown in subsection 4.6.1. This time period of approximately 1s can be considered as the incubation time (τ), where the onset of SRX as a result of the static recovery. Therefore, the JMAK model can accommodate for this incubation time by altering Eq.2.17 from the literature, by using the Eq.4.2 illustrated below. It is important to note however that the static recovery process still continues slightly after the incubation time, and overlaps with the recrystallization process, until the dislocation arrangement within the sub-grains is completed.

$$X_{re} = 1 - exp[-K(t-\tau)^n] \tag{4.2}$$

The thermally activated rate constant, *K*,that represents the nucleation and growth rate can be estimated by using the intercepts of the ln[-ln(1-X_{re})] with ln(t) graph. The Avrami constant, *n* is correspondingly calculated by calculating the slope from this graph, as shown in Fig.4.28. The incubation time, τ, that has been experimentally observed, is mathematically modelled and validated using the Eq.4.3 [14], shown below.

$$\tau = \tau_0 \, D_0^{m_\tau} \, \dot{\epsilon}^{n_\tau} \, \epsilon^{l_\tau} \, exp(\frac{Q_\tau}{RT}) \tag{4.3}$$

The parameters τ_0, m_τ, n_τ, l_τ, are constants that have been reported in the Appendix section A.5. The apparent activation energy, Q_τ, is assumed for a low carbon steel. The deformation conditions in this research study are at an annealing temperature of 900°C, strain(ϵ) of 0.2, and a strain rate($\dot{\epsilon}$) of $1s^{-1}$. Additionally, the grain size before deformation(D_0) has been experimentally reported earlier as approximately 101.50μm. Finally, the incubation time estimated from Eq.4.3 is approximately 0.9s, which is in good agreement with the experimentally determined incubation time. Therefore, the incubation time takes into account the time period where SRX nucleation does not occur after deformation, and assists in disregarding nuclei that may have dynamically formed during deformation.

4.7.2 Avrami constant and SF constant

The recrystallization fractions have been accurately determined by the GAM technique, as shown in subsection 4.3.4. The JMAK model and the empirical relationship of the SF equation has been described from the literature using Eq.2.18 and Eq.2.19, respectively. Similar to Avrami constant, *n*, described above, the SF equation is denoted by a constant, *m*, to indicate the transformation process during the annealing treatment. After incorporating the experimental recrystallization fractions obtained during the annealing treatment, the logarithmic of the JMAK and SF equation is plotted with the logarithmic of time. Calculating the slope from Fig.4.28(a) and (b), the transformation constants can be estimated for the JMAK and SF equation, respectively. It has been observed that the constants, *n* and *m* have a similar trend for the different processes of the annealing treatment. The initial phase, shown in orange, indicates the recovery process fitted by three data points at 1s, 2s and 5s of the annealing treatment. Since recrystallization nucleation begins at approximately 1s, the recovery process overlaps with recrystallization process. However, the prominent consumption of the unrecrystallized fraction is observed from 10s of the annealing treatment. So, the recrystallization process is shown in blue and fitted by three data points at 10s, 50s and 100s. Finally, the SRX phenomenon concludes with the grain growth process, shown in green and fitted by three data points at 200s, 500s and 1000s.

The larger *n* and *m* values, 2.33 and 2.56, respectively, that have been initially obtained during recovery, occurs due to the exclusion of the incubation time in the respective equations (Eq.2.18 and Eq.2.19). By contrast, the values of *n* and *m* that have been obtained from the 10s time interval onward is of lower values, since it is not highly dependent on the incubation time, and hence can be considered as the accurate constant values for both the equations (Eq.2.18 and Eq.2.19).The Avrami constant(n) obtained experimentally from the recrystallization kinetics is observed

to be 1.37, which is in good agreement with the expected value in the literature to be between 1 and 2 [11]. Additionally, the m values from the SF equations is constantly observed to be higher than the Avrami constant, which is in good agreement with earlier work conducted for a low carbon ferritic steel [28]. Finally, the n and m values, 0.52 and 0.62, respectively, during the grain growth process is of a much smaller value as compared to the recrystallization process, which confirms the decline and stagnation of the recrystallization kinetics. The inference from the small transformational constant values for the JMAK model and SF equation during the grain growth process, indicates that it is no longer relevant once site saturation is achieved within the microstructure.

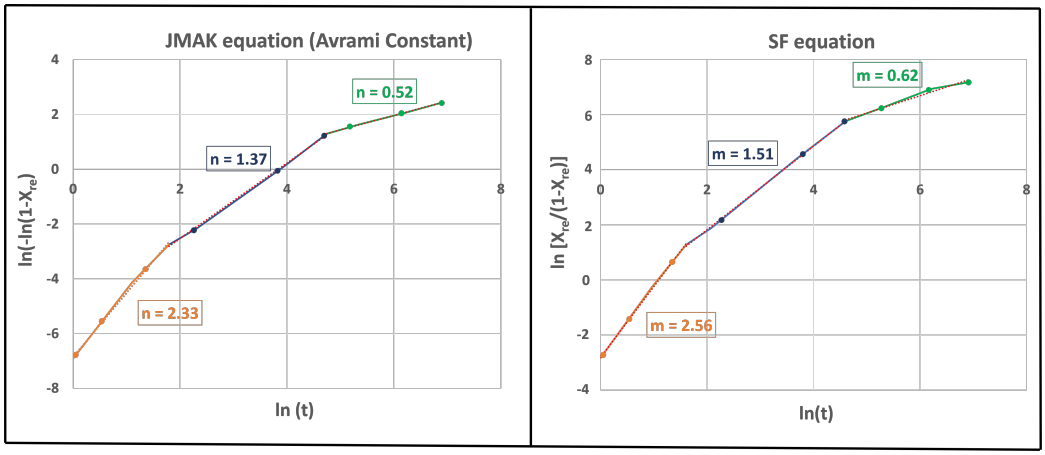

FIGURE 4.28: **(a) Avrami constant from the JMAK model duing recovery, recrystallization and grain growth process. (b)SF equation constant during recovery, recrystallization and grain growth**

4.7.3 SRX Kinetics Comparison: Experimental, JMAK model and Empirical relationship

The transformational constants (estimated from the subsection 4.7.2) during the recovery, recrystallization and grain growth processes for the JMAK and SF equations, can be utilized to obtain the recrystallization kinetics curve for the annealing treatment. The experimental results obtained with the original GAM technique in subsection 4.3.4, has been compared with the JMAK model and the SF equation as shown in Fig.4.29. The expected sigmoidal pattern for the experimental recrystallization kinetics has been validated by the fitting conducted with the JMAK model. However, the JMAK model predicts recrystallization to begin before the proposed incubation time and this behaviour occurs since the equation does not incorporate the incubation time. Nevertheless, the JMAK model fitted for the recovery phase of the annealing treatment is in agreement with the experimental results.

The fitting of the SF equation predicts nucleation to begin and progress slower than the experimental kinetics during the initial phase of the annealing treatment, as seen in Fig.4.29. However, after the recovery process, the experimental results are observed to be in agreement with the SF equation, unlike the JMAK model which observes a larger deviation towards the end of the recrystallization process. This deviation which leads to slower kinetics with the JMAK model is potentially due to the disregarded experimental growth of nuclei before site saturation occurs. The experimental growth of nuclei can be comprehended by the reduced nucleation rate

after 2s of the annealing treatment, as seen in Fig.4.24. Despite the small critical subgrain size required for bulging at 10s (shown in Fig.4.23), the observed experimental nucleation rate is comparatively low at 10s, which can be accounted for the experimental growth of nuclei occurring after 2s of the annealing treatment. Finally, the site saturation ultimately results in the drastic decrease in Avrami constant, as observed during the grain growth process. The deviation in the JMAK model during the latter recrystallization and grain growth processes is consistent with the previous study [60], which states that the JMAK model is not valid after 70% of the recrystallization fraction. Additionally the deviation in the current experimental results with the JMAK model, around the 50s time interval can also be attributed to the experimental deviation error in stress during deformation of the specimen. By contrast, the SF equation is found to be in better agreement with the experimental results during the grain growth process, which is consistent with the previous research work conducted [28].

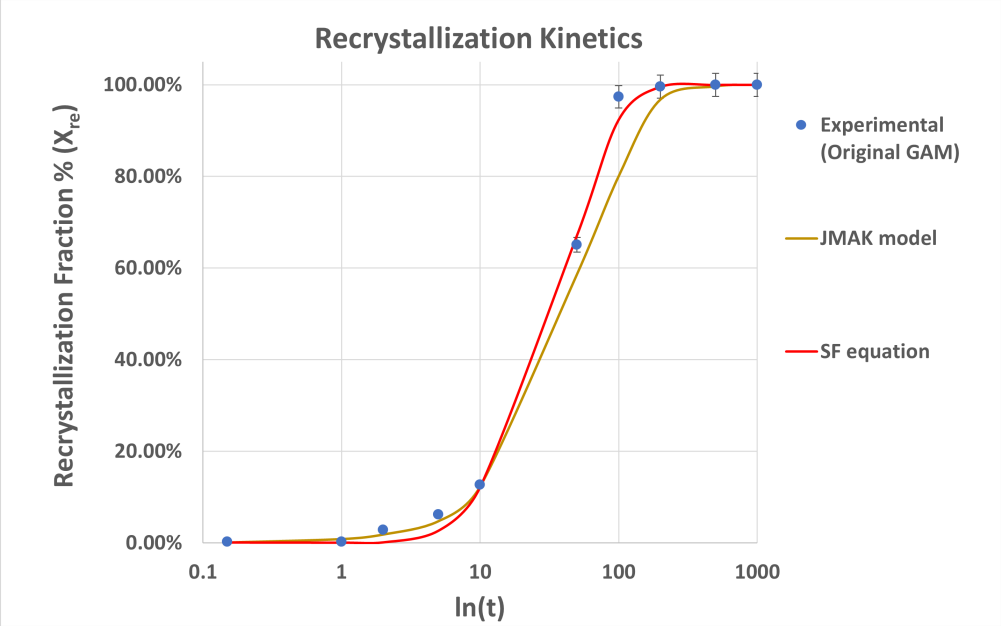

FIGURE 4.29: **Recrystallization Kinetics of the experimental results using original GAM. The fitting of the JMAK model and SF equation is conducted using the results from Fig.4.28**

In conclusion to the section, the experimental results have been validated by comparison with the commonly used JMAK model and the empirical relationship of the SF equation. The importance of the incubation time has been illustrated by the inaccuracies in the JMAK model after deformation of the specimen. The recrystallization kinetics that have been obtained for the modelled Ni-30 Fe alloy is assumed to similarly occur for the C-Mn steel. However, the recrystallization kinetics behaviour reported in this study must not be generalized, since it is further dependent on the initial grain size, temperature, deformation mode, material composition and grain boundary energy.

Chapter 5

Conclusion and Recommendation

5.1 Conclusions

The experimental research study for the SRX phenomenon of austenite after initial deformation of a Ni-30Fe alloy produced the following results:

- The development of annealing twins and LAGB regions within the recrystallized grains dismisses the merged GOS technique since it calculates the average of the misorientation angles from the merged grain mean orientation. By contrast, the merged GAM technique calculates the average misorientation angles with respect to its second nearest neighbouring pixels within a grain, thereby providing the expected sigmoidal pattern for the recrystallization kinetics.

- The function that merges grains that consists of a common twin boundary between, obtains the merged GAM values for an overall grain by potentially merging both recrystallized and deformed regions, producing slightly slower recrystallization kinetics for the merged GAM technique. By contrast, the similarity in the original GAM technique observed with the estimation of recrystallized grains and fractions using the GND density procedure, validates the GAM recrystallization separation method for the estimation of the recrystallization kinetics.

- The initial average grain size, D_0, is 101.50 $\pm$ 2.53 μm on consideration of the annealing twins by the merging grain function. The final grain size after the annealing treatment (1000s annealed specimen) has an average recrystallized grain size of 58.18 $\pm$ 1.45 μm, which is in good agreement with the predicted value of 56.92μm according to Sellars model.

- Initially, the stored energy after deformation quantified from the DLE method as 6.26x10^5 J/m^3, which declines to 5.56x10^5 J/m^3 after the nucleation and growth processes, thereby capturing the effect of recovery and recrystallization. The GNDs used to measure the stored energy are estimated to possess an error of 13% based on the curvature tensor approach. Additionally, the slightly higher estimation of the stored energy using the DLE method in comparison to the approximation method is due to the complexity involved in calculation of the average Poisson's function, which uses the average of the edge and screw dislocation systems of the FCC material.

- The incubation time estimated from the physical equation is approximately 0.9s, which is in good agreement with the experimentally determined incubation time of 1s. Initially, during recovery the Avrami constant and SF equation constant is much larger than expected due to the exclusion of the incubation

time in the modelling. The bulging of the HAGBs is observed experimentally after deformation, validating that the primary mechanism for the recrystallization nucleation is by SIBM. This mechanism is observed to occur primarily at triple junctions in the initial phase (1s and 2s) of the annealing treatment.

- The nucleation criteria is predicted in this study using the minimum critical sub-grain size required for bulging from Rehman's model. By consideration that all the GND's have been captured with the curvature tensor approach, 0.75 is the ideal factor for the global GND density (ρ^*_{GND}), in order to estimate the difference in dislocation densities ($\Delta\rho_{GND}$) between two grains. This factor that has been adopted promotes single sub-grain SIBM to be dominant (as compared to multiple sub-grain SIBM), since factor values proximate to 1 assumes higher driving force for a large single recovered sub-grain at the bulge.

- Initially at 1s, the central region possesses the lowest nucleation rate of 62 recrystallized grains $mm^{-2}s^{-1}$, whereas the lower region possesses the highest nucleation rate of 168 recrystallized grains $mm^{-2}s^{-1}$. Thereafter at 2s, the central region produced the highest nucleation rate of 960 recrystallized grains $mm^{-2}s^{-1}$, as compared to the other two regions with approximately 600 recrystallized grains $mm^{-2}s^{-1}$. The transformation in nucleation rate from minimum to maximum between 1s and 2s, for the central region of the specimen is an indication of the change in local deformation accumulation after the uniaxial compression test.

- Despite the low critical size for bulging required at 10s, the experimental nucleation rate is almost similar to that of 1s, which confirms that majority of the nucleation sites have been consumed by this point in the annealing treatment. Therefore, there is sufficient driving force that allows the growth of the triple junction recrystallized nuclei at a very early stage in the annealing treatment.

- The static recovery in the specimen which allows the annihilation of dislocations, can be observed by the difference in GND densities (approximately of the order $10^1 m^{-2}$) between the deformed and recrystallized grains. The nucleation rate is not observed to reach zero until after 100s of the annealing treatment, when the whole sample possesses the GND density as that of the recrystallized grains. This phenomenon explains that recrystallization nucleation continues until site saturation is attained, and all GNDs are annealed out of the specimen.

- The discrepancy between the predicted and experimental nucleation rate is approximately of the order $0.6x10^4$ nuclei $mm^{-3}s^{-1}$, thereby providing an inference that the nucleation modelling approach from the literature is unsuitable for this research study.

- The Avrami constant obtained during recrystallization is experimentally calculated to be 1.37, which is in good agreement with the expected value in the literature to be between 1 and 2. Additionally, the m values from the SF equation is constantly observed to be higher than the Avrami constant, which is in good agreement with earlier work conducted for a low carbon steel. Finally, the small transformational constant values for the JMAK model during the grain growth process, indicates that it is no longer relevant due to experimental growth of nuclei before site saturation is obtained.

5.2 Recommendations

The recommendations for further investigations that would assist in this research field are as follows:

- For future research it is essential to carefully categorize annealing twins separately as recrystallization twins and grain growth twins, as it would accurately depict the different stages of the SRX phenomenon. Additionally, inaccuracies in the identification of twin boundaries can be avoided by further investigation of the boundary plane.
- Further investigation can be conducted to extensively study the recovery process by utilizing the modified version of Friedel's model in the literature [58]. The driving force for nucleation can be estimated using the sub-grain size and sub-grain boundary energy by obtaining a high resolution EBSD scan in the order of 100nm. This EBSD scan will also be crucial to validate the single sub-grain SIBM hypothesis for the Ni-30Fe alloy.
- The consumption of the nucleation sites by growth of initial nuclei at an early stage of the annealing treatment will prove detrimental for the modelling of the SRX process in the Ni-30Fe alloy. Additionally, further investigation and alterations is required to estimate the fraction of sub-grains that positively influence the bulging of the grain. Finally, the estimation of the non-recrystallization fraction from the nucleation model must be further investigated.
- Further investigation to analyze the grain growth process based on the mobility of the HAGBs is essential to fully model the SRX process. Cahn's solute drag model [61] can be used to capture the mobility of the HAGBs, which is dependent on the solute concentration and temperature. Additionally, calculation of the grain growth rate would be of interest for the grain growth kinetics.
- Texture evolution analysis can be conducted to examine whether there is the retainment of deformation orientations confirmed by Beladi et al[10], or texture modifications that occur due to the recrystallization twins($\Sigma 3$ orientation relationship with the nucleus), as shown by Haase et al.[45].

Appendix A

Appendix

A.1 Recrystallization Separation: GAM Histogram

The determination of the cut-off value for the GAM technique follows the similar procedure used to predict the GOS cut-off value (shown in subsection4.3.1). The GAM histogram generated from the 10s annealed sample as seen in Fig.A.1 is an example of finding the separation point between the recrystallized and deformed grains, by observing a cut-off point. The cut-off value found from these results are 0.25°, which is utilized for the quantification of recrystallized and deformed grains.

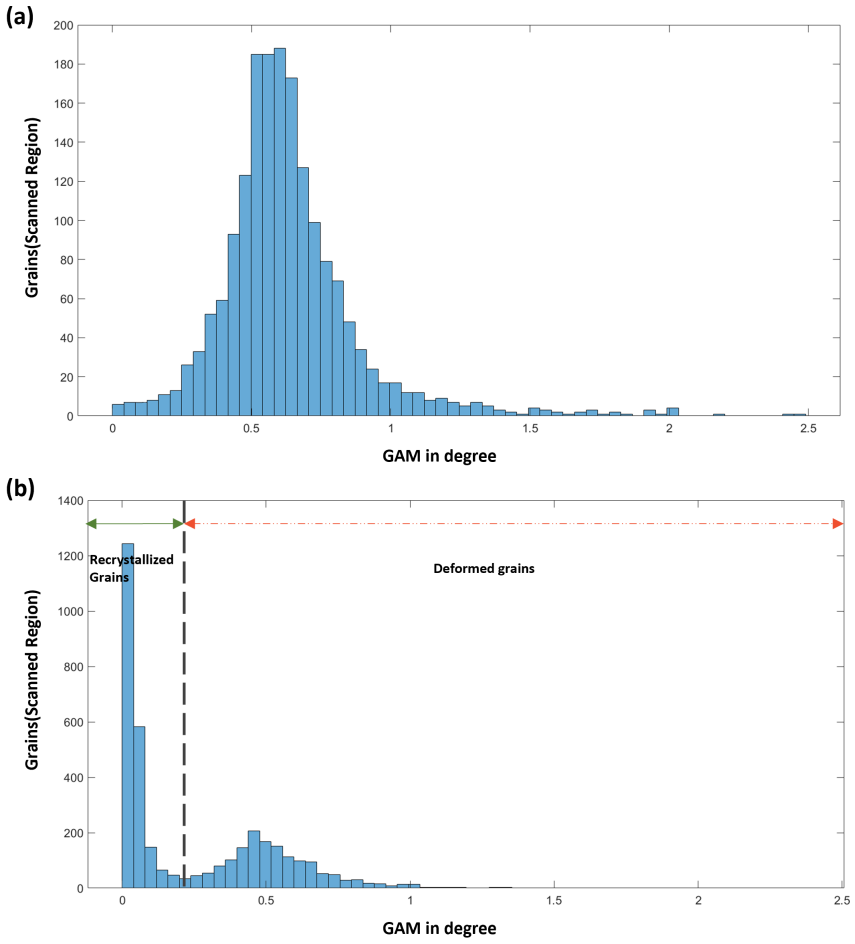

FIGURE A.1: **GAM histogram for the low resolution scanned regions, (a) After deformation and; (b) 10s annealing time**

A.2 Unrecrystallized grain Size: Without merging

The grain size calculations reported in subsection 4.4.2 consider the twins present within the grain. The merging function used for the deformed grains is not completely accurate since the former twin boundaries lose their grain boundary character after deformation. Therefore, the grain size measured without merging for the EBSD scan before deformation is observed to be 50.75 μm. This estimated initial grain-size value is approximately half the grain size measured with the merging function. Finally, this factor of 2 is more useful to comprehend the consumption of the deformed grain boundary by a reasonable and gradual decrease in the average grain size during recovery and recrystallizaion, rather than estimating the deformed grain size directly from the merged function. The values from Table A.1 is utilized to calculate the corrected unrecrystallized grain size after deformation, shown in Fig.4.16.

Annealing Time(s)	Unrecrystallized Grain Size (μm)
0	50.75
1	49.33
2	44.29
5	40.99
10	38.21
50	27.50
100	12.50
200	6.46
500	4.13
1000	3.35

TABLE A.1: Unrecrystallized grain size calculations without merging of grains

A.3 GND Density for different regions

Fig.A.2 depicts results for each region of the specimen, which has been averaged and plotted in section 4.5.1.1, in order to show the effect of recovery and recrystallization for the deformed Ni-30Fe alloy. During the initial phase of the annealing treatment, the GND density for the three regions of the specimen varies largely, as compared to the GND densities once the specimen is recovered(10s annealing time interval). This phenomenon of larger deviation in GND density between the upper, central and lower regions validates the movement of local deformation. Initially, once the

specimen is deformed, it is observed that the lower region of the specimen experiences maximum GND density providing deformation accumulation. However, at 2s of the annealing treatment the local deformation shifts to the central region of the specimen, providing a maximum GND density for the deformed region. Finally, towards the end of the annealing treatment, there are deviations observed in the GND desnity for the deformed regions. This arises as a result of experimental errors due to the presence of small unrecrystallized grains, where the grain average misorientation cannot be estimated due to the absence of second nearest neighbours within an unrecrystallized grain.

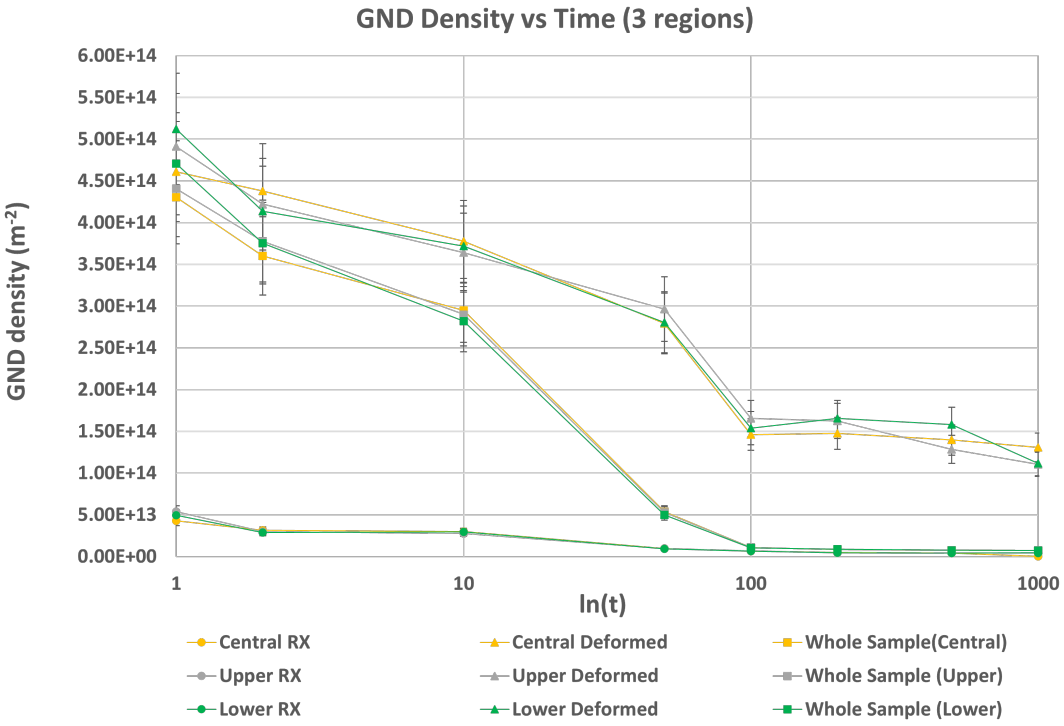

FIGURE A.2: **GND density at different annealing periods for the upper(grey line), central(yellow line) and lower(green line) region of the specimen. The GND density is depicted separately for the recrystallized(Circular marker), deformed(Triangular marker) and whole scanned region(Square marker)**

A.4 Stored Energy during the annealing treatment

The results for the stored energy as a function of time is reported in this section, which follows the similar trend as the GND density. The continuous decrease in the stored energy of the non-recrystallized region is a result of the recovery taking place. The recovery process ultimately influences the evolution of the critical subgrain size with time. The quantified values of stored energy using the DLE method and approximation method have been illustrated for different time periods.

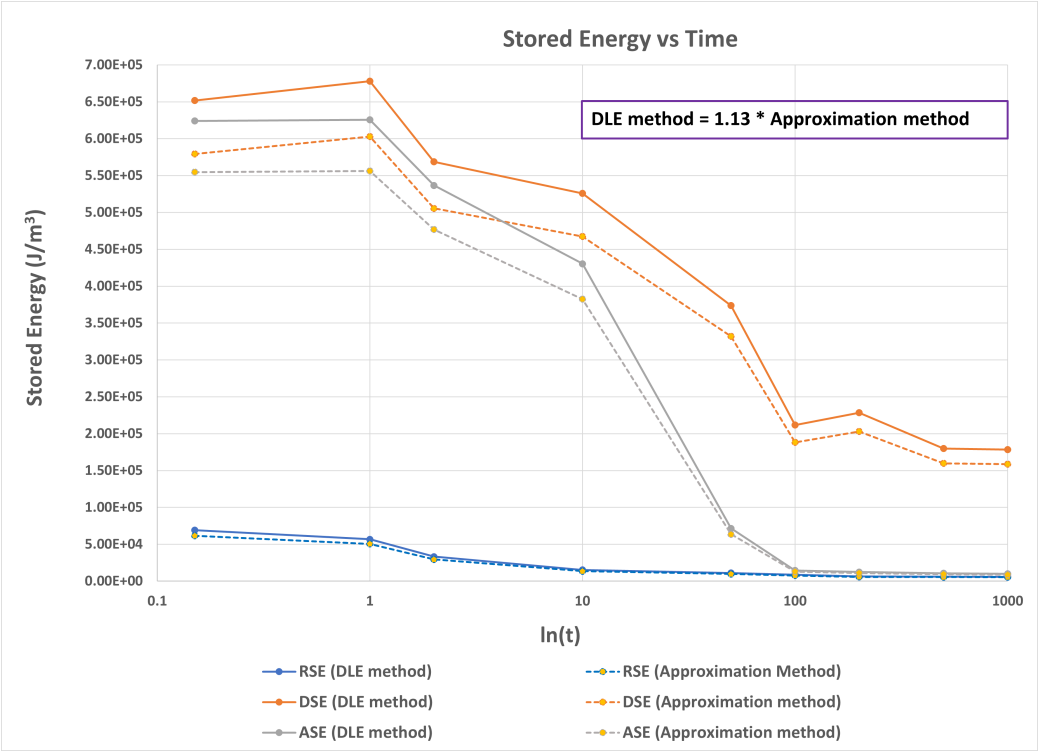

FIGURE A.3: **Quantification of the S_E with time using the DLE method and comparison with the approximation method**

A.5 Incubation Time

The estimation of the incubation time by the mathematical modelled equation in subsection 4.7.1 requires the input of different parameters which have been reported in the table below.

Parameters	**Values**
τ_0	$5x10^{-12}$ s
D_0	$101.5x10^{-6}$ m
m_τ	0.227
n_τ	0.159
l_τ	-2.09
Q_τ	241000
R	8.314 J K^{-1} mol^{-1}

TABLE A.2: Constant Parameters used to mathematically model the incubation time involved during the annealing treatment [14]

Bibliography

[1] K. Lee, J. Han, J. Park, B. Kim, and D. Ko, "Prediction and control of front-end curvature in hot finish rolling process," *Advances in Mechanical Engineering*, vol. 7, no. 11, p. 1687814015615043, 2015.

[2] P. Konijnenberg, S. Zaefferer, D. Raabe, A. Khorashadizadeh, G. Rohrer, A. Rollett, and M. Winning, "Ebsd-electron back-scatter diffraction," *Solar Energy Materials & Solar Cells*, vol. 151, pp. 66–80, 2016.

[3] J. Ryu, "Model for mechanical properties of hot-rolled steels," 2008.

[4] A. Taylor, P. Cizek, and P. Hodgson, "Comparison of 304 stainless steel and ni–30 wt.% fe as potential model alloys to study the behaviour of austenite during thermomechanical processing," *Acta materialia*, vol. 59, no. 14, pp. 5832–5844, 2011.

[5] G. Nolze and R. Hielscher, "Orientations–perfectly colored," *Journal of Applied Crystallography*, vol. 49, no. 5, pp. 1786–1802, 2016.

[6] R. H. Petrov, L. A. Kestens, R. Colás, and G. Totten, "Advanced high-strength steels: Electron backscatter diffraction (ebsd)," *Encyclopedia of Iron, Steel, and Their Alloys; Colás, R., Totten, GE, Eds*, pp. 46–69, 2016.

[7] A. Kundu and D. P. Field, "Influence of microstructural heterogeneity and plastic strain on geometrically necessary dislocation structure evolution in single-phase and two-phase alloys," *Materials Characterization*, vol. 170, p. 110690, 2020.

[8] E. Anselmino, "Microstructural effects on grain boundary motion in al-mn alloys," 2007.

[9] H. Buken, "Modeling static recrystallization in metallic materials," Ph.D. dissertation, Montanuniversität Leoben, 2018.

[10] H. Beladi, P. Cizek, A. S. Taylor, G. S. Rohrer, and P. D. Hodgson, "Static softening in a ni-30fe austenitic model alloy after hot deformation: microstructure and texture evolution," *Metallurgical and Materials Transactions A*, vol. 48, no. 2, pp. 855–867, 2017.

[11] M. K. Rehman and H. S. Zurob, "A novel approach to model static recrystallization of austenite during hot rolling of nb microalloyed steel. part i: Precipitate-free case," *Metallurgical and Materials Transactions A*, vol. 44, no. 4, pp. 1862–1871, 2013.

[12] N. Bozzolo and M. Bernacki, "Viewpoint on the formation and evolution of annealing twins during thermomechanical processing of fcc metals and alloys," *Metallurgical and Materials Transactions A*, vol. 51, no. 6, pp. 2665–2684, 2020.

[13] Y. Jin, M. Bernacki, G. S. Rohrer, A. D. Rollett, B. Lin, and N. Bozzolo, "Formation of annealing twins during recrystallization and grain growth in 304l austenitic stainless steel," in *Materials Science Forum*, vol. 753. Trans Tech Publ, 2013, pp. 113–116.

[14] A. Yoshie, M. Fujioka, Y. Watanabe, K. Nishioka, and H. Morikawa, "Modelling of microstructural evolution and mechanical properties of steel plates produced by thermomechanical control process," *ISIJ international*, vol. 32, no. 3, pp. 395–404, 1992.

[15] F. J. Humphreys and M. Hatherly, *Recrystallization and related annealing phenomena*. Elsevier, 2012.

[16] R. Doherty, D. Hughes, F. Humphreys, J. J. Jonas, D. J. Jensen, M. Kassner, W. King, T. McNelley, H. McQueen, and A. Rollett, "Current issues in recrystallization: a review," *Materials Science and Engineering: A*, vol. 238, no. 2, pp. 219–274, 1997.

[17] G. Higgins, "Grain-boundary migration and grain growth," *Metal Science*, vol. 8, no. 1, pp. 143–150, 1974.

[18] A. Belyakov, T. Sakai, H. Miura, R. Kaibyshev, and K. Tsuzaki, "Continuous recrystallization in austenitic stainless steel after large strain deformation," *Acta materialia*, vol. 50, no. 6, pp. 1547–1557, 2002.

[19] H. Beladi, P. Hodgson, and M. Barnett, "Mapping the hot deformation microstructure of ni-30fe alloy," *ISIJ international*, vol. 45, no. 12, pp. 1893–1896, 2005.

[20] J.-Y. Cho, T. Inoue, F. Yin, and K. Nagai, "Effect of initial grain orientation on evolution of deformed microstructure in hot compressed ni-30fe alloy," *Materials transactions*, vol. 45, no. 10, pp. 2960–2965, 2004.

[21] W. Charnock and J. Nutting, "The effect of carbon and nickel upon the stacking-fault energy of iron," *Metal science journal*, vol. 1, no. 1, pp. 123–127, 1967.

[22] D. Dingley, "Progressive steps in the development of electron backscatter diffraction and orientation imaging microscopy," *Journal of microscopy*, vol. 213, no. 3, pp. 214–224, 2004.

[23] C. Moussa, M. Bernacki, R. Besnard, and N. Bozzolo, "About quantitative ebsd analysis of deformation and recovery substructures in pure tantalum," in *IOP Conference Series: Materials Science and Engineering*, vol. 89, no. 1. IOP Publishing, 2015, p. 012038.

[24] J. F. Nye, "Some geometrical relations in dislocated crystals," *Acta metallurgica*, vol. 1, no. 2, pp. 153–162, 1953.

[25] H. Gao, Y. Huang, W. Nix, and J. Hutchinson, "Mechanism-based strain gradient plasticity—i. theory," *Journal of the Mechanics and Physics of Solids*, vol. 47, no. 6, pp. 1239–1263, 1999.

[26] L. Kubin and A. Mortensen, "Geometrically necessary dislocations and strain-gradient plasticity: a few critical issues," *Scripta materialia*, vol. 48, no. 2, pp. 119–125, 2003.

[27] P. Mannan, A. G. Kostryzhev, H. Zurob, and E. V. Pereloma, "Hot deformation behaviour of ni–30fe–c and ni–30fe–nb–c model alloys," *Materials Science and Engineering: A*, vol. 641, pp. 160–171, 2015.

[28] X. Zhang, "Precipitate evolution in grain oriented electrical steel and high strength low alloy steel," Ph.D. dissertation, University of Groningen, 2020.

[29] L. Kestens and H. Pirgazi, "Texture formation in metal alloys with cubic crystal structures," 2016.

[30] H. Hallberg, "Approaches to modeling of recrystallization," *Metals*, vol. 1, no. 1, pp. 16–48, 2011.

[31] H. F. Poulsen, D. J. Jensen, and G. B. Vaughan, "Three-dimensional x-ray diffraction microscopy using high-energy x-rays," *MRS bulletin*, vol. 29, no. 3, pp. 166–169, 2004.

[32] S. A. Saltikov, "The determination of the size distribution of particles in an opaque material from a measurement of the size distribution of their sections," in *Stereology*. Springer, 1967, pp. 163–173.

[33] D. Raabe, "Recovery and recrystallization: phenomena, physics, models, simulation," *Physical Metallurgy*, pp. 2291–2397, 2014.

[34] S. Hansen, J. Vander Sande, and M. Cohen, "Niobium carbonitride precipitation and austenite recrystallization in hot-rolled microalloyed steels," *Metallurgical Transactions A*, vol. 11, no. 3, pp. 387–402, 1980.

[35] P. R. Rios, F. Siciliano Jr, H. R. Z. Sandim, R. L. Plaut, and A. F. Padilha, "Nucleation and growth during recrystallization," *Materials Research*, vol. 8, pp. 225–238, 2005.

[36] F. Lin, Y. Zhang, W. Pantleon, and D. J. Jensen, "Importance of non-uniform boundary migration for recrystallization kinetics," *Metallurgical and Materials Transactions A*, vol. 49, no. 11, pp. 5246–5258, 2018.

[37] M. Sabatini, "Corrosion of electrodeposited nanocrystalline nickel-iron (ni-fe) alloys in neutral and alkaline sulphate environments," Ph.D. dissertation, University of Toronto (Canada), 2018.

[38] J. Cahoon, Q. Li, and N. Richards, "Microstructural and processing factors influencing the formation of annealing twins," *Materials science and engineering: a*, vol. 526, no. 1-2, pp. 56–61, 2009.

[39] Q. Li, J. Cahoon, and N. Richards, "On the calculation of annealing twin density," *Scripta materialia*, vol. 55, no. 12, pp. 1155–1158, 2006.

[40] K.-H. Song, Y. B. Chun, and S.-K. Hwang, "Direct observation of annealing twin formation in a pb-base alloy," *Materials Science and Engineering: A*, vol. 454, pp. 629–636, 2007.

[41] H. Gleiter, "The formation of annealing twins," *Acta metallurgica*, vol. 17, no. 12, pp. 1421–1428, 1969.

[42] C. Pande, M. Imam, and B. Rath, "Study of annealing twins in fcc metals and alloys," *Metallurgical transactions A*, vol. 21, no. 11, pp. 2891–2896, 1990.

[43] D. Brandon, "The structure of high-angle grain boundaries," *Acta metallurgica*, vol. 14, no. 11, pp. 1479–1484, 1966.

[44] D. L. Olmsted, S. M. Foiles, and E. A. Holm, "Survey of computed grain boundary properties in face-centered cubic metals: I. grain boundary energy," *Acta Materialia*, vol. 57, no. 13, pp. 3694–3703, 2009.

[45] C. Haase, M. Kühbach, L. A. Barrales-Mora, S. L. Wong, F. Roters, D. A. Molodov, and G. Gottstein, "Recrystallization behavior of a high-manganese steel: Experiments and simulations," *Acta Materialia*, vol. 100, pp. 155–168, 2015.

[46] V. I. Kalikmanov, "Classical nucleation theory," in *Nucleation theory*. Springer, 2013, pp. 17–41.

[47] W. A. Johnson, "Reaction kinetics in processes of nucleation and growth," *Am. Inst. Min. Metal. Petro. Eng.*, vol. 135, pp. 416–458, 1939.

[48] M. Avrami, "Granulation, phase change, and microstructure kinetics of phase change. iii," *The Journal of chemical physics*, vol. 9, no. 2, pp. 177–184, 1941.

[49] A. Kolmogorov, "Sobre a teoria estatística da cristalização de metais," *Izv. Akademii Nauk SSSR–Ser. Matemat*, vol. 1, pp. 355–359, 1937.

[50] P. Rios and E. Villa, "Transformation kinetics for inhomogeneous nucleation," *Acta Materialia*, vol. 57, no. 4, pp. 1199–1208, 2009.

[51] P. Rios, L. Pereira, F. Oliveira, W. Assis, and J. Castro, "Impingement function for nucleation on non-random sites," *Acta Materialia*, vol. 55, no. 13, pp. 4339–4348, 2007.

[52] C. Sellars, "Modelling microstructural development during hot rolling," *Materials Science and technology*, vol. 6, no. 11, pp. 1072–1081, 1990.

[53] G. Jauncey, "The scattering of x-rays and bragg's law," *Proceedings of the National Academy of Sciences of the United States of America*, vol. 10, no. 2, p. 57, 1924.

[54] K. Mingard, B. Roebuck, E. Bennett, M. Gee, H. Nordenstrom, G. Sweetman, and P. Chan, "Comparison of ebsd and conventional methods of grain size measurement of hardmetals," *International Journal of Refractory Metals and Hard Materials*, vol. 27, no. 2, pp. 213–223, 2009.

[55] W. T. Read and W. Shockley, "Dislocation models of crystal grain boundaries," *Physical review*, vol. 78, no. 3, p. 275, 1950.

[56] K. Kurzydłowski, "On the formation of twin grains as a result of grain encounters during the process of recrystallization and grain growth," *Scripta metallurgica et materialia*, vol. 25, no. 5, pp. 1099–1102, 1991.

[57] T. Sakai, A. Belyakov, R. Kaibyshev, H. Miura, and J. J. Jonas, "Dynamic and post-dynamic recrystallization under hot, cold and severe plastic deformation conditions," *Progress in materials science*, vol. 60, pp. 130–207, 2014.

[58] J. Friedel, *Dislocations: international series of monographs on solid state physics*. Elsevier, 2013, vol. 3.

[59] J. Bailey and P. B. Hirsch, "The recrystallization process in some polycrystalline metals," *Proceedings of the Royal Society of London. Series A. Mathematical and Physical Sciences*, vol. 267, no. 1328, pp. 11–30, 1962.

[60] M. Oyarzábal, A. Martínez-de Guerenu, and I. Gutiérrez, "Effect of stored energy and recovery on the overall recrystallization kinetics of a cold rolled low carbon steel," *Materials Science and Engineering: A*, vol. 485, no. 1-2, pp. 200–209, 2008.

[61] M. Suehiro, Z.-K. Liu, and J. Ågren, "A mathematical model for the solute drag effect on recrystallization," *Metallurgical and Materials Transactions A*, vol. 29, no. 13, pp. 1029–1034, 1998.